

Structural Composite Lithium-ion Battery

*Effect of intercalation induced volumetric
changes on micro-damage*

Johanna Xu

Polymeric Composite Materials



Structural Composite Lithium-ion Battery

*Effect of intercalation induced volumetric
changes on micro-damage*

Johanna Xu

Luleå University of Technology
Department of Engineering Sciences and Mathematics
Division of Materials Science

Printed by Luleå University of Technology, Graphic Production 2019

ISSN 1402-1544

ISBN 978-91-7790-312-3 (print)

ISBN 978-91-7790-313-0 (pdf)

Luleå 2019

www.ltu.se

Preface

The work presented in this thesis has been carried out at Luleå University of Technology between November 2014 and January 2019. The financial support provided by the Swedish Energy agency grant project 37712-1, KOMBATT II, is gratefully acknowledged.

First and foremost, I would like to express my gratitude to my supervisor Professor Janis Varna, for all the support and guidance he has provided me. I would also like to thank my co-supervisor Professor Göran Lindbergh for welcoming me to the Applied Electrochemistry group at KTH during the very beginning of my Ph.D. studies and for all help since then. Associate Professor Andrejs Pupurs is acknowledged for generously sharing his knowledge and experience whenever needed.

The entire KOMBATT-II team is acknowledged for valuable discussions. With a special mention to Wilhelm Johannisson, Johan Hagberg and Ross Harnden at KTH for nice collaborations in the experimental work.

I want to express my appreciation to my colleagues and friends at the division of Materials Science, and in particular the Polymeric Composite Materials group, for the nice working environment.

Last but by no means least, to my friends and family, your loving support will never be forgotten.

To all of you, thank you very much.

Johanna Xu

Luleå, January 2019

Abstract

The quest for lighter materials and structures to reduce climate impacts in the automotive industry has paved the way for multifunctional solutions. Mass saving on a system level can be achieved by materials or structures having more than one primary function, thus reducing the number of components used. Structural batteries are composite materials that simultaneously carry mechanical loads while delivering electrical energy. While carbon fiber is a commonly used reinforcing material in high-performance composite materials, it also possesses excellent lithium intercalation properties. Therefore, it is possible to use carbon fiber to develop structural batteries based on lithium-ion battery technology.

Among several proposed solutions, the micro-battery employs the carbon fiber as a negative electrode of the battery and also as a composite reinforcement material. The fiber is coated with a solid polymer electrolyte which works as an ion conductor and separator whilst transferring mechanical loads. The coated fiber is surrounded by additional matrix material acting as a positive electrode, composed of conductive additives, active electrode material and electrolyte. This assembly of materials allows the necessary electrochemical processes to occur simultaneously, including electrochemical reactions at the surface of the active electrode material, mass transport within active electrode material by diffusion, mass transport in electrolyte by diffusion and migration, and electronic conduction.

During electrochemical cycling the electrodes undergo volume changes as a result of lithium transport. The work in this thesis addresses the effects of volume changes on internal mechanical stress state in the structural battery. A physics-based mathematical model employing a number of coupled nonlinear differential equations has been set-up and solved numerically to investigate performance in the structural battery material. The resulting transient lithium ion concentration distributions were used in combination with linear elastic analysis in order to assess the

mechanical stresses in the fiber, coating and matrix caused by non-uniform swelling and shrinking of the micro-battery. Stress analysis shows that high hoop stress in the matrix during charging may initiate radial matrix cracks at the coating/matrix interface. Linear elastic fracture mechanics has been used to analyze radial matrix crack propagation and debonding at coating/matrix interface in both unidirectional (UD) and cross-ply laminate, under electrochemical load only and combined electrochemical and thermomechanical load. Results show that for cross-ply structural battery composite the sequence of macro-scale crack forming events differs from a conventional cross-ply composite, as well as from a UD composite battery laminate. The most likely course of failure events in a cross-ply laminate were found to be: 1) radial matrix crack initiation and unstable growth; 2) matrix/coating debond when the matrix crack has a certain length.

List of appended papers

This thesis consists on an extended summary and the following appended papers:

Paper I

Xu J, Lindbergh G, Varna J. Multiphysics modeling of mechanical and electrochemical phenomena in structural composites for energy storage: Single carbon fiber micro-battery. *J Reinf Plast Compos* 2018;37(10):701-715.

Paper II

Xu, J., Lindbergh, G. & Varna, J. Carbon fiber composites with battery function: Stresses and dimensional changes due to Li-ion diffusion. *J. Compos. Mater.* (2018). doi:10.1177/0021998317752825

Paper III

Xu J, Varna J. Matrix and interface microcracking in carbon fiber/polymer structural micro-battery. *Submitted to J. Compos. Mater.* (2018).

Paper IV

Xu J, Varna J. Matrix and interface cracking in cross-ply composite structural battery under combined electrochemical and mechanical loading. *Submitted to Composites Science & Technology* (2019)

Paper V

Xu J, Varna J. Methodology for mechanical quality evaluation of carbon fiber coating with energy storage function. *Submitted to Experimental Techniques* (2017)

Paper not included in thesis

Hagberg, J., Maples, H. A., Alvim, K. S. ..., Xu, J., Johannisson, W., Bismarck, A., . . .
Lindbergh, G. (2018). Lithium iron phosphate coated carbon fiber electrodes for structural lithium ion batteries. *Composites Science & Technology*, 162, 235-243

Oral presentation at conferences

J. Xu, A. Pupurs, J. Varna, Mathematical model for intercalation induced stresses in multifunctional material constituents, Oral presentation at 8th EEIGM Conference. Valencia, Spain, June 2015

J.Xu Strukturella kompositbatterier för energieffektiva fordon, Oral presentation at Energirelaterad fordonsforskning 2016, Gothenburg Sweden, April 2016

Xu, J., Pupurs, A., Lindbergh, G. & Varna, J. . Multifunctional composites: Modeling intercalation induced stresses in constituents of micro-battery. In: *ECCM 2016: Proceeding of the 17th European Conference on Composite Materials*. Paper presented at 17th European Conference on Composite Materials, Munich, Germany, 26-30th June 2016.

Contents

1.	Introduction	1
	Fiber Composites.....	1
	The Lithium- ion battery	4
	Multifunctionality and structural composite battery	5
	Design of 3D structural composite micro-battery	7
2.	Modeling	10
	Mathematical models of processes in the lithium ion battery	10
	Mechanical modeling	13
	Material models for constituents	13
	Homogenization	14
	Fracture mechanics.....	19
3.	Experimental characterization of interfaces	22
	Macro-scale test.....	22
	Micro-scale test	24
4.	Scope of the thesis.....	29
5.	Summary of papers.....	30
6.	Future work	45
	Bibliography.....	52

1. Introduction

Fiber Composites

Over the past 50 years, man-made synthetic composite materials have become one of the most important engineering materials, in particular carbon fiber reinforced polymer (CFRP) composites. Today, CFRP are found in virtually all high-performance applications where weight saving in combination with high strength and stiffness is important.

In laminated CFRP, each lamina consists of parallel (and continuous) carbon fibers oriented in the same direction, surrounded by polymer matrix material. The carbon fibers carry structural load and provide high stiffness and strength of the composite material. The primary task of the matrix material, typically a thermoset polymer, is to bind the materials together, and to transfer and distribute loads between the reinforcing fibers.

The freedom of design is one of the most attractive features of the composite material. Depending on the application, the material can be designed to achieve desirable properties while suppressing unwanted ones, by selecting different material systems and varying the lay-up. Most composite structures are built from multidirectional laminates, which are made of unidirectional (UD) plies with different fiber orientations with respect to the specimen axis, Figure 1.

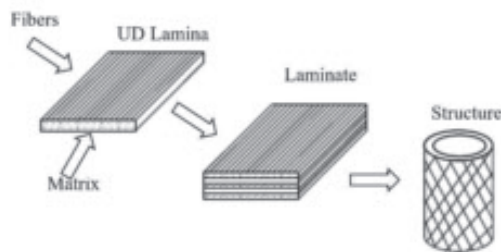


Figure 1. Composite structure built from multidirectional laminate.

Damage modes in composites

The definition of failure in composites varies depending on the application. In some applications a very small damage may be qualified as failure, for example in pressure vessels where a very small crack leads to leakage. Whereas in other applications only total fracture is considered as failure. Generally, internal material failure initiates long before any changes in the macroscopic behavior are observed. Internal material failure can occur in many forms, including fiber breaks, separation of fibers from the matrix (debonding), microcracking of the matrix and separation between layers (delamination), Figure 2 . The influence of internal damage on material's macroscopic behavior is observed when the frequency of internal damage is sufficiently high.

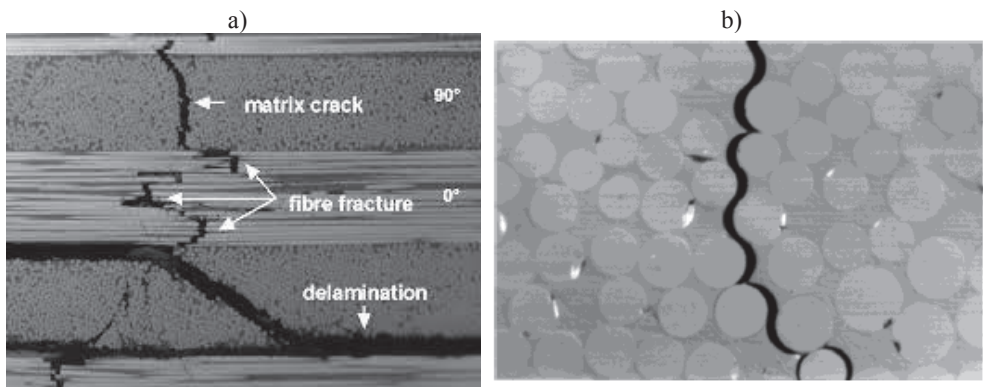


Figure 2. Cross-section micrographs of failures in composite materials. a) Carbon fiber composite laminate with matrix crack, delamination and fiber fracture [1]. b) Multiple debonds at fiber/matrix interface forming a transverse crack in glass fiber composite [2].

Introduction to microcracking

The damage mode considered in this thesis is transverse cracking (also known as intralaminar cracking) focusing on 1) microcracks in the matrix; 2) debonding at fiber/matrix interface.

For composites containing off-axial plies, especially 90°-plies in a cross-ply laminate, when subjected to longitudinal tensile loading, the transverse crack propagating through the thickness

in 90° plies is usually found as the first failure event. These meso-scale cracks are a result from individual fiber/matrix debonds coalescing on micro-scale. Once the first transverse crack is formed, the number of similar cracks increases with increasing load [3].

Single fiber composite models were used at an early stage to understand the crack forming mechanisms. In one of the few experimental studies of its kind Zhang et al [4] studied the debond crack growth in an experimental setup of a single fiber embedded in matrix materials, subjected to transverse loading, Figure 3a. During the test debonds at fiber/matrix interface resulted from existing flaws, upon additional load the debond growth varies depending on the interface quality, Figure 3b. It was found that for composites with strong interface bonding the debond growth in the circumferential direction and propagation along fiber direction happen simultaneously.

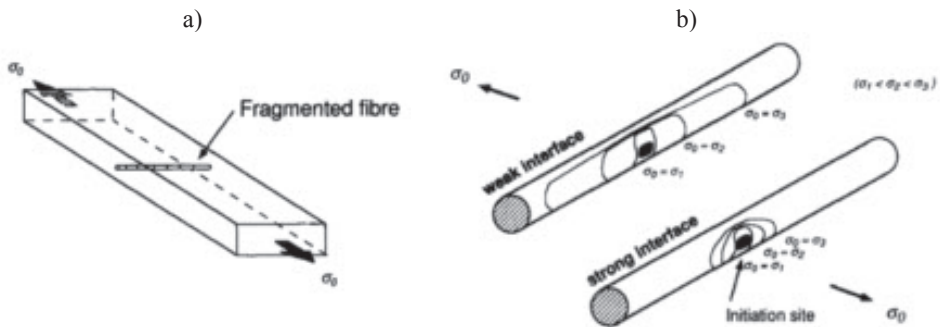
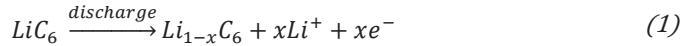


Figure 3.a) Fragmented single fiber specimen, subjected to transverse tensile loading.
 b) Interfacial debonding processes. Figures reprinted from [4]

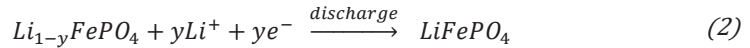
The Lithium- ion battery

Lithium-ion battery (LIB) is one type of secondary batteries (i.e. rechargeable batteries) which uses oxidation-reduction reactions to convert chemical energy into electrical energy and vice versa. A conventional LIB consists of two electrodes, negative and positive, with a separator in between soaked with liquid electrolyte. The electrodes are of porous character consisting of nano-to-micrometer sized active electrode material particles, mixed with conductive additives and binder material. The active materials of LIB electrodes are intercalating materials. Intercalation is the reversible mechanisms allowing insertion of guest ions into a host material with layered structures. Graphite and lithium iron phosphate (LiFePO₄) are active materials commonly used as active materials in the negative and positive electrode, respectively. The pores of the electrodes are filled with an electrolyte. During discharging in a LiFePO₄/graphite cell the following reactions take place at the electrode/electrolyte interfaces.

At the negative electrode; oxidation



and at the positive electrode; reduction



where x and y varies between 0 and 1.

During charging the reactions are reversed. The electrons in the redox reactions are transferred between the electrodes via an external circuit, and the ions are transported in the electrolyte,

Figure 4. The cell voltage is dependent on the difference in electrochemical potential between the reactions, and can be calculated theoretically from thermodynamics and the change in Gibbs free energy [5].

The electrolyte plays a key role in the battery, since it is the medium for ion transportation between the electrodes. There are four different types of electrolytes, organic liquids, ionic liquids, solid polymer electrolytes and gel electrolytes [6]. Most electrolytes used in commercial lithium-ion batteries are liquids, consisting of a lithium salt; such as lithium hexafluorophosphate (LiPF_6), dissolved in solvent mixture; typically ethylene carbonate (EC), diethyl carbonate (DEC), dimethyl carbonate (DMC) [7].

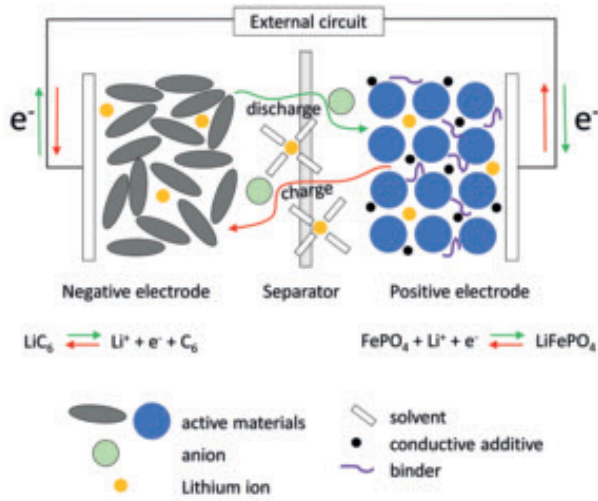


Figure 4. Schematic of a battery cell, working principle and constituents

Multifunctionality and structural composite battery

Lately, there has been a paradigm shift in the approach to achieve weight and volume saving of system as a whole –an introduction of multifunctionality in composites, which simultaneously perform at least two functions. Research in the area of multifunctional composite materials is increasing [8]. Multifunctionality can be achieved through structural composite batteries [9-12], a composite material which simultaneously and intrinsically carries mechanical load while delivering electrical energy through LIB technology. Benefits from this type of energy delivering

and/or storage materials are extensive. Essentially, any system that requires electrical energy with load bearing components can benefit from structural batteries in order to decrease the total weight.

To design structural composite material battery, commercial carbon fiber can be used for its load carrying properties and for its electrical conduction and intercalation ability. Commercially available intermediate modulus (IM) carbon fiber has shown ability to intercalate lithium comparable to that of theoretical maximum for pure graphite [13-15]. Repeated electrochemical cycling (intercalation/deintercalation) of the carbon fiber causes degradation in ultimate tensile strength, while the tensile stiffness remains unchanged [16,17].

For mechanical performance in structural composite the liquid electrolyte commonly used in conventional batteries must be replaced with a solid electrolyte, acting as an ion conductive medium as well as transferring load in the composite material. A major drawback for using solid electrolytes is the decreased ion conductivity with increased stiffness [18-21].

In the 3D micro-battery cell concept, the negative electrode consists of one single carbon fiber, coated with a thin layer of structural battery electrolyte (SBE) and an additional layer with the positive electrode [9,22,23]. With this battery design the single fiber battery cells work in parallel, as shown in Figure 5, and the low ion conductivity is overcome by reducing the thickness of the electrolyte to a less than 500 *nm* by electropolymerization [24].

The matrix material needs to act as load transfer medium as well as to function as an electrode. This is achieved by adding electrochemically active material (lithium iron phosphate, LiFePO_4) and conductive additives to the mixture of electrolyte and polymer binder.

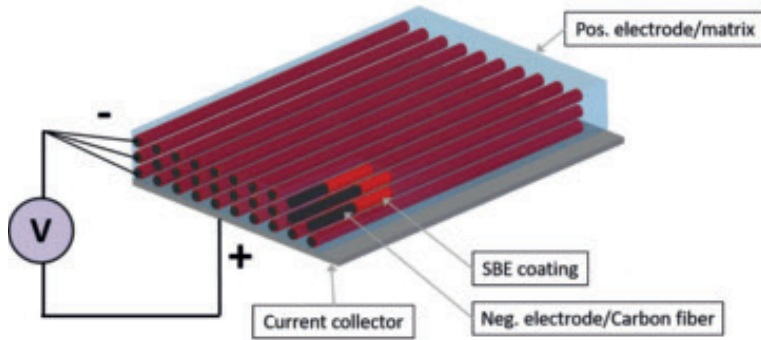


Figure 5. Schematic illustration of the battery structural composite material. Each carbon fiber is coated with a ion-conductive but electrically insulating SBE and surrounded by the cathode matrix material.

Design of 3D structural composite micro-battery

Conventional LIB are manufactured with the negative electrode (anode) capable of accommodating more charge than that can be stored in the positive electrode (cathode) [25]. For a structural micro-battery this means that the capacity for Li intercalation in the matrix has to be matched with Li intercalation capacity in the fiber. There is no advantage of storing more ions in the matrix than can be inserted in the fiber, since it is associated with safety issues which ultimately lead to battery failure [26]. On the other hand, if the storage capacity in the matrix is too small, the fiber's ability to intercalate is not fully utilized.

In Table 1 some physical properties of the electrodes are shown, it can be seen that the specific capacity of the active material in the positive electrode, Q_{spec}^+ , is half that of the negative electrode, Q_{spec}^- . The composite fiber volume fraction, V_f , determines the capacity ratio between the electrodes.

Table 1. Properties of the electrode active material.

Parameter	Description	Unit	Value
Q_{spec}^+	Specific capacity, positive electrode	[mAh/g]	169
Q_{spec}^-	Specific capacity, negative electrode	[mAh/g]	372
ρ^+	Density, positive electrode	[kg/m ³]	3600
ρ^-	Density, negative electrode	[kg/m ³]	1780

The electrodes in the 3D battery considered in this work, denoted as “reference case” are designed to hold a ratio between the capacity of the positive and negative electrode, $R_{P/N} = 0.92$, close to but less than 1. $R_{P/N}$ is defined as

$$R_{P/N} = \frac{j_{1C}^+}{j_{1C}^-} \quad (3)$$

where j_{1C} is the current density [A/m^2] for 1C discharging, superscripts + and – represent the positive (matrix) and negative (fiber) electrode respectively, j_{1C} is given by

$$j_{1C}^+ = \frac{c_{s,max}^+ \cdot \varepsilon_s^+ \cdot F \cdot V^+}{1[h]} \quad j_{1C}^- = \frac{c_{s,max}^- \cdot F \cdot V^-}{1[h]} \quad (4)$$

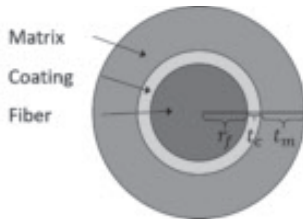
where ε_s^+ is the porosity of the positive electrode (volume fraction active material particles), F is the Faraday constant ($F = 96487 \text{ A s} \cdot \text{mol}^{-1}$), V^+ and V^- is the volume of the positive and negative electrodes, respectively, $c_{s,max}^+$ and $c_{s,max}^-$ is the maximum Li concentration in the active material (LiFePO₄) and fiber electrode, respectively, defined as

$$c_{s,max}^+ = \frac{Q_{spec}^+ \cdot \rho^+}{F} \quad c_{s,max}^- = \frac{Q_{spec}^- \cdot \rho^-}{F} \quad (5)$$

where Q_{spec}^+ and Q_{spec}^- are specific capacities, defined as the amount of charge per weight that a battery electrode material contains.

In Table 2 the dimensions of the 3D structural composite battery for the reference case are listed, which yield $V_f = 0.338$.

Table 2. Geometrical parameters of the cylinder unit for the reference case, $V_f = 0.338$.



Parameter	Value [μm]
Fiber radius, r_f	2.5
Coating thickness, t_c	0.1
Matrix thickness, t_m	1.7

2. Modeling

Mathematical models of processes in the lithium ion battery

The behavior of a lithium ion battery is modeled by describing the mass and charge balances within the battery cell, using a set of coupled partial differential equations. The time and coordinate dependent variables in these equations are potentials and concentrations in solid and electrolyte phase, respectively [27-29]. This subchapter outlines the physics-based equations used in the models in the included papers. The models were solved with COMSOL Multiphysics [30]. The many processes occurring within a lithium-ion battery under operation include mass transport in the electrolyte and in the active material particles (host material for lithium intercalation), electrochemical reaction and electron conduction.

Mass transport in gel electrolyte

Ions in an electrolyte are transported both by migration and diffusion. In the beginning of the cell discharge an electric potential difference over the electrolyte is created, causing lithium ions to be transported through migration from the negative to the positive electrode. Also, anions (PF_6^-) are migrating due to the electric potential difference, but in the opposite direction to the lithium ions. Because of the migration of anions, a concentration difference in the electrolyte is created, causing a diffusion flux of lithium ions and the anions in the opposite direction to the anion flux. For a gel electrolyte that contains lithium hexafluorophosphate (LiPF_6 , salt) dissolved in a mixture of ethylene carbonate and propylene carbonate (EC and PC, solvent mixture, treated as one species [31]) and polymer binder material poly(vinylidene fluoride-co-hexafluoropropylene) P(VdF-HFP), the material balance for the salt and solvent is expressed as

$$\frac{\partial c_{salt}}{\partial t} = \nabla \cdot \left(D_{SS} \nabla c_{salt} + D_{SL} \nabla c_{solv} + (1 - t_+) \frac{i_e}{F} \right) \quad (6)$$

and

$$\frac{\partial c_{solv}}{\partial t} = \nabla \cdot \left(D_{LS} \nabla c_{salt} + D_{LL} \nabla c_{solv} - (t_{solv}) \frac{i_e}{F} \right) \quad (7)$$

In Eq. (6)-(7) ∇ is the Nabla operator. The solvent concentration dependent diffusivities D with subscript SS, SL, LS or LL are apparent diffusivities based on Maxwell-Stefan diffusivities. The apparent transport numbers. t_+ and t_{solv} describes the fraction of the total current carried in an electrolyte by a given ionic species and F is the Faraday constant. The electrolyte phase current density, i_e , is a function of variation of the potential across the electrolyte, φ_e , conductivity κ , and the salt and solvent concentration gradients.

$$i_e = \kappa (-\nabla \varphi_e + \eta_{salt} \nabla c_{salt} + \eta_{solv} \nabla c_{solv}) \quad (8)$$

Electrolyte mass transport in porous electrode

The mass transport in a porous electrode is affected by the pore structure, hence the porosity, ε , and the tortuosity, τ , must be taken into account. Therefore, the effective parameters for the electrode are calculated by an averaging process which includes parameters of the electrolyte phase and parameters of the porosity ε_e and tortuosity, τ_e

$$P_{eff} = P \cdot \varepsilon_e^{\beta_e} \quad P = D_{SS}, D_{SL}, D_{LS}, D_{LL}, \kappa \quad (9)$$

where ε_e is the porosity (volume fraction) of electrolyte in the porous positive electrode, and β_e is the electrolyte phase Bruggeman coefficient, constant for all properties P , and takes the tortuosity into account. The power function describes the accessibility for the species transport in the electrode.

Mass transport in active material particle

In electrochemically active materials, diffusion is assumed to govern the transport. The diffusion is modeled with Fick's 2nd law, Eq. (10), used to calculate the spatial variations in lithium concentration between the surface and center of the active material particle. With a carbon fiber as the active material in the anode Eq. (10) is solved using cylindrical coordinates. In the cathode where the particles are described as uniform spheres Eq. (10) is solved using spherical coordinates.

$$\frac{\partial c_s}{\partial t} = \nabla \cdot (-D_s \nabla c_s) \quad (10)$$

where c_s is the lithium concentration in the active electrode particles, ∇ is the nabla operator and D_s is the solid phase diffusion coefficient which depends on c_s .

Electrochemical reaction

The intercalation reaction which allows for lithium access into and out of the active material through oxidation or reduction, is assumed to take place at the surface of the active material particles. The Butler-Volmer equation is often used to describe the process kinetics which calculates the Faradic current locally, i_{loc} , as a function of the local overpotential [32].

$$i_{loc} = i_0 \left(\exp\left(\frac{\alpha_a i F \eta}{RT}\right) - \exp\left(-\frac{\alpha_c i F \eta}{RT}\right) \right) \quad (11)$$

where F is Faraday's constant, R is the universal gas constant, and T is temperature, i_0 is the exchange current density, α_a and α_c are the electrochemical reaction symmetry factors and η is the overpotential defined as:

$$\eta = \varphi_s - \varphi_e - E_{eq} \quad (12)$$

In Eq. (12) φ with subscript s and e is the potential for the solid and electrolyte phase, respectively. E_{eq} is the electrode equilibrium potential. The equilibrium potential is determined by the intercalation degree, i.e. the electrode phase Li concentration and the electrolyte phase lithium ion concentration.

Electronic conduction

Electrons are transported in the electronically conductive materials in the electrode. Ohm's law is used to calculate the solid phase potential distribution in the electrode.

$$i_s = -\sigma_s \nabla \varphi_s \quad (13)$$

where i_s is the current density of the electrode phase, and σ_s the electrode potential.

Mechanical modeling

The dimensional changes and internal stresses in the constituents of the composite are due to mismatch and anisotropy of expansion coefficients, and local concentration changes of Li in the active material in the composite. The dimensional changes are not free expansion of constituents but rather a result of interaction with mechanical constrains from other parts of the structural composite battery.

Material models for constituents

The stress-strain relationship for a transversely isotropic material with intercalation induced volumetric changes can be introduced using the thermo-mechanical analogy [33], assuming that the dimensional changes are proportional to the Li concentration, c .

$$\sigma_i^k = C_{ij}^k (\varepsilon_j^k - \varepsilon_j^{k,free\ swelling}) \quad (14)$$

For the cylindrical unit cell index $k = m$ is for the matrix, $k = c$ for the coating, and $k = f$ for the fiber, and indices $i, j = r, \theta, 1$ are cylindrical coordinates. For the spherical unit cell representing the matrix, the upper index is for the particle and the surrounding slurry and the lower index for spherical coordinates. Repeating indexes in Eq (14) denote summation. C_{ij}^k is the stiffness matrix using Voigt notation, $\varepsilon_j^{k,free\ swelling}$ is the free swelling strain in j -direction due to Li-ion intercalation; swelling does not have shear components. For fiber

$$\varepsilon_j^{f,free\ swelling} = \beta_j^f \frac{c_f}{c_{s,max}^-}, \text{ where } \beta_j^f \text{ are constant coefficients of proportionality called}$$

intercalation-expansion coefficients to characterize the dimensional changes in the three

directions. $\frac{c_f}{c_{s,max}^-}$ is the normalized Li concentration in the fiber, where c_f is the time dependent Li

concentration in the electrode material, $c_{s,max}^-$ is the maximum concentration reached when Li

has intercalated into all available sites. The free swelling strain $\varepsilon^{m,free\ swelling}$ of the matrix is analyzed in the next section

Homogenization

The micro-battery is a multiscale composite material: it is a UD coated fiber composite with the matrix by itself being a spherical particle reinforced composite. Homogenization is used to

compute the homogenized properties of the matrix and effective macroscopic composite

properties, Figure 6. These properties are necessary in developing multi-fiber models for

microcracking analysis to reduce the number of explicitly considered fibers and to account for the constraint applied by surrounding layers in a multidirectional laminate.

The matrix material is a particle composite with effective isotropic properties. The micromechanical modeling to obtain effective properties of the matrix uses the Composite Spheres Assemblage (CSA) introduced by Hashin [34], assuming two phases present. The spherical LiFePO_4 active material represents the particle phase, and the remaining constituents (SBE, carbon black and additional binder material) together comprise the so called slurry phase, shown schematically in Figure 6.

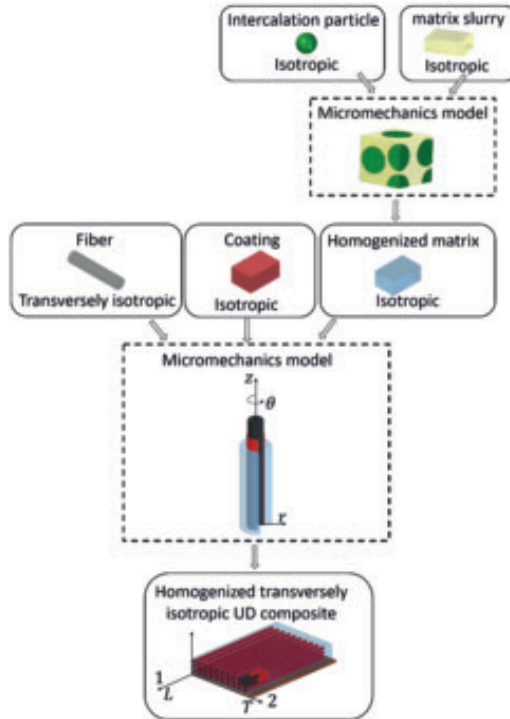


Figure 6. Modeling scheme for effective properties of UD composite material.

In the CSA the bulk modulus K is given by

$$K^* = K_s + (K_p - K_s) \frac{(3K_s + 4G_s)V_p}{3K_p + 4G_s - 3(K_p - K_s)V_p} \quad (15)$$

with superscript * denoting the effective property of the particle composite and subscript s and p denotes slurry and particle phases, respectively. V is the volume fraction, and G is the shear modulus for each phase calculated by Eq. (16), where E is the Young's modulus and ν is the Poisson's ratio

$$G = \frac{E}{2(1 + \nu)} \quad (16)$$

The shear modulus for the particle composite is then given by

$$G^* = G_s + \frac{V_p}{1/(G_p - G_s) + 6V_p(K_p + 2G_s)/5G_s(3K_s + 4G_s)} \quad (17)$$

Since the matrix material is regarded macroscopically isotropic, Young's modulus, E^* , may be calculated from the bulk and shear modulus

$$E^* = \frac{9K^*G^*}{3K^* + G^*} \quad (18)$$

The free swelling strain of the homogenized matrix, assuming $\beta_s = 0$, is given by

$$\varepsilon^{m,f \text{ ree swelling}} = \beta_p V_p \left(1 + \frac{4(K_p - K_s)G_s V_s}{3K_s K_p + 4G_1(K_s V_s + K_p V_p)} \right) \frac{c_p}{c_{p,max}} \quad (19)$$

where $\frac{c_p}{c_{p,max}}$ is the normalized Li concentration in the LiFePO₄ particle, calculated from the electrochemical model, Eq.(6)- (13), with boundary conditions given in the appended **Paper I**.

The elastic properties of the UD composite are calculated using the Concentric Cylinder Assembly (CCA) model introduced by Hashin [34,35]. Explicit expressions are obtained for the effective plane-strain bulk modulus K_{23} , the shear modulus G_{12} , longitudinal modulus E_1 and

Poisson's ratio ν_{12} . The transverse shear modulus G_{23} is obtained by using a self-consistent scheme, first introduced by Christensen and Lo [36]. The cylinder representation of the three-phase system (fiber, coating and particle reinforced matrix) is shown in Figure 6. The stress-strain state is independent on the axial coordinate z .

The elastic problems to solve, include i) radial loading to find bulk modulus K_{23} , ii) axial loading in fiber direction to find E_1 and ν_{12} , iii) in-plane shear loading to find G_{12} , and iv) shear loading in the plane transverse to the fiber to find G_{23} , Figure 7. E_2 can then be calculated from K_{23} and G_{12} . The entire set of equations can be found in [37].

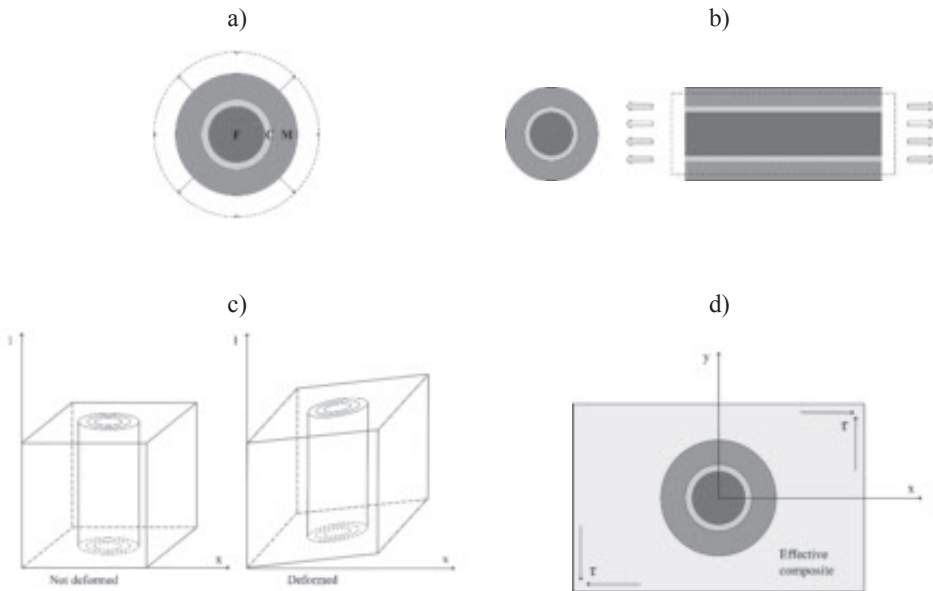


Figure 7. Deformation of the composite from a) radial loading, b) axial loading, c) pure in-plane shear loading, and d) shear loading in the plane transverse to the fiber.

In Table 3 the properties of the fiber, coating and the homogenized matrix (with a particle volume fraction $V_p = 0.553$) are presented along with the calculated UD composite properties.

Table 3. Assumed and calculated elastic constants and intercalation swelling parameters.

Constituent	E_z (GPa)	E_r (GPa)	ν_{zr} (-)	$\nu_{r\theta}$ (-)	Expansion	
					$\beta_z(-)$	$\beta_r(-)$
Fiber	300	30	0.2	0.45	0.009	0.05
SPE coating	1	1	0.3	0.3	0	0
Matrix, $V_p = 0.553$	2.5	2.5	0.3	0.3	0.04	0.04
	E_L (GPa)	E_T (GPa)	ν_{LT} (-)	ν_T (-)	$\beta_L(-)$	$\beta_T(-)$
UD composite, ($V_f=0.338$)	103.0	4.0	0.27	0.47	0.0089	-0.017

The expansion coefficients for the UD composite β_L and β_T require special discussion presented below. Free expansion of electrode host materials due to intercalation is a well-known phenomenon [38-40]. Initially, it may seem tempting to model this mechanism by following the approach of well-studied models of other volume changing phenomena in fiber reinforced composites, such as moisture absorption. However, the moisture weight in the composite increases during absorption, which makes the moisture weight fraction a suitable variable to use in modeling. In contrast, the amount of Li in the composite material is constant, but the content in the constituents changes (redistributes) during charging/discharging causing dimensional changes of the constituents and the whole composite. Therefore, the effective composite intercalation expansion cannot be related to the amount of available lithium (which is not changing). A different variable has to be introduced to correlate with the macroscopic dimensional changes, here the normalized average Li content in the fiber, $c_{f,avg}/c_{f,max}$ was used. $c_{f,avg}$ is the average Li concentration in the fiber, and $c_{f,max}$ is the carbon fiber maximum Li storing capacity. According to linear theory, the intercalation is inducing dimensional changes (strains) to the composite, ε^I , which are proportional to $c_{f,avg}/c_{f,max}$, and different in different directions, Eq. (20) in matrix form

$$\begin{pmatrix} \varepsilon_L^I \\ \varepsilon_T^I \\ \gamma_{LT}^I \end{pmatrix} = \begin{pmatrix} \beta_L \\ \beta_T \\ 0 \end{pmatrix} \frac{c_{f,avg}}{c_{f,max}}. \quad (20)$$

For the UD composite the reference state with assumed zero macroscopic expansion and zero micro-stresses is when the Li content in the fiber is zero (discharged) and the matrix is fully charged. The expansion coefficient in the fiber direction, β_L , can then be described by a simple rule-of-mixture expression

$$\beta_L = \frac{E_z^f V_f \beta_z^f + E_m V_m \beta^m}{E_z^f V_f + E_m V_m} \quad (21)$$

The effect of the thin coating layer is neglected in Eq. (21). The expansion coefficient in the composite transverse direction, β_T , is obtained from radial displacements calculated from the coupled electrochemical-mechanical model

$$\beta_T = \beta_r = \frac{\varepsilon_r}{(c_{f,avg}/c_{f,max})} \quad (22)$$

where ε_r is the radial strain calculated from the radial displacement, u_r , at the outer CCA boundary, Figure 6.

Fracture mechanics

Linear elastic fracture mechanics parameters such as stress intensity factor K and energy release rate G are commonly used to analyze damage propagation in structural materials. Energy Release Rate (ERR) quantifies the net change in potential energy associated with crack extension. Irwin defined ERR as a modified form of the Griffith energy balance

$$G = -\frac{d\Pi}{dA} \quad (23)$$

where Π is the potential energy stored within an elastic body and A is the crack area. Crack extension occurs when G reaches and exceeds a critical value, known as critical strain energy release rate G_C , which is a material property.

For simple geometries, analytical formulas may be derived from beam theory, energy balance or stress intensity factor analyses. For more advanced geometries, numerical solutions are a necessity. There are several techniques implemented in commercial FEM software, where two of the most commonly used techniques include virtual crack closure technique (VCCT) and J- integral.

In this work, where all constituents are assumed to be linear elastic and brittle, the approach for evaluating the ERR is based on VCCT, built-in in ANSYS [41]. VCCT is based on the assumption that the energy needed to separate a surface is the same as the energy needed to close the same surface[42]. The expression for calculation of the Mode I (Figure 8a) ERR is

$$G_I = \lim_{\Delta a \rightarrow 0} \frac{1}{2\Delta a} \int_a^{a+\Delta a} \sigma_y(x) \cdot \Delta u_y(x - \Delta a) dx \quad (24)$$

where σ_y is the stress component related to normal tractions with respect to crack plane at the crack tip, Δa is the crack extension, and Δu_y is the opening displacement at the crack tip.

Similarly, for Mode II (Figure 8b) ERR

$$G_{II} = \lim_{\Delta a \rightarrow 0} \frac{1}{2\Delta a} \int_a^{a+\Delta a} \sigma_{xy}(x) \cdot \Delta u_x(x - \Delta a) dx \quad (25)$$

where σ_{xy} is the shear stress ahead of crack tip, and Δu_x is the relative tangential displacement.

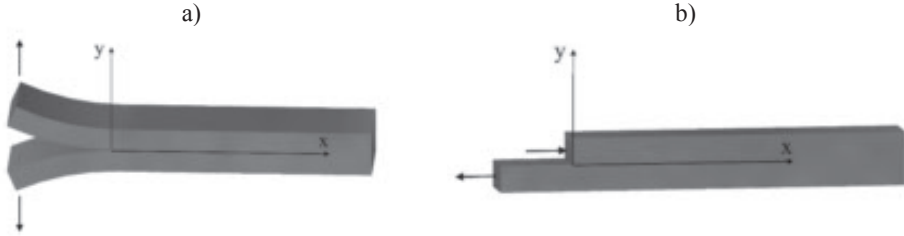


Figure 8. Fracture modes a) Mode I and b) Mode II

The implementation in ANSYS uses the virtual crack-closure method which further assumes that the stress states around the crack tip do not change significantly when the crack grows by a small amount Δa . For the 2-D crack geometry shown in Figure 9, the ERR is defined as:

$$G_I = -\frac{1}{2\Delta a} R_Y \Delta v \qquad G_{II} = -\frac{1}{2\Delta a} R_X \Delta u \qquad (26)$$

where G_I and G_{II} are Mode I and Mode II ERR, respectively, Δu and Δv are relative displacements between the top and bottom nodes of the crack face in local coordinates X and Y, respectively, R_X and R_Y are reaction forces at the crack tip node, and Δa is the length of the element closest to the crack tip. For a 2-D case, the total ERR, $G_{tot} = G_I + G_{II}$.

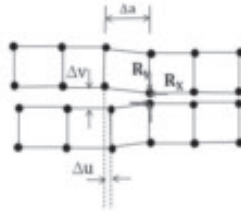


Figure 9. Parameters for VCCT calculation for 2-D crack geometry.

3. Experimental characterization of interfaces

In composites the efficiency of stress transfer from matrix to reinforcement and hence several mechanical properties including compressive strength, strain to failure, damage initiation, fracture toughness and fatigue life depend on fiber/matrix interface [43]. In most cases, fibers are coated with sizing to enhance interfacial properties [44]. For structural battery composites additional requirements are stipulated for the coating in order to achieve multifunctionality. The role of the coating differs depending on material and device design.

For a micro-battery the coating is required to be thin in order to minimize the transport distance, and to be electrically insulating while ion conductive [23]. In a laminated structural battery, the coating may serve as positive electrode [45], with active material deposited onto the fibers.

Many of these novel coating materials are still under development, and the coating techniques are limited by small-scale and batch-wise manufacturing under inert conditions. Hence, the amount of coated fibers produced on lab scale may not be sufficient for macro-specimens to be manufactured and tested according to standards available. Characterization of the interface quality may then take place using modified macro-scale test methods, or tests on micro-scale.

Macro-scale test

The double cantilever beam (DCB) test is the most commonly used method for measuring the initiation and propagation values of Mode I interlaminar fracture toughness, G_I , under static and cycling loading conditions. A tensile load is applied to DCB specimen, containing a through-width non-stick insert (thin film) at the specimen mid-plane. The tensile force (P) acts in a direction normal to the crack surface, and the crack length (a) is closely monitored.

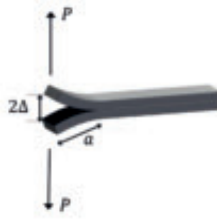


Figure 10. Schematics of the DCB test.

In **Paper V** the mechanical performance of the coating is assessed in DCB test on specially designed unidirectional composites; which are made by embedding LiFePO_4 coated fiber bundles between prepreg layers of commercial UD composite, using the excess resin in the prepreg to impregnate bundles, Figure 11

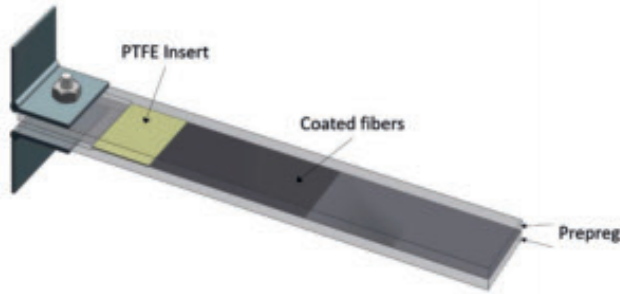


Figure 11. Schematics of the DCB specimen in Paper V. The coated fiber bundles are placed in the mid-plane of prepreg-layers, with a pre-crack created by inserting polytetrafluoroethylene (PTFE)-film at one end of the specimen .

Compliance calibration (CC) method was used for data reduction. The critical strain energy release rate (fracture toughness), G_{IC} , for each crack length was found using [46]

$$G_{IC} = \frac{P_{max}^2}{2b} \frac{\partial c}{\partial a} \quad (27)$$

where P_{max} is the maximum recorded load for each crack length a when the crack start to grow, b is the specimen width and c is the specimen compliance for each crack length.

$$c = 2\Delta/P \quad (28)$$

where 2Δ is the load point vertical displacement, and P is the recorded load.

The compliance as a function of crack length was calibrated using a power function:

$$c = Aa^n \quad (29)$$

where coefficients A and n for the particular specimen are obtained from the compliance (c) versus crack length (a) curve.

Micro-scale test

Commonly used methods to evaluate micromechanical properties of the fiber/matrix interface include a) the single-fiber pull-out test, b) the microbond test, c) the fragmentation test and d) the micro-indentation test, shown in Figure 12, presented below.

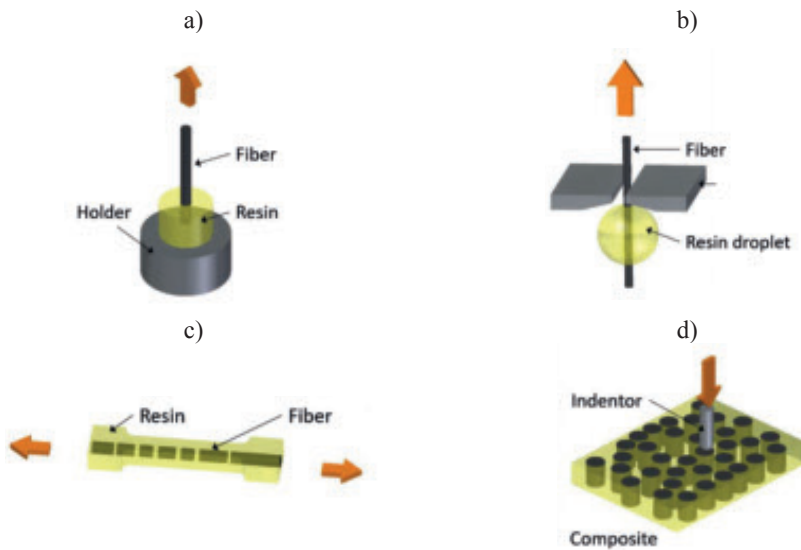


Figure 12. Micromechanical test methods. a) Single fiber pull-out test. b) Microbond test. c) Single fiber fragmentation test. d) Micro-indentation test

Single fiber pull-out test

In this test one end of a single fiber is embedded in uncured resin. The resin is then cured with the fiber in place to produce the test specimen. The test is carried out in a tensile test machine, where the free end of the fiber is gripped and pulled from the resin block.

Microbond test

Like the single fiber pull-out test, the microbond test is a single fiber test, but instead of embedding the fiber in a block of resin, a resin droplet is placed and cured on the fiber. The specimen is placed in a tensile testing machine so that one end (the fiber) is gripped, and the resin droplet is placed between two knife edges. The load is introduced on the resin droplet by the knife edges as the fiber is pulled by the grip.

Single fiber fragmentation

In the single fiber fragmentation test (SFFT) a single fiber is placed at the center of a dog-bone shaped mold, aligned with its longitudinal direction. The mold is then filled with uncured (and degassed) resin. The cured sample is placed in a testing machine and loaded in tension. As the specimen is extended, the fiber will fail repeatedly into shorter and shorter lengths until a saturation is reached and the fiber no longer fails. At the end of the test, the fragment lengths are measured in a light optical microscope.

Micro-indentation test

The indentation test originates from metallurgical micro-hardness test. It can be applied to a cross section of the composite material, the load is applied through an indenter (which is smaller than the diameter of the fiber), and the load-displacement response is recorded.

However, in a round-robin program from 1990s [47], it was found that the scatter within each participating laboratory for the different test methods mentioned above was acceptable, but the scatter between laboratories for a particular test method was high. This result implies that any method of choice can be used to qualitatively characterize different fiber/matrix systems, but the obtained result should not be used for quantitative comparison of results obtained from other laboratories or existing in literature.

The microbond test was selected to study the fiber/SBE interfacial shear strength, and possible changes on the interfacial shear strength induced by electrochemical cycling. This test method was chosen because of the simple character of the test, but also due to the lack of optical transparency of the SBE material, which excludes certain methods, such as the SFFT.

During the microbond tests the droplet is sheared off the fiber as its movement is hindered by a blade acting as barrier. The apparent interfacial shear strength (IFSS) is obtained through

$$IFSS = \frac{F_{max}}{L_e(2\pi r_f)} \quad (30)$$

where F_{max} is the maximum or debonding force, L_e is the length of the embedded fiber inside the droplet, and r_f is the fiber radius.

Unpublished microbond test results in Figure 13 show maximum force, F_{max} , vs embedded fiber length, L_e , for T800 carbon fiber with a) SBE and b) epoxy resin droplets. IFSS values for the two material systems calculated by Eq. (30) are listed in Table 4.

Table 4. Microbond results for T800 carbon fiber with SBE and epoxy resin droplets.

Material system	IFSS value [MPa]
Carbon fiber/SBE	6.9 ± 0.5
Carbon fiber/epoxy	84.4 ± 9.9

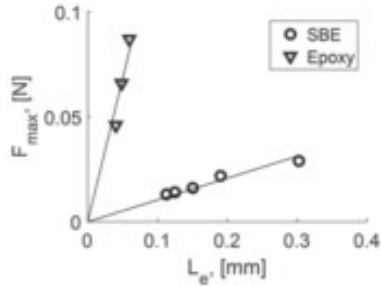


Figure 13. Maximum force F_{max} vs embedded fiber length L_e for T800 carbon fiber with SBE and epoxy resin droplets respectively.

The interfaces of the two systems are different not only for the measured IFSS, which is an order of magnitude lower for carbon fiber/SBE compared to carbon fiber/epoxy. The recorded load - displacement curves for the two systems, Figure 14a and Figure 15a, also show entirely different behavior.

The microbond test on carbon fiber/epoxy, Figure 14a, show an initial steep slope where the blades are in contact with the droplet. The point at which the load instantly drops is where the droplet debonds from the fiber, F_{max} . Afterwards, the load increases to a constant low level which is the frictional force corresponding to when the droplet slides along the fiber after debonding, or fiber break occurs before the sliding takes place, as shown in Figure 14a.

This type of behavior suggest that the achieved interface quality is good. Post-test SEM fractography Figure 14b, shows cracks in the droplet, indicating that failure occurs in the epoxy before it occurs at the interface, i.e. the interface is strong.

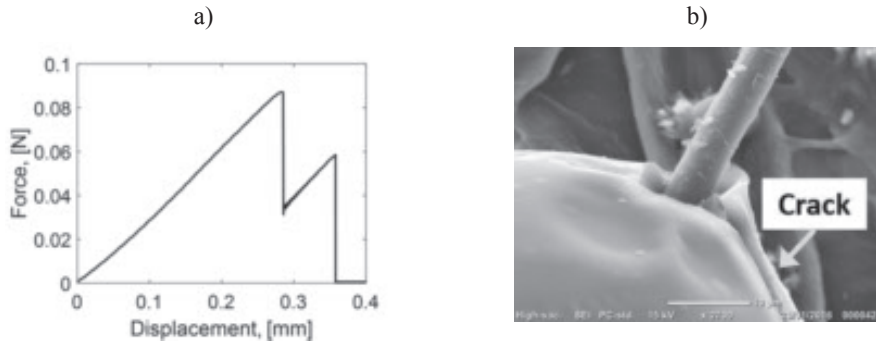


Figure 14. a) Typical load - displacement curves for carbon fiber/epoxy. b) Post-test SEM picture of the droplet and fiber with epoxy residues.

For the SBE droplet (Figure 15b) the load at debonding, F_{max} , is not followed by a drop in force and F_{max} is actually smaller than the frictional force after the debonding when the droplet slides along the carbon fiber.

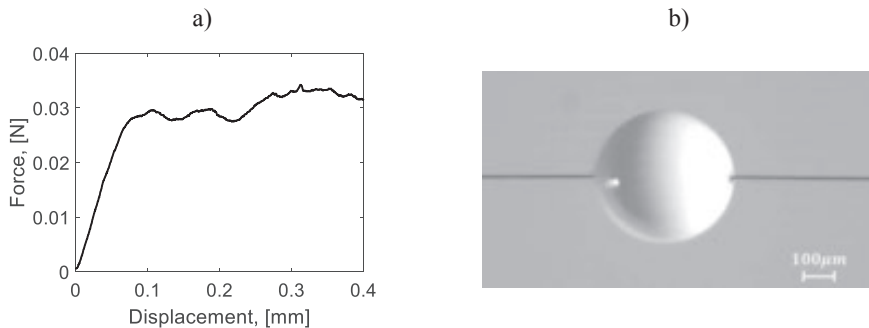


Figure 15a) Load-displacement curve from the microbond test on b) SPE droplet on carbon fiber prior to testing.

4. Scope of the thesis

The objective of this thesis is to develop a multi-physics based model to predict the effects of combined electrochemical charging/discharging and mechanical loading on structural composite battery materials. The modeling addresses effects of Li transport both within and between battery electrodes, to investigate the resulting local mechanical stress distribution in the constituents.

For this purpose, the same three-phase concentric cylinder assembly representation of the material was used for modeling electrochemical processes in the battery cell and the mechanical stresses arising due to charging/discharging.

This work also aims to gain understanding of the failure forming events for this novel type of composite material, induced by volume changes from intercalation. As the stresses due to charging and discharging can be very high, microdamage may initiate and grow without any applied external load. To study possible micro-cracking scenarios, models with multiple fibers and multiple fibers embedded between layers of different orientation was employed. Linear elastic fracture mechanics was used to analyze radial matrix crack propagation and debonding at coating/matrix interface in both unidirectional (UD) and cross-ply laminate, under electrochemical load only and combined electrochemical and thermomechanical load.

5. Summary of papers

In **paper I** a framework for modeling a structural micro battery is presented. Mathematical formulation for a cylindrical single lithium-ion battery cell under operation describing the electrochemical processes occurring is presented. A model was set up and solved in COMSOL Multiphysics [30]. The modeled electrochemical processes include (i) mass transport in electrolyte and active electrode material particles, (ii) electrochemical reaction at active electrode material surfaces and (iii) electronic and ionic conduction.

Equations to describe the spatial and time dependent variation in the potential as well as in the lithium ion concentration in the solid and electrolyte phases are formulated and analyzed on different length scales. It is assumed that the matrix (positive electrode) consists of several phases: an electronically conductive phase, an active material phase and the electrolyte phase. The governing mechanism in each particular phase is modeled. Electrons are transported in the conductive phase, and Ohm's law is used to describe the potential gradients in the solid phase. In the active material, Li is assumed to be transported by diffusion, and described by Fick's second law. In the electrolyte phase ions are transported by both diffusion and migration. The solid and electrolyte phases are linked by the conservation of charge. The multi-scale character of the battery is addressed by coupling equations solved across the battery cell macroscopic domains; fiber electrode, coating separator and matrix electrode, and microscopic domains: active electrode particles. Equations associated with the processes in the electrolyte and the potentials are solved to find the dependency on the radial coordinate in the macroscopic domains. The lithium concentration within the active materials in the matrix is solved in the microscopic domain. The effect on electrochemical and mechanical performance of altering the fiber volume fraction and the matrix composition in the structural battery was investigated, focusing on the radial

swelling and specific capacity. Two scenarios were analyzed: 1) assuming that the electrochemical cycling begins with a pristine fiber and the active material in the matrix is fully lithiated at stress-free state and 2) the electrochemical cycling starts with the fiber fully lithiated and all host sites for Li in the matrix material being empty.

In the first scenario, the maximum dimensional change occurs when the battery is fully charged.

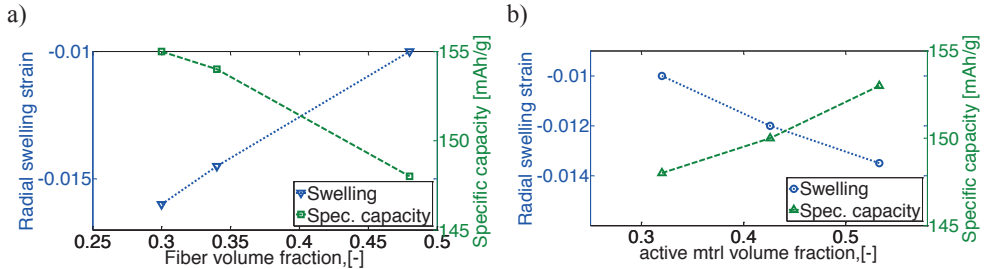


Figure 16. Radial swelling strain and specific capacity versus a) fiber volume fraction and b) volume fraction of the active material in the matrix for $V_f = 0.34$.

In Figure 16a the maximum shrinkage of the micro-battery in the radial direction is shown for different fiber volume fractions. For $V_f < 0.34$ there is more Li available in the matrix material than can be intercalated into the carbon fiber, and for $V_f > 0.34$ more available intercalation sites are available in the fiber than Li present in the system. The global dimensional change in the radial direction is negative, due to the shrinkage in the matrix material being greater than the radial expansion of the fiber, which is also the reason for higher V_f resulting in lower shrinkage. In Figure 16b radial swelling strain and the capacity normalized to the amount of active material in the cathode is shown for different volume fraction of the active material. Both the specific capacity and radial swelling strain is increasing with increasing ε_s^+ . Since the amount of active material in the matrix governs the available amount of Li for intercalation in the fiber, it naturally follows that the swelling is less for a lower volume fraction of the active material.

Theoretically, another stress-free state can be assumed (Scenario 2) when fiber is fully lithiated and all host sites for Li in the matrix material are empty. The corresponding maximum volume change then occurs at full discharge (cut-off voltage). Where the dimensional change in the radial direction of the battery is positive because the swelling of the matrix is greater than the shrinkage of the fiber, which dominates the global behavior. In general, the swelling decreases with increasing V_f , because the amount of matrix material surrounding the carbon fiber decreases, thus reducing its ability to withstand both the fiber displacement while the matrix itself also swells less due to lower lithium concentration. However, as shown in Figure 17, the radial swelling is also decreased for very low V_f . This is explained by the distance in the radial direction of the matrix material being too large to allow for efficient transport of Li^+ in the electrolyte phase for intercalation in the active material.

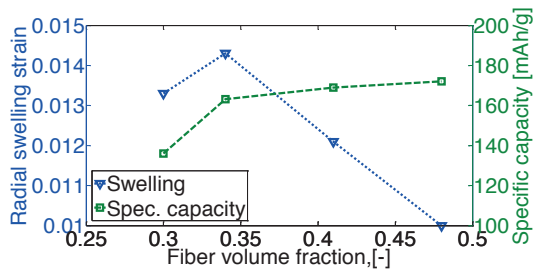


Figure 17. Fiber fully lithiated from start, radial swelling strain at cut-off voltage and specific capacity dependence on fiber volume fraction.

In **Paper II** the effect of carbon fiber diffusion coefficient on Li distribution for different charge current was studied numerically. The resulting stress distribution in the carbon fiber and at the solid/electrolyte interface was analyzed for different elastic constants. The discharge current is expressed as a C or C-rate in order to normalize against battery capacity. A C-rate is a measure of the rate at which a battery is discharged relative to its maximum capacity, 1C means that the discharge current will discharge the entire battery in 1 hour.

For a 1C charge rate with a slow Li diffusion in the fiber, small Li concentration gradient is present during charging, with higher Li concentration at the fiber surface than on the fiber axis. The normalized concentration in the fiber never reaches 1, because of the conservatively set upper cut-off voltage. When the discharging starts, the Li concentration is first reduced at the fiber surface, whereas in the region close to the fiber axis the concentration is still slightly increasing, a process driven by the previously created concentration gradient. With continued discharging the Li concentration is always lower in the fiber surface region. In contrast, when the diffusion is fast the concentration gradients in the fiber are negligible.

At 10C charge/discharge a slow diffusion in the carbon fiber lead to highly non-uniform concentration in the fiber, with changing slope dependent on the charge/discharge progression. Fast diffusion in the carbon fiber gives uniform concentration distributions at 10C.

The mechanical stresses are obtained by assuming generalized plane strain conditions. The carbon fiber is considered stress free with no Li present. i.e. at fully discharged state. The matrix material is also stress free in the discharged state, when it contains the highest lithium concentration. There are two mechanisms governing the stresses, i) the interaction between constituents and ii) the non-uniform Li concentration distribution in the fiber.

Figure 18 shows the stress distribution in the fiber for a 10C charging when the upper voltage limit is reached, which is the maximum deviation from the initial stress-free condition. The

corresponding stresses at the coating/matrix interface($r = r_c$) and matrix outer boundary ($r = r_m$) are listed in Table 5.

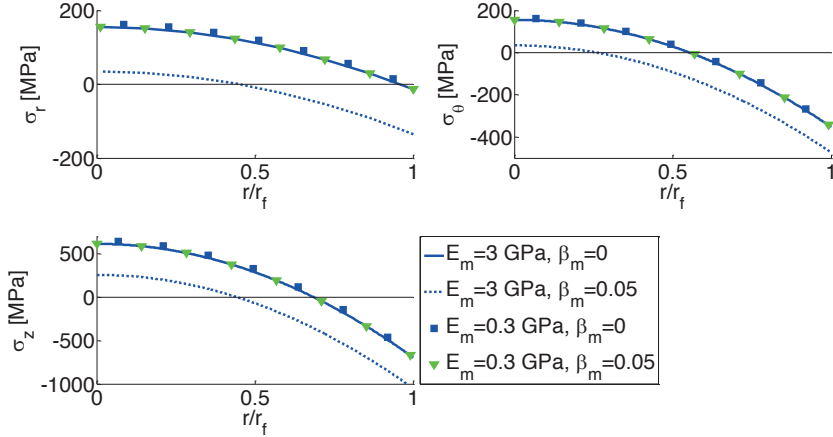


Figure 18. Stress distribution along the fiber radial direction at full charge with 10C charge rate.

For a 10C charging/discharging rate, when the Li transport is not sufficiently fast, higher stress gradients are expected, because of large Li concentration gradients. For hoop and axial stresses, the fiber center experiences tensile stresses while the outer part of the fiber is under compressive loading, this is due to the non-uniform Li concentration distribution creating a Li-rich shell exerting additional forces on the Li-poor fiber core. For a low modulus matrix the effect of swelling in the matrix has very limited effect on the stress distribution in the fiber, whereas for a stiff matrix the swelling has significant influence. This is valid during the entire charging. At discharge the stress state is reversed, resulting in tensile axial and hoop stresses at the outer fiber parts.

Table 5. Stresses at the coating/matrix interface and outer boundary at full charge for 10C charging.

E_m [GPa]	β_m [-]	$\sigma_r(r = r_c)$ [MPa]	$\sigma_\theta(r = r_c)$ [MPa]	$\sigma_\theta(r = r_m)$ [MPa]	$\sigma_z(r = r_c)$ [MPa]	$\sigma_z(r = r_m)$ [MPa]
3	0.05	-129.9	281.7	148.3	215	211.5
3	0	-52.9	113.9	61.0	41.6	41.6
0.3	0.05	-13.2	28.7	15.1	29.1	21.5
0.3	0	-5.4	11.6	6.2	4.2	4.2

The dependency of stresses on matrix stiffness and swelling coefficient is evident. The most noticeable difference between a matrix that shrinks during charging and one that does not is the enormous tensile axial and hoop stresses arising in the matrix during charging. In the presented example these stresses are significantly higher than typical tensile strength values for polymers. The high tensile hoop stress when the matrix is shrinking during charging, indicate that radial cracks initiation at the coating-matrix interface or in the matrix is a possible damage mechanism to consider.

In **paper III** multiphysics simulations and linear elastic fracture mechanics was used to study the propagation of radial matrix cracks and debond at the coating/matrix interface in unidirectional structural micro-battery composite under electrochemical loading only. It was shown that assuming uniform Li distribution in the fiber and matrix at the end of charging, the resulting stress distribution in the constituents is in good agreement with the stress distributions obtained from multi-physics calculations. Hence, a simplified modeling strategy can be employed. Stress analysis shows that the high hoop stress in the matrix at the coating/matrix interface during charging time, t , may be a reason for radial matrix cracks initiating at the coating/matrix interface, Figure 19b.

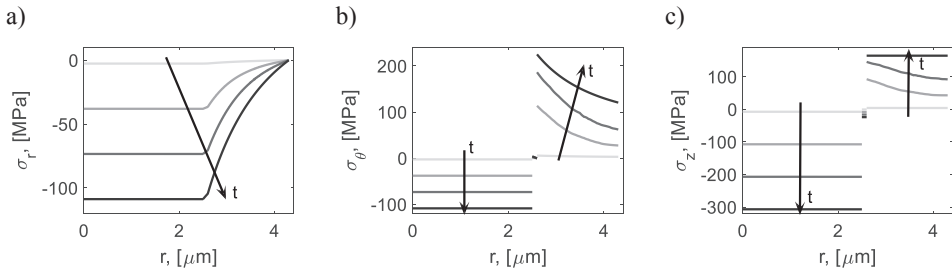


Figure 19. Stress distribution during charging. a) radial stress. b) hoop stress. c) axial stress.

Propagation of these cracks was studied by calculating Energy release rate (ERR) assuming square packing of fibers. For a micro-battery (unit in the structural composite) containing electrodes balanced with respect to storage capacity, $V_f = 0.338$, results show that the crack growth towards the nearest fiber in $\theta = 0^\circ$ direction, (see Figure 20 for notation), is unstable, whereas the crack growth in the $\theta = 45^\circ$ direction includes both stable and unstable propagation regions. The ERR for growth in $\theta = 0^\circ$ direction is larger.

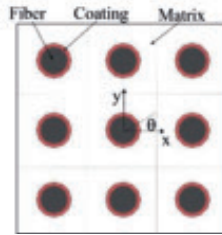


Figure 20. Square packing of fibers.

Composites with higher V_f have the same trends, but with lower G_I values, Figure 21b.

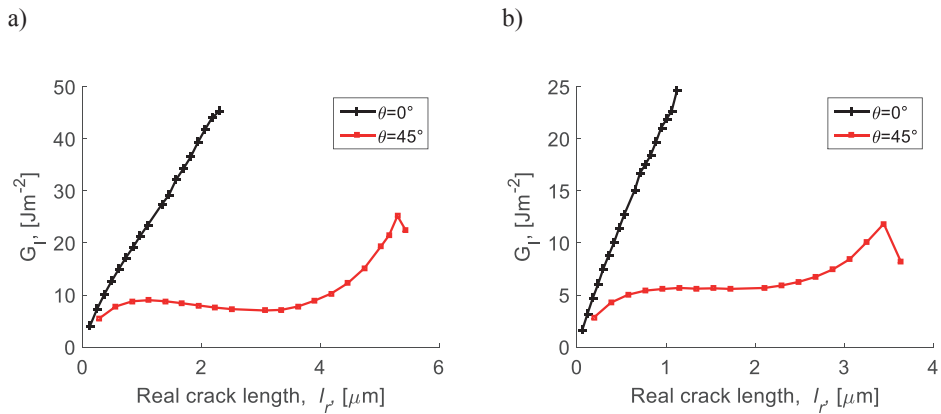


Figure 21. Variation of Mode I ERR as a function of the radial crack length for growth in different directions for a) the reference case $V_f = 0.338$, and b) $V_f = 0.482$.

For the undamaged composite radial stresses at the fiber boundary are compressive during both charging and discharging, meaning that debonding is not risked. However, with a radial crack present, the stress distribution changes, Figure 22. The radial stress distribution is very similar to that without damage, compressive along the entire interface; except for a very local radial crack tip region where it is tensile and very high, Figure 22a, and the high tensile radial stresses region slightly increases for long cracks. The shear stress distribution along the interface is greatly affected, due to the presence of a radial crack, leading to large values not only at the radial crack

tip but in a large region, Figure 22b, where $l_{r,n}$ is normalized length of the matrix crack. The combined action of high tensile radial stresses and shear stresses near the tip of the crack is a very probable cause for initiation of small debonds.

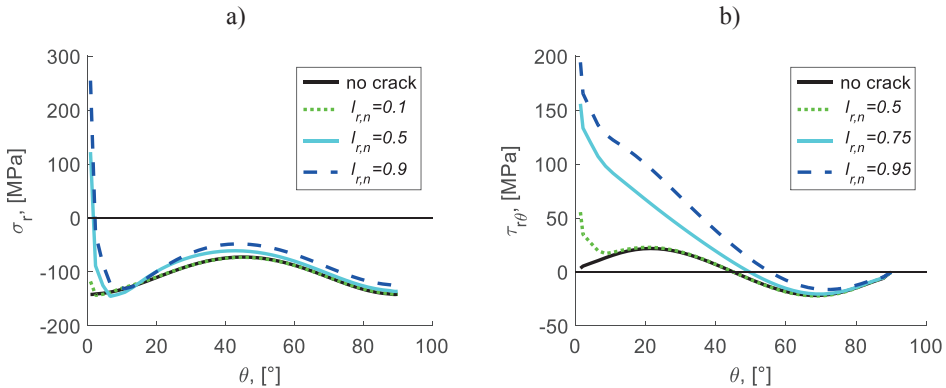


Figure 22. a) Matrix radial stress distribution at coating/matrix interface. b) Matrix shear stress distribution at coating/matrix interface

Results for ERR show that the debond crack growth, Figure 23a, is governed by Mode II, Figure 23b. The ERR values for the interface crack growth are of an order of magnitude lower than for the radial matrix crack growth.

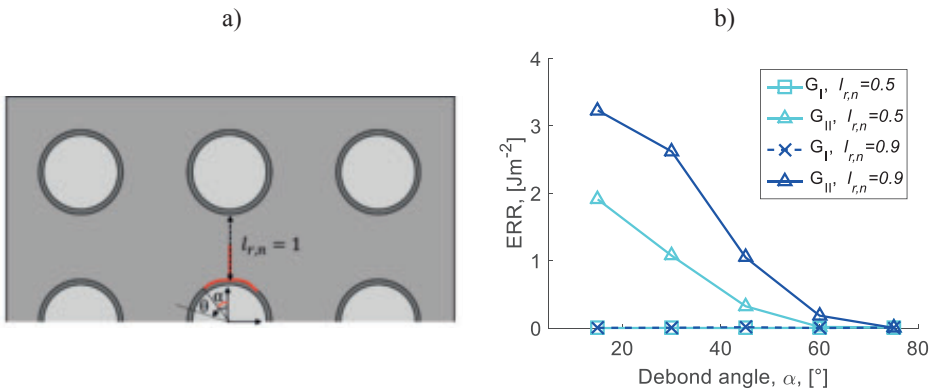


Figure 23. a) Schematic of coating/matrix debonding in the presence of a radial matrix crack. b) ERR of debond crack subjected to electrochemical loading.

In **paper IV** damage formation in a cross-plyed structural composite battery under pure electrochemical and combined electrochemical and thermomechanical ($\Delta T = -80^\circ\text{C}$, $\varepsilon_x = 0.5\%$) loading was studied. 2D FEM models assuming square packing of fibers in the 90° -ply and homogenized properties for the 0° -ply were used to analyze radial crack propagation in the matrix material and debonding at coating/matrix interface, Figure 24a. Crack propagation was studied by calculating Energy Release Rate (ERR). For a micro-battery with fiber content $V_f = 0.338$, results show the crack growth towards the nearest fiber in both x-direction (horizontal crack) and y-direction (vertical crack) is unstable, Figure 24b, with crack growth in the y-direction much more probable.

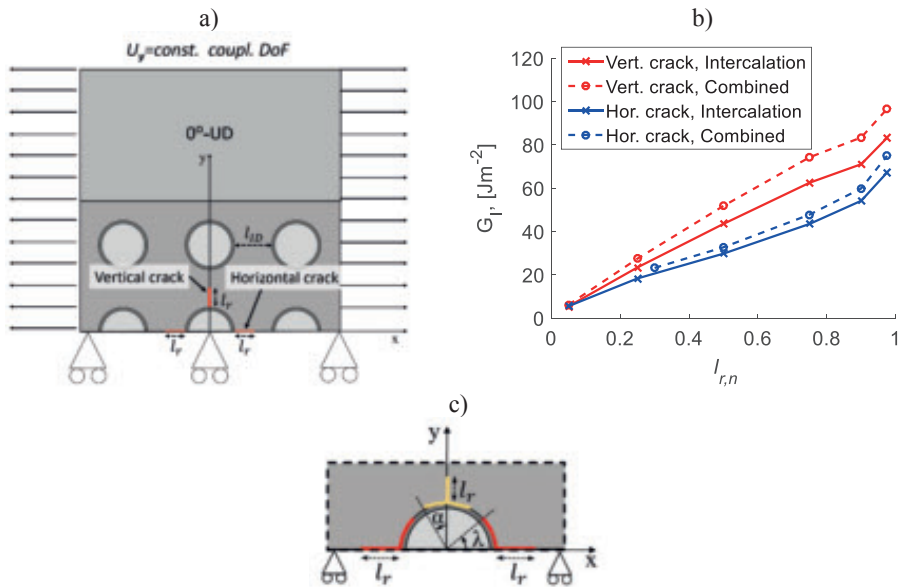


Figure 24. a) Schematics of 2D model with matrix cracks. b) Mode I ERR for matrix crack. c) Details of the debonds originating from matrix cracks.

Large tensile radial and shear stresses at the coating/matrix interface, in the presence of matrix cracks make the debonding relevant for consideration, Figure 24c. The debond crack growth is in

mixed mode, Figure 25-Figure 26, both for the pure electrochemical load and combined load, for both matrix crack paths.

For debonds originating from vertical matrix crack under pure electrochemical loading, small debonds ($\alpha < 30^\circ$) are governed by the Mode II ERR component (G_{II}), Figure 25b, increasing with the debond angle until reaching a peak value at approximately $\alpha = 30^\circ$, then G_{II} starts to decrease with increasing debond angle α , approaching zero for very large debonds.

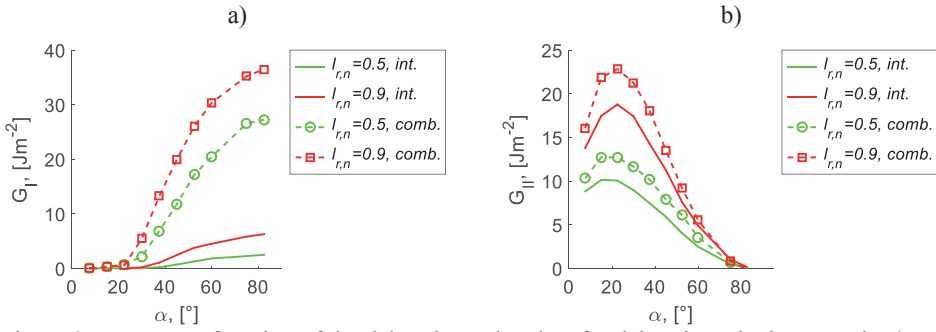


Figure 25. ERR as a function of the debond angular size, for debond crack along coating/matrix interface originating from vertical matrix crack under pure intercalation (solid lines) and combined loading (dashed lines): a) Mode I ERR and b) Mode II ERR.

The Mode I ERR component G_I , Figure 25a, remains insignificant until the same $\alpha = 30^\circ$, where G_I starts to grow with increasing debond angle α . Added thermomechanical load changes the mode ratio (G_I/G_{II}) for the debond. Mainly Mode I ERR for debonds $\alpha > 30^\circ$ is increased considerably, due to the applied thermomechanical load, $\epsilon_x = 0.5\%$, acting normal to the crack plane for large debond angles α . The increase in Mode II ERR follows the same trends as for the case of only intercalation load, but with magnified values.

In Figure 26a- Figure 26b the mixed mode character of the debond growth with and without horizontal matrix crack is shown for the two load cases. For intercalation only, G_I is increasing with increasing debond angle λ for small debonds ($\lambda \leq 30^\circ$). For large debonds ($\lambda \geq 60^\circ$) G_I is greatly reduced, as the debond crack growth direction becomes almost parallel with the x-axis,

while generating the maximum value for G_{II} . The impact of the increasing horizontal matrix crack length $l_{r,n}$ on the ERR for debonding is increasing G_I . The effect of matrix crack length on G_{II} is more complex: for small debonds it significantly increases but for large debonds it decreases.

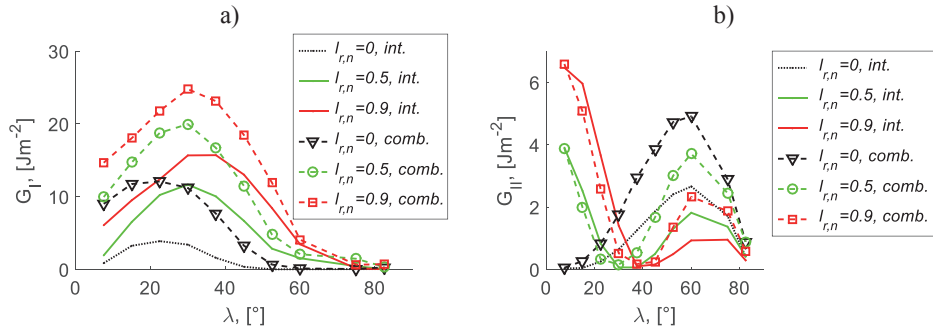


Figure 26. ERR as a function of the debond angular size, for a debond crack along coating/matrix interface originating from horizontal matrix crack under pure intercalation (solid lines) and combined intercalation and thermomechanical load (dashed lines): a) Mode I ERR and b) Mode II ERR.

The impact of the added thermo-mechanical loading on Mode I ERR (Figure 26a) is substantial, especially for debonds $\lambda \leq 40^\circ$, which is when the debond crack can be regarded as near-perpendicular to the direction of the applied load. For large debonds ($\lambda \geq 60^\circ$), the crack growth direction is near parallel with the x-axis, reducing G_I regardless of the added loads in the x - direction.

The ERR values for the interface crack growth are lower than for the radial matrix crack growth. Therefore, the most probable sequence of failure event in the cross-ply laminate are: 1) vertical radial matrix crack initiation and unstable growth; 2) debond is initiated at certain length of the matrix crack and propagates in a mixed mode manner. These results suggest that the course of events for a macro-scale transverse matrix crack formation is different for a structural composite battery in comparison to a conventional cross-ply composite.

In **paper V** a methodology for assessing the fiber/coating adhesion of the novel coated material systems is presented. Since most coating techniques used for the development of multifunctional composite materials are limited by small-scale and batch-wise manufacturing under inert conditions [24,48,49], the amount of coated fibers from these setups is not sufficient for macro-specimens to be manufactured and tested. By embedding the coated fiber bundles between prepreg layers of commercial UD composite, and allowing the excess resin in the prepreg to impregnate the bundles, DCB tests can be carried out to evaluate the coating adhesion properties. The measured Mode I fracture toughness, G_{IC} , reflects possible combination of failures at all interfaces and/or in the matrix and in the coating, Figure 27.

Post-test Scanning Electron Microscopy (SEM) fractographic analysis of the fracture surface was used to correlate the highly different G_{IC} values with actual failure mechanisms and their sequence.



Figure 27. Possible damage initiation sites along the test specimen, at *i*) fiber/coating, *ii*) coating/matrix interfaces, in the *iii*) coating and *iv*) matrix.

G_{IC} values for three tested specimens are shown in Figure 28. While G_{IC} is stable with increasing crack length for two of the specimens, DCB-1 and DCB-2, but with widely different values, at around $500 J/m^2$ and $200 J/m^2$, a leaping behavior can be found for DCB-3, with values ranging between these two extreme values.

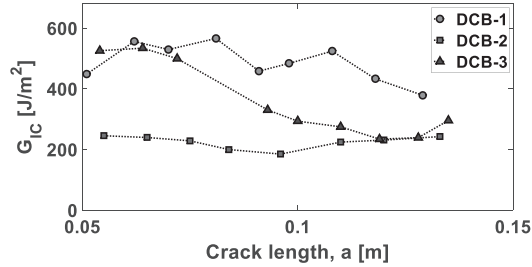


Figure 28. Critical strain energy release rate.

The variations in measured G_{IC} can be attributed to varying coating thickness between bundles and within each bundle. The current non-standardized coating process by electrophoretic deposition of $LiFePO_4$ on carbon fiber results in large variation of coating thickness along fiber, between fibers in each bundle and between bundles.

Fractographic studies of the pulled-out fibers and fiber imprints on the fracture surface show that for the used material, the fiber/coating interface is the weakest among all interfaces.

It was found:

- 1) $G_{IC} = 200 J/m^2$ corresponds to thick coatings. The failure mechanism is debonding between fiber and coating, with a clean fiber surface, Figure 29.

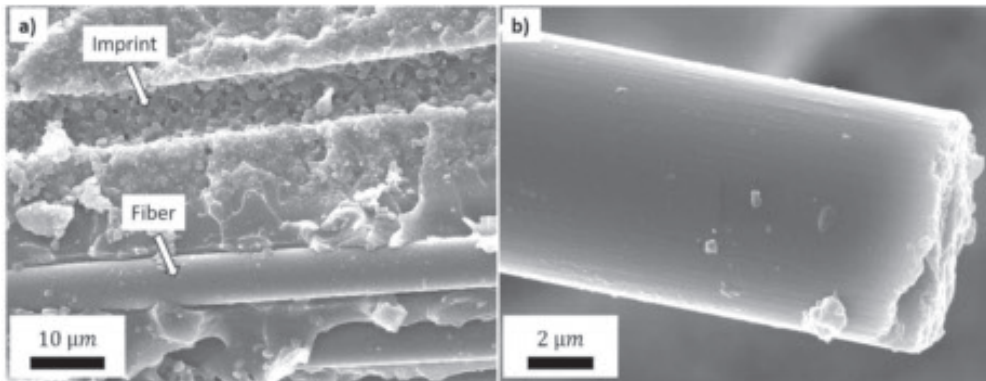


Figure 29. Fracture morphology of specimen with low strain energy release rate (G_{IC}). a) imprint of fiber and fiber with coating particles and b) clean fiber surface.

- 2) $G_{IC} = 500 \text{ J/m}^2$ corresponds to thin coatings. Heterogeneity of the coating is high (the particle size is comparable with the coating thickness), and the fiber/coating crack deviates in the coating reaching the coating/matrix interface and returning to the fiber/coating interface. The real crack path is longer and crosses regions with higher fracture toughness.

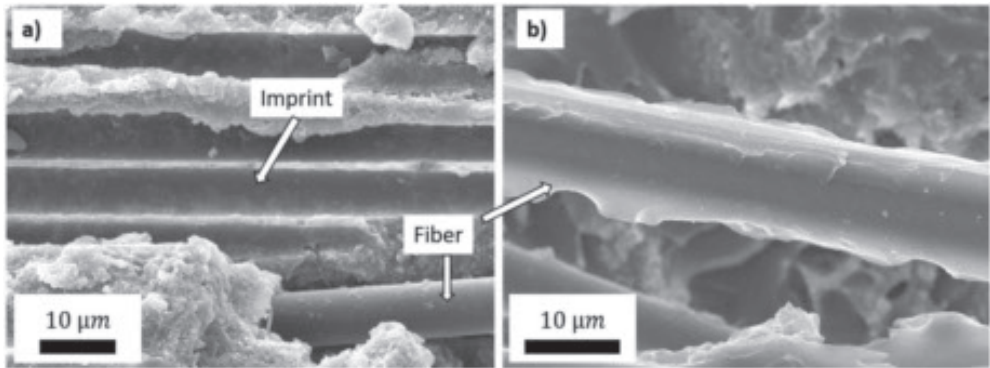


Figure 30. SEM picture of fracture surface specimen with high strain energy release rate (G_{IC}).
a) imprint of fiber, and fiber in the coated part of the specimen b) fiber surface with rests of resin.

6. Future work

The ultimate goal is for the multifunctional composite to be implemented in applications where its weight reduction on system level can be demonstrated and benefited. To achieve this, further interdisciplinary research is required. The work ahead may roughly be categorized into “practicalities” and “understanding”.

One aspect of practicalities is to include other necessary materials besides electrodes and electrolyte to get a functioning and safely operating structural composite battery. These additional materials/functions include proper packaging of battery cells, cell connectors, enabling electrical connection between electrodes and external circuit via terminals, safety installations and ancillary equipment (monitoring, thermal management, venting system). Another aspect is the ability to manufacture these structural battery (full) cells, and scale up the manufacturing in ambient conditions.

In this section, a selection of some challenges ahead is presented, focusing in particular on understanding certain mechanisms in order to improve modeling.

Radial fiber swelling

The carbon fiber used in this novel multifunctional material, is actually developed to fit a monofunctional purpose; the mechanical performance, meaning that there is a lack of comprehensive understanding of how these fibers function under interacting electrochemical and mechanical processes. Research has been devoted to understanding the impact of the intercalation on the stiffness, strength and expansion of intermediate modulus (IM) carbon fibers [14]. The reason for the superior electrochemical performance of IM carbon fibers over its high modulus (HM) counterpart reported by [13], is the differences in carbon fiber microstructure [50]. High-

resolution transmission electron microscopy and *in - situ* Raman spectroscopy on individual carbon fiber show that the storage capacity of the fiber is favored for small crystallite with limited directional orientation, which is the case of IM carbon fibers. Whereas for HM fiber with larger crystallites which are highly oriented in the fiber direction, the storage capacity is on the order of half of that of the IM fiber. By understanding how the size and orientation of the crystallite relates to the intercalation mechanisms, just like the relationship between the stiffness/strength of the fiber and its microstructure has been known for long, enables development of new carbon fiber with a multifunctional intention, by tailoring the graphitic crystallite size and order. However, as has been shown in this thesis, it is the fiber's swelling due to the intercalation that give rise to high stresses in the matrix (much higher than for a conventional composite). This suggests that the swelling coefficients should be included as an important parameter when the fiber's properties are tailored to be used in a structural battery. The data on the radial swelling [51] serve as a good indication of the large swelling, but it is actually not entirely reliable since there is no method for measuring the transverse swelling in a similar way to that of the longitudinal swelling. Hence, methods for studying the radial fiber swelling (*in - situ*) remain to be developed.

Characterization of structural battery electrolyte

The methods for so called full characterization of the transport properties of the electrolyte are time consuming and experimentally difficult, and the factors affecting the accuracy are not well understood [7,52]. Consequently, such investigations despite their importance are rarely undertaken and published. A full characterization consists of a series of experiments, including conductivity measurements, concentration cells, galvanostatic polarization experiment and diffusion experiments, from which the ionic conductivity, diffusion coefficient and the transport

number are extracted. In order to validate and improve the modeling a full characterization of the SBE is required. In addition, as a transition from UV-curing to heat curing appears as a necessity for multilayer structural composite laminates [53], the coefficient of thermal expansion (CTE) of the neat resin must be measured, to be able to take the residual thermal stresses into account,

Matrix material – a multifunctional particulate composite

It is necessary to validate the mechanical performance of the multifunctional matrix material, intended as the positive electrode material. Primarily, it must be ensured that the particulate composite material transfers load both in an intercalated and de-intercalated state. Furthermore, understanding of how the active material particle size and volume fraction affects the interacting electrochemical and mechanical performance enables tailoring the multifunctional performance of the matrix material.

By decreasing the LiFePO_4 (or other active material used in the cathode) particle size, the diffusion time of Li in the active material will shorten, resulting in enhanced power performance. At the same time, reduced particle size is associated with an increase in undesirable side reactions due to higher surface area, resulting in poor cycling performance. Thus, there is a trade-off in particle size regarding electrochemical performance.

Likewise, there are trade-offs for the mechanical performance as well. The mechanical properties of particulate-polymer composites depend strongly on the size and volume fraction of the reinforcing particles, the particle-matrix interface adhesion and the degree of particle dispersion. While small particles allow for higher volume fractions, which increase elastic and fracture properties of the composites, it also causes higher viscosity and particle agglomeration before curing [54]. In [55] the introduction of two different particle sizes in the same matrix showed improved strength and fracture toughness while lowering the viscosity and thus allowing for a

more uniform particle dispersion compared to its single-particle-size counterpart, as the presence of large particles showed a de-agglomeration effect. It is possible that two different particle sizes of the active material are advantageous also for the battery application, since some of the particles do not become fully intercalated, thereby reducing the total volume change.

Particulate polymer composites are noted to show mechanical properties which depend on time, rate and temperature [56,57]. The time dependent behavior of the multifunctional LiFePO_4 reinforced composite remains to be characterized. Most commonly used methods to characterize materials viscoelastic and viscoplastic behavior is the tensile creep test, where a constant stress is applied to the specimen, and strain is recorded as a function of time.

Testing on bundle vs individual fiber

Electrochemical cycling performance tested both on individual fiber scale and for the fiber bundle show that there is a size effect [58]. The difference is clear for faster charge/discharge rates, while the performance is very similar for slow charge/discharge rates. Similarly, it may be of interest to investigate differences in mechanical performance with respect to any size effect. In [53] the impact of ion transport on the fiber/SBE interface was tested on macro-scale, for UD laminas of spread carbon fiber tows embedded in SBE. Electrochemically cycled specimens and non-cycled specimens were tested in three-point bending, the measured transverse stiffness showed no statistical difference, suggesting no losses in mechanical properties due to ion transport in the SBE and SBE-to-carbon fiber interface. Test on micro-scale can be used to validate these results, for which the microbond test is especially suitable. The microbond test allows for qualitative assessment of the effect of intercalation on interface strength, for lithiated and delithiated carbon fiber.

The longitudinal stiffness measured on dry fiber bundles, showed no effect of intercalation [59]. However, while the stiffness remained unchanged an increase in cross-section area of the fibers was observed when lithiated. Indicating that there is an actual decrease of the fiber axial modulus due to intercalation. Single fiber tensile test can be useful to capture this change in stiffness, since is difficult to measure on bundles with unknown filaments and no strain gauge or extensometer. There is also a possibility to extract the fiber stiffness change from the linear part of the recorded load-displacement curve during the microbond test. By performing a compliance calibration, i.e. perform tests on specimens with different gauge lengths, taking the additional displacement artefacts from the test machine into account, will reduce the impact of lack of strain gauges. The fiber stiffness, E_1 , corrected with respect to compliances can be calculated from

$$E_1 = \frac{L_0}{C * A} \quad (31)$$

where L_0 is the initial fiber length, A is the average fiber cross section area and C is the true compliance, determined by subtracting the system compliance obtained from compliance calibration, C_s , from the apparent compliance for each specimen, C_a .

Temperature effects

Conventional batteries have a narrow temperature window for optimal operation. Deviating from this temperature span impairs the battery performance and/or life. The temperature limitation in a structural composite battery also needs to be identified and understood, as it governs the battery performance, safety and aging, as well as giving rise to thermal stresses and lowering the mechanical performance.

Thermal modeling coupled with battery modeling is a useful tool to study temperature effects in batteries. The thermal model is based on thermal energy balance:

$$\rho C_p \frac{\partial T}{\partial t} = \nabla \cdot (k \nabla T) + Q \quad (32)$$

where ρ is the density, C_p is the heat capacity, k the thermal conductivity and Q the heat generation rate. Heat is generated from overpotentials (i.e. deviations from the equilibrium potential during battery operation) and resistances, which means that Q is a function of solid phase potential in the matrix, $\Phi_{s,m}$, electrolyte phase potentials in coating and matrix, $\Phi_{e,c}$, and $\Phi_{e,m}$, molar fluxes J_f and J_m , salt and solvent concentrations in coating and matrix, c_{solv} and c_{solv} , and Li concentration in fiber and LiFePO₄ active material particles, c_f and c_p . Averaged values for the temperature and generated heat can be used to couple the battery and thermal model, Figure 31.

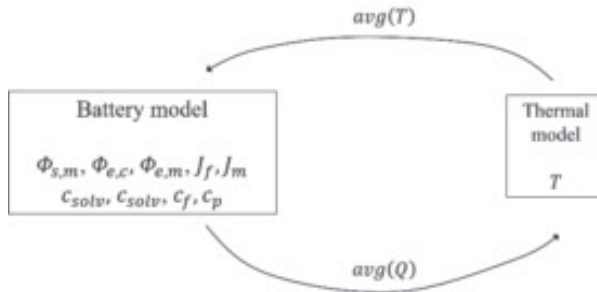


Figure 31. Coupling between the battery and thermal model using the average values for the temperature and generated heat

Solid Electrolyte Interface/Interphase (SEI)

The electrode/electrolyte interface is one of the main parameters governing the safety and lifetime of the battery. During charge, lithium ions supported by solvent molecules approach the surface of the graphite, as the lithium ions are intercalated into the graphite sheets; the potential of the negative electrode is very low, there is a thermodynamic driving force for electrolyte reductions, leading to formation of decomposition products that deposit on the surface. This layer

on the graphite surface is called solid electrolyte interface (SEI)-layer. The SEI layer formation is both detrimental and essential for the battery. On one hand, the SEI layer increases the cell's internal impedance. But on the other hand, the SEI acts as a protective barrier on the graphite allowing the battery to function properly. The SEI layer is permeable to lithium ions but not to electrons, meaning that further degradation of the electrolyte is avoided.

The thickness of the SEI layer in conventional batteries is not uniform and it increases with age, resulting in an increase of the cell's internal impedance; reducing its capacity and hence its cycle life. It remains to be investigated how this SEI layer behaves in a structural composite battery, as graphite is replaced with carbon fiber and the SBE replaces liquid electrolyte. Two questions should be answered: 1) Does the SEI form at all? 2) To what extent does the introduction of this new phase (and especially two new interfaces formed) impact the material load carrying ability and electrochemical performance?

In case the impact of the SEI layer is too prominent to neglect, formation of the SEI layer can be incorporated in the battery model, as demonstrated by Ekström and Lindbergh [60].

Bibliography

1. Chapter 7 - Defects and damage and their role in the failure of polymer composites. In: Greenhalgh ES, editor. *Failure Analysis and Fractography of Polymer Composites*: Woodhead Publishing, 2009.
2. Joffe R. Damage accumulation and stiffness degradation in composite laminates. Doctoral Thesis, Luleå, Luleå University of Technology, Department of Engineering Sciences and Mathematics, Material Science, 1999.
3. Garrett KW, Bailey JE. Multiple transverse fracture in 90° cross-ply laminates of a glass fibre-reinforced polyester. *J Mater Sci* 1977;12(1):157-168.
4. Zhang H, Ericson ML, Varna J, Berglund LA. Transverse single-fibre test for interfacial debonding in composites: 1. Experimental observations. *Compos Part A Appl Sci Manuf* 1997;28(4):309-315.
5. Bard AJ, Faulkner LR. *Electrochemical methods : fundamentals and applications*. New York: Wiley, 2001.
6. Quartarone E, Mustarelli P. Electrolytes for solid-state lithium rechargeable batteries: Recent advances and perspectives. *Chem Soc Rev* 2011;40(5):2525-2540.
7. Lundgren H. *Thermal Aspects and Electrolyte Mass Transport in Lithium-ion Batteries*. PhD Thesis, Stockholm, KTH, Applied Electrochemistry; KTH, Applied Electrochemistry, 2015.
8. Gibson RF. A review of recent research on mechanics of multifunctional composite materials and structures. *Compos Struct* 2010;92(12):2793-2810.
9. Asp LE, Greenhalgh ES. Structural power composites. *Composites Sci Technol* 2014;101:41-61.
10. Snyder JF, Gienger EB, Wetzel ED. Performance metrics for structural composites with electrochemical multifunctionality. *J Compos Mater* 2015;49(15):1835-1848.
11. Ekstedt S, Wysocki M, Asp LE. Structural batteries made from fibre reinforced composites. *Plast Rubber Compos* 2010;39(3-5):148-150.
12. Liu P, Sherman E, Jacobsen A. Design and fabrication of multifunctional structural batteries. *J Power Sources* 2009;189(1):646-650.
13. Kjøll MH, Jacques E, Zenkert D, Behm M, Lindbergh G. PAN-based carbon fiber negative electrodes for structural lithium-ion batteries. *J Electrochem Soc* 2011;158(12):A1455-A1460.

14. Jacques E. Lithium-intercalated carbon fibres. PhD Thesis, Stockholm, Engineering Sciences, Royal Institute of Technology, 2014.
15. Hagberg J, Leijonmarck S, Lindbergh G. High Precision Coulometry of Commercial PAN-Based Carbon Fibers as Electrodes in Structural Batteries. *J Electrochem Soc* 2016;163(8):A1790-A1797.
16. Jacques E, H. Kjell M, Zenkert D, Lindbergh G. The effect of lithium-intercalation on the mechanical properties of carbon fibres. *Carbon* 2014;68:725-733.
17. Jacques E, Kjell MH, Zenkert D, Lindbergh G, Behm M, Willgert M. Impact of electrochemical cycling on the tensile properties of carbon fibres for structural lithium-ion composite batteries. *Composites Sci Technol* 2012;72(7):792-798.
18. Willgert M, Kjell MH, Lindbergh G, Johansson M. New structural lithium battery electrolytes using thiol-ene chemistry. *Solid State Ion* 2013;236:22-29.
19. Ihrner N, Johansson M. Improved performance of solid polymer electrolytes for structural batteries utilizing plasticizing co-solvents. *J Appl Polym Sci* 2017;134(23).
20. Willgert M, Kjell MH, Jacques E, Behm M, Lindbergh G, Johansson M. Photoinduced free radical polymerization of thermoset lithium battery electrolytes. *Eur Polym J* 2011;47(12):2372-2378.
21. Willgert M, Leijonmarck S, Lindbergh G, Malmström E, Johansson M. Cellulose nanofibril reinforced composite electrolytes for lithium ion battery applications. *J Mater Chem A* 2014;2(33):13556-13564.
22. Carlson T. Multifunctional composite materials : Design, manufacture and experimental characterisation. PhD Thesis, Luleå University of Technology, Material Science;, 2013.
23. Asp L, Bismarck A, Lindbergh G, Leijonmarck S, Carlson T, Kjell M. Structural battery half cell, a structural battery and their manufacture. 2015(2893582).
24. Leijonmarck S, Carlson T, Lindbergh G, Asp LE, Maples H, Bismarck A. Solid polymer electrolyte-coated carbon fibres for structural and novel micro batteries. *Compos Sci Technol* 2013;89:149-157.
25. Gabrielli G, Marinaro M, Mancini M, Axmann P, Wohlfahrt-Mehrens M. A new approach for compensating the irreversible capacity loss of high-energy Si/C|LiNi_{0.5}Mn_{1.5}O₄ lithium-ion batteries. *J Power Sources* 2017;351:35-44.
26. Williard N, He W, Hendricks C, Pecht M. Lessons learned from the 787 dreamliner issue on Lithium-Ion Battery reliability. *Energies* 2013;6(9):4682-4695.

27. Doyle M, Fuller T, Newman J. Modeling of galvanostatic charge and discharge of the lithium/ polymer/insertion cell. *J Electrochem Soc* 1993;140(6):1526-1533.
28. Newman J, Tiedemann W. Porous-electrode theory with battery applications. *AIChE J* 1975;21(1):25-41.
29. Ramadesigan V, Northrop PWC, De S, Santhanagopalan S, Braatz RD, Subramanian VR. Modeling and simulation of lithium-ion batteries from a systems engineering perspective. *J Electrochem Soc* 2012;159(3):R31-R45.
30. COMSOL Multiphysics® v. 5.2. www.comsol.com. COMSOL AB, Stockholm, Sweden.
31. Nyman A, Behm M, Lindbergh G. A theoretical and experimental study of the mass transport in gel electrolytes II. Experimental characterization of LiPF₆-EC-PC-P(VdF-HFP). *J Electrochem Soc* 2011;158(6):A636-A643.
32. Hamann CH, Hamnett A, Vielstich W. *Electrochemistry*. Weinheim: Wiley-VCH, 2007.
33. Pupurs A, Varna J. Modeling mechanical stress and exfoliation damage in carbon fiber electrodes subjected to cyclic intercalation/deintercalation of lithium ions. *Compos B Eng* 2013.
34. Hashin Z. Analysis of Composite Materials- A Survey. *J Appl Mech Trans ASME* 1983;50(3):481-505.
35. Hashin Z, Rosen B.W. The elastic moduli of fiber-reinforced materials. 1964;32(2):223-232.
36. Christensen RM, Lo KH. Solutions for effective shear properties in three phase sphere and cylinder models. *J Mech Phys Solids* 1979;27(4):315-330.
37. Marklund E, Varna J, Neagu RC, Gamstedt EK. Stiffness of aligned wood fiber composites: Effect of microstructure and phase properties. *J Compos Mater* 2008;42(22):2377-2405.
38. Siegel JB, Stefanopoulou AG, Hagans P, Ding Y, Gorsich D. Expansion of Lithium Ion Pouch Cell Batteries: Observations from Neutron Imaging. *J Electrochem Soc* 2013;160(8):A1031-A1038.
39. Wang X, Sone Y, Segami G, Naito H, Yamada C, Kibe K. Understanding Volume Change in Lithium-Ion Cells during Charging and Discharging Using In Situ Measurements. *J Electrochem Soc* 2007;154(1):A14-A21.
40. Zhang N, Tang H. Dissecting anode swelling in commercial lithium-ion batteries. *J Power Sources* 2012;218:52-55.
41. ANSYS INC. ANSYS ® Academic Research Release 15.0. 2011.

42. Krueger R. Virtual crack closure technique: History, approach, and applications. *Appl Mech Rev* 2004;57(1-6):109-143.
43. Hull D, Clyne TW. *An introduction to composite materials*. Cambridge: Cambridge Univ. Press, 1996.
44. Bismarck A, Lee AF, Saraç AS, Schulz E, Wilson K. Electrocoating of carbon fibres: A route for interface control in carbon fibre reinforced poly methylmethacrylate? *Compos Sci Technol* 2005;65(10):1564-1573.
45. Hagberg J, Maples HA, Alvim KSP, Xu J, Johannisson W, Bismarck A, Zenkert D, Lindbergh G. Lithium iron phosphate coated carbon fiber electrodes for structural lithium ion batteries. *Compos Sci Technol* 2018;162:235-243.
46. Sela N, Ishai O. Interlaminar fracture toughness and toughening of laminated composite materials: a review. *Composites* 1989;20(5):423-435.
47. Pitkethly MJ, Favre JP, Gaur U, Jakubowski J, Mudrich SF, Caldwell DL, Drzal LT, Nardin M, Wagner HD, Di Landro L, Hampe A, Armistead JP, Desaeger M, Verpoest I. A round-robin programme on interfacial test methods. *Composites Sci Technol* 1993;48(1-4):205-214.
48. An Q, Rider AN, Thostenson ET. Electrophoretic deposition of carbon nanotubes onto carbon-fiber fabric for production of carbon/epoxy composites with improved mechanical properties. *Carbon* 2012;50(11):4130-4143.
49. Bachinger A, Rössler J, Asp LE. Electrocoating of carbon fibres at ambient conditions. *Compos B Eng* 2016;91(Supplement C):94-102.
50. Fredi G, Jeschke S, Boulaoued A, Wallenstein J, Rashidi M, Liu F, Harnden R, Zenkert D, Hagberg J, Lindbergh G, Johansson P, Stievano L, Asp LE. Graphitic microstructure and performance of carbon fibre Li-ion structural battery electrodes. *Multifunctional Materials* 2018;1(1):015003.
51. Jacques E, Hellqvist Kjell M, Zenkert D, Lindbergh G, Behm M. Expansion of carbon fibres induced by lithium intercalation for structural electrode applications. *Carbon* 2013;59:246-254.
52. Nyman A. *An Experimental and Theoretical Study of the Mass Transport in Lithium-Ion Battery Electrolytes*. PhD Thesis, Stockholm, KTH Applied Electrochemistry, 2011.
53. Johannisson W, Ihrner N, Zenkert D, Johansson M, Carlstedt D, Asp LE, Sieland F. Multifunctional performance of a carbon fiber UD lamina electrode for structural batteries. *Compos Sci Technol* 2018;168:81-87.
54. Greenwood R, Luckham PF, Gregory T. The Effect of Diameter Ratio and Volume Ratio on the Viscosity of Bimodal Suspensions of Polymer Latexes. *J Colloid Interface Sci* 1997;191(1):11-21.

55. Kwon S, Adachi T, Araki W, Yamaji A. Thermo-viscoelastic properties of silica particulate-reinforced epoxy composites: Considered in terms of the particle packing model. *Acta Mater* 2006;54(12):3369-3374.
56. Drozdov AD. Modeling viscoelastic response of particulate polymeric composites with high volume fractions of fillers. *Math Comput Model* 1999;29(4):11-25.
57. van Hartingsveldt EAA, van Aartsen JJ. Strain-rate dependence of interfacial adhesion in particle-reinforced polymers. *Polymer* 1991;32(8):1482-1487.
58. Kjell MH, Zavalis TG, Behm M, Lindbergh G. Electrochemical characterization of lithium intercalation processes of PAN-based carbon fibers in a microelectrode system. *J Electrochem Soc* 2013;160(9):A1473-A1481.
59. Jacques E, Kjell MH, Zenkert D, Lindbergh G, Behm M. Effect of lithium-ion intercalation on the tensile properties of carbon fibres for energy storage composites. *Eccm-15, Venice, Italy*, 2012.
60. Ekström H, Lindbergh G. A Model for Predicting Capacity Fade due to SEI Formation in a Commercial Graphite/LiFePO₄ Cell. *Journal of The Electrochemical Society* 2015;162(6):A1003-A1007.

Paper I

Multiphysics modeling of mechanical and electrochemical phenomena in structural composites for energy storage: Single carbon fiber micro-battery

Journal of Reinforced Plastics and Composites
2018, Vol. 37(10) 701–715
© The Author(s) 2018
Reprints and permissions:
sagepub.co.uk/journalsPermissions.nav
DOI: 10.1177/0731684418760207
journals.sagepub.com/home/jrp
SAGE

Johanna Xu¹ , Göran Lindbergh²  and Janis Varna¹

Abstract

This paper presents a framework for multiphysics modeling of a novel type of multifunctional composite material, structured on microscale, with ability to function as battery cell in addition to carry mechanical load. The micro-battery consists of a single carbon fiber surrounded by very thin solid electrolyte coating and embedded in a matrix which is a porous material containing active particles able to intercalate lithium. During battery operation (discharging and charging) the structural battery constituents undergo volume changes, caused by lithium-ion movement. The presented mathematical model is solved numerically using COMSOL software and results are used to analyze the physical phenomena occurring in the structural battery material. Parametric analysis is performed to reveal the significance of geometrical parameters like fiber volume fraction in the battery and the porosity content in the matrix on the multifunctional performance of the composite unit including its swelling/shrinking during charging/discharging.

Keywords

Carbon fiber, lithium-ion battery, multiphysics modeling

Introduction

Concept of structural battery

In the last five decades of development of man-made fiber composites the emphasis, motivated by an overall goal of material and energy saving, has been on developing lightweight materials with excellent specific strength and stiffness. In recent years a new branch with the same overall goals has emerged with the focus shifted from solely optimizing composite materials' structural performance to also exploiting its multifunctionality. Multifunctionality, i.e. when at least two functions are delivered by the same material simultaneously, is regarded as a major weight reduction solution. The multifunctional concept for composite materials, considering structural and electrical energy storage functionalities, can be implemented in different ways, e.g. by multifunctional structures where different subsystems are merged into one, such as thin film batteries being embedded within composite laminates.¹ Another approach is to formulate multifunctional materials, where the material simultaneously carries mechanical loads and, for

example, stores electrical energy. A polymer composite material with intrinsic high mechanical and electrochemical properties is referred to as structural power composite. Such devices are desired for their potential to both reduce weight and provide the energy needs for future electric vehicles. The state-of-the-art research on various concepts of structural power composites has been reviewed by Asp and Greenhalgh.²

Research on structural power composites so far has focused on structural supercapacitors and structural batteries, which both store and release electrical energy, but their working principle differs. Batteries store energy electrochemically: chemical reactions

¹Department of Engineering Sciences and Mathematics, Luleå University of Technology, Luleå, Sweden

²School of Chemical Science and Engineering, KTH Royal Institute of Technology, Stockholm, Sweden

Corresponding author:

Johanna Xu, Department of Engineering Sciences and Mathematics, Luleå University of Technology, Luleå 97189, Sweden.
Email: Johanna.Xu@ltu.se

release electrons that can be extracted into a circuit. In a supercapacitor, no chemical reactions are involved; energy is stored electrostatically on the surface of the material. The main disadvantage of supercapacitors is low energy density, meaning the amount of energy stored per unit weight is limited. For this reason, the development of structural batteries appears to be more promising from a future vehicle application point of view.

A typical lithium-ion (Li-ion, Li^+) battery cell consists of a negative electrode connected to the negative terminal of the cell, a positive electrode connected to the positive terminal of the cell, and a separator soaked with liquid electrolyte between the two electrodes preventing short circuiting. Usually the electrodes consist of nano-to-micrometer sized electrochemically active electrode material particles, electrochemical reactions taking part on their surface, mixed together with electronic conductive additives and binder material. Examples of active electrode material are graphite (powder) in the negative electrode and lithiated metal phosphates (e.g. LiFePO_4) in the positive electrode, both serving as host materials allowing for lithium-ion extraction and insertion as the battery is charged and discharged. The insertion process of lithium into active materials is called intercalation.

During the discharge of the lithium-ion battery, Li diffuses to the surface of graphite particles in the negative electrode where it undergoes electrochemical reaction, and then the ions travel through the electrolyte solution via diffusion and ionic conduction to the positive electrode where they react and diffuse toward the inner regions of the LiFePO_4 particles. During charging, the process is reversed.

To introduce an energy storage function in the structural composites, each constituent material must undertake additional roles to allow for the above-mentioned mechanisms.

In this paper we analyze a micro-battery containing one single carbon fiber as negative microelectrode. It is coated with a solid battery electrolyte (SBE) and embedded in a solid positive electrode material, which also acts as matrix.

Previous work investigating the electrochemical performance of different carbon fibers³⁻⁵ has shown that PAN-based carbon fibers are suited as electrode material since they show ability to intercalate Li ions. Hagberg et al.⁵ found capacities and columbic efficiencies (the fraction of the prior charge capacity that is available during the following discharge cycle) of PAN-based carbon fibers matching commercial state-of-the-art graphitic electrodes. Jacques et al.⁶ studied the effect of intercalation on fiber tensile properties and reported that the fiber stiffness is unaffected by repeated lithium intercalation/deintercalation, but a drop in

strength of approximately 10% was measured. A 1% free axial expansion of the fiber was measured at fully charged state, and a corresponding radial expansion was estimated to be around 10%.

The main task of the matrix in a structural composite material is to ensure load transfer to fibers; in a structural battery application, the role should be extended to also serve as an electrode material. This can be achieved by adding electrochemically active material and electrically conductive material to the polymer in the matrix.

With the carbon fibers as one electrode (the negative) and the matrix material as the other electrode (the positive), it is evident that these two materials cannot be in direct contact, since this will cause short circuiting. Therefore, an isolating separator material between the electrodes is needed, together with an electrolyte to allow for ion transportation between the electrodes.

The electrolytes' role in a conventional battery is to enable ion transport between the two electrodes, through diffusion and migration. The ion conductivity of the electrolyte is one of the most important properties as it governs the rate at which the lithium ions move, and hence the resulting current. Thus, it can be understood that high ionic conductivity is desirable for an electrolyte in a battery, while a structural battery additionally requires good mechanical properties of all constituents. Although the highest ionic conductivities are found in liquid electrolytes, these cannot be used in structural batteries, due to the lack of mechanical performance. Instead, SBEs are required⁷⁻⁹ to accommodate for load transfer, ion conduction, and preventing short circuiting, they have lower ion conductivity but the distance for transport in the micro-battery is much smaller than in conventional battery.

Modeling challenges

Numerous mathematical models of lithium-ion batteries are available in literature. Depending on the modeling purpose the formulations differ significantly, ranging from simple equivalent electric circuit model to so-called physics-based models. For example, battery management systems in electric vehicles, the computationally inexpensive equivalent electric circuit model is suitable,¹⁰ because obtaining rapid descriptions for the battery external characteristics is the main objective. However, to study transient behavior and electrochemical processes of the battery cell, physics-based models are needed and the phenomena are described by differential equations.

A mathematical model to simulate the processes in lithium-ion battery cells, consisting of positive and negative porous electrodes, a separator, and current collectors, was first introduced by Newman et al.¹¹⁻¹³

in the early 1990s. This model based on the principles of transport phenomena, electrochemistry, and thermodynamics is represented by coupled nonlinear partial differential equations on different scales. This model is by far the most prevalent among battery researchers, as it solves for the (i) Li^+ concentration in electrolyte, (ii) electrolyte potential, (iii) solid-state potential, (iv) Li concentration within the porous electrodes, and (v) the electrolyte concentration and electrolyte potential within the separator. These models have since then been refined to better predict the cell voltage and other performance metrics at different operating conditions, by including other phenomena such as heat generation and aging mechanisms.¹⁴

In the field of electrochemistry, the main interest to investigate mechanical stresses and strains caused by dimensional changes during intercalation/deintercalation of Li into and from active materials originates from the necessity to predict loss of capacity and a decline in cycling performance due to crack formation at the active material surface. Available approaches use a diffusion model coupled with continuum mechanics model. Often a one-way coupling is assumed where the diffusion is not affected by stress, since elastic deformation is a much faster process in comparison to diffusion in solids. Most of the work has been focusing on an isolated active particle, meaning that various assumptions were made in order to disregard the surrounding phases.

Cheng and Verbrugge^{15,16} provided models of diffusion-induced stress in single spherical nanoparticles under different types of operation, with the objective to study the particle size and surface effects on the stress in the nanoparticles. A criterion for crack propagation within a spherical insertion electrode was established.¹⁷

Botte¹⁸ used a single particle model to analyze volume changes due to lithium intercalation in a single carbon fiber, evaluating the cyclic voltammetry performance, aiming at extending the results from the microelectrode to modeling the performance of full-size electrodes. The internal stresses in the carbon fiber induced by diffusion and intercalation of lithium were also investigated by Pupurs and Varna,¹⁹ where the propagation of possible radial and arc cracks formation was studied using well-known fracture mechanics techniques. The focus was on internal stresses in the fiber due to concentration gradient and not on the mechanical constraint of surrounding materials.

In addition to the volume changes in the fiber,²⁰ also swelling in the active material particles of the positive electrode has been measured to be approximately 7%.²¹ The constrain to volume changes during battery operation can result in microdamage in the material,

degrading both electrical and mechanical performance of the structural battery composite.

In this work a multiscale and multiphysics electrochemical-mechanical coupled model is developed and used for analyzing volume changes in the structural battery constituents during electrochemical cycling. A single carbon fiber micro-battery cell is analyzed. The battery cell consists of a carbon fiber negative microelectrode, with individual carbon fiber coated by a SBE material, surrounded by a solid positive electrode material, made from a LiFePO_4 -doped SBE matrix material.

The mechanical stresses in the battery during electrochemical cycling are governed by swelling and shrinking of electrodes resulting from the lithium-ion transport. A physics-based model describing the electrochemical behavior of the full cell is presented, employing a one-way coupling to the elastic deformation. The mechanical constraint of surrounding materials to the fiber that was left out in previous study¹⁹ is taken into account. It is important to take these constraints into consideration, because they represent a significant part of the battery structure.

The objective of this paper is to provide a mathematical framework for describing physical phenomena taking place in this novel microstructured composite with ability to store energy and to perform mechanically. The developed model is used to demonstrate the dependence of polarization (i.e. the voltage drop) and capacity (the amount of charge the cell can deliver) on different boundary conditions and battery designs.

Theory

The working principle of a micro-battery was presented in the "Introduction" section. In brief, electrons flow internally through the electrodes and externally in an outer circuit. Li^+ are transported from one electrode to the other via the electrolyte through diffusion and migration, to provide reactants to the interfaces with the active materials where intercalation reactions occur, where the ions are reduced and neutral Li diffuses into the active material. The processes taking place during a normal battery operation are listed in Table 1, and each of these processes requires its own modeling, on different length scales.

The chemical reactions for a LiFePO_4 /carbon fiber lithium-ion cell giving rise to these processes are given below.

At the surface of the active material in the positive electrode

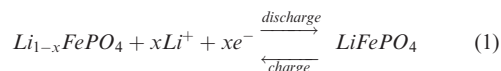
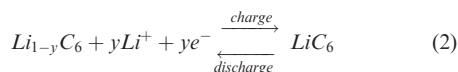


Table 1. Processes taking place in a battery during operation and its models.

Processes	Domain	Model
Intercalation reactions	Surface of the active materials	Butler–Volmer equation
Electronic conduction	Electronic conductive phase of the electrodes	Ohm's law
Li diffusion in active material	Electrochemically active material	Mass balance equation (Fick's second law)
Migration	Electrolyte	Electroneutrality
Li ⁺ ionic diffusion	Electrolyte	Mass balance equation

and at the carbon fiber surface



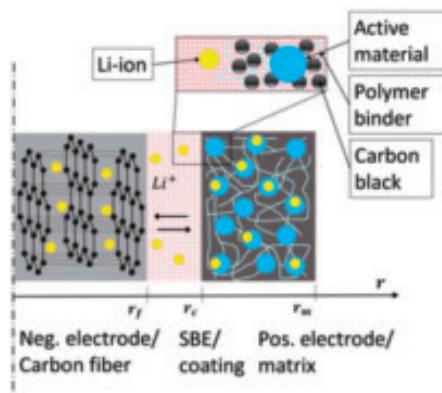
The difference between the voltage under equilibrium and that under operation (i.e. with a current flow) is termed polarization. The polarization originates from three basic subprocesses, including (i) activation overpotential, associated with the activation of the electrochemical reactions; (ii) diffusion polarization, due to the concentration gradients built up in the electrolyte and in the active material phase; (iii) ohmic potential drop, due to insufficient ionic conductivity in the electrolyte and electronic conductivity in the solid phase.

Polarization effects have significant impact on the battery efficiency and how the battery can be charged and discharged. The contributions from a specific subprocess to the total polarization can be quantified using the method demonstrated by Nyman et al.²² However, the focus of this study is on differences in the polarization depending on different designs, and the consequences in terms of swelling, rather than the source of polarization.

Materials and geometry

Previous reported work on structural batteries²³ considered a laminated design, where the electrode and the separator materials in the form of sheets were stacked and then laminated with current collectors. Although proof of concept was confirmed, the battery performed poorly, mainly due to the low ionic conductivity of the SBE. In a laminated structural battery the distance between the electrodes, which is the distance for lithium-ion transport, is typically in the order of 10–100 μm . A method of coating single carbon fiber with a polymer electrolyte in a continuous process by electropolymerization was introduced by Leijonmarck et al.,²⁴ by which the lithium transport distance can be reduced to less than 500 nm, allowing for new structural battery designs.

The conceptualized cylindrical axisymmetric microbattery considered in this paper consists of an individual negative electrode, carbon fiber coated by a gel

**Figure 1.** Schematic of the cell constituents. (SBE: solid battery electrolyte.)**Table 2.** Battery cell constituents for balanced electrodes.

Constituent	Thickness (μm)
Carbon fiber, r_f	2.5
SBE layer on carbon fiber, $r_c - r_f$	0.1
Positive electrode matrix, $r_m - r_c$	1.7

electrolyte (lithium salt and solvent dissolved in a polymer) surrounded by a solid positive electrode material, which partially consists of the electrochemically active material LiFePO_4 (Figure 1).

The radius of the battery system r_m is 4.3 μm , with a fiber content of $V_f = 0.34$, detailed dimensions of constituents are shown in Table 2, which will be called the reference case where the electrodes are balanced for the ability to intercalate ions.

Mathematical modeling

Physics-based lithium-ion battery model

The equations presented in the following subsections are used to describe the spatial and time-dependent variation in the potential as well as in the lithium-ion

concentration in the solid and electrolyte phases. The equations associated with the electrolyte and the potentials are solved for the axisymmetric model in Figure 1 to find the time- and r -dependences. The lithium concentration within the electrochemically active material is solved for the spatial variation along the r -direction of the battery as well as R -direction of the active material particles.

To carry out this type of modeling many input parameters have been collected from various experiments reported in literature (see Tables 3 and 4). Boundary and interface conditions are summarized in Tables 5 and 6.

Fiber region. The lithium transportation in the active material of the negative electrode, i.e. the carbon fiber, is described by Fick's law of diffusion in the cylindrical coordinate system

$$\frac{\partial c_f(r,t)}{\partial t} = \frac{1}{r} \frac{\partial}{\partial r} \cdot \left(D_f \frac{\partial c_f}{\partial r} r \right) \quad (21)$$

where c is the Li concentration with subscript f denoting the fiber phase, D is the c_f -dependent diffusion coefficient, and t is the time.

There is no flux at the center of the fiber, equation (3) in Table 5. On the fiber surface $r = r_f$, equation (4), the flux is determined by the reaction rate of Li ions from the electrochemical reaction occurring on the

interface at fiber/coating interface, described by equation (38) in "Reaction kinetics" section.

Coating region. The modeling of mass transport involves describing the interactions between the species in the electrolyte. The equations presented in this section are

Table 5. Boundary conditions for mass balance equations in electrode active material and SBE phase.

Dependent variable	Boundary	Expression	
c_f	$r = 0$	$-D_f \frac{\partial c_f}{\partial r} = 0$	(3)
	$r = r_f$	$-D_f \frac{\partial c_f}{\partial r} = J_f(t)$	(4)
c_a	$R = 0$	$-D \frac{\partial c_a}{\partial R} = 0$	(5)
	$R = R_p$	$-D_a \frac{\partial c_a}{\partial R} = J_m(r,t)$	(6)
$c_{salt,c}$	$r = r_f$	$\frac{\partial c_{salt,c}}{\partial r} = \frac{D_{LL}(1-t_+) + D_{SS}t_+}{D_{SS}D_{LL} - D_{LS}D_{SL}} \frac{J_f}{F}$	(7)
	$r = r_c$	$c_{salt,c} = c_{salt,m}$	(8)
$c_{salt,m}$	$r = r_c$	$-D_{SS} \frac{\partial c_{salt,c}}{\partial r} = -D_{SS,eff} \frac{\partial c_{salt,m}}{\partial r}$	(9)
	$r = r_m$	$\frac{\partial c_{salt,m}}{\partial r} = 0$	(10)
$c_{solv,c}$	$r = r_f$	$\frac{\partial c_{solv,c}}{\partial r} = \frac{D_{SS}(1-t_+) + D_{SS}t_+}{D_{SS}D_{LL} - D_{LS}D_{SL}} \frac{J_f}{F}$	(11)
	$r = r_c$	$c_{solv,c} = c_{solv,m}$	(12)
$c_{solv,m}$	$r = r_c$	$-D_{LL} \frac{\partial c_{solv,c}}{\partial r} = -D_{LL,eff} \frac{\partial c_{solv,m}}{\partial r}$	(13)
	$r = r_m$	$\frac{\partial c_{solv,m}}{\partial r} = 0$	(14)

Table 3. Positive electrode properties and composition used in the reference case.

Property	Symbol	Value	Unit
Solid phase Li diffusivity	D_a	$3.42 \cdot 10^{-22}$	m^2/s
Particle radius	R_p	$2.49 \cdot 10^{-7}$	m
Electronic conductivity in conductive additives	σ_{cs}^+	91	S/m
Volume fraction conductive additive	ε_{cs}^+	$9.3 \cdot 10^{-2}$	—
Volume fraction active material	ε_s^+	$5.33 \cdot 10^{-1}$	—
Volume fraction electrolyte phase	ε_L^+	$2.7 \cdot 10^{-1}$	—
Conductive phase Bruggeman's constant	β_{cs}^+	1.5	—
Electrolyte phase Bruggeman's constant	β_L^+	2.92	—

Table 4. State-of-charge-dependent carbon fiber parameters.⁴

Parameter	SOC %					
	5	20	40	60	80	100
D_f (m^2/s)	$1.41 \cdot 10^{-14}$	$3 \cdot 10^{-13}$	$6.87 \cdot 10^{-13}$	$6.69 \cdot 10^{-13}$	$1.89 \cdot 10^{-12}$	$3.6 \cdot 10^{-12}$
$i_{0,f}$ ($\frac{A}{m^2}$)	0.96	2.67	3.87	5.03	5.31	5.90

SOC: state of charge.

Table 6. Boundary conditions for charge balance equations in electronically and ionically conductive phases.

Dependent variable	Boundary	Expression
$\Phi_{e,c}$	$r = r_f$	$\frac{\partial \Phi_{e,c}}{\partial r} = \frac{I_c}{\kappa} + \eta_{salt} \frac{\partial c_{salt,c}}{\partial r} + \eta_{solv} \frac{\partial c_{solv,c}}{\partial r}$ (15)
	$r = r_c$	$\Phi_{e,c} = \Phi_{e,m}$ (16)
$\Phi_{e,m}$	$r = r_c$	$-\kappa \frac{\partial \Phi_{e,c}}{\partial r} = -\kappa_{eff} \frac{\partial \Phi_{e,m}}{\partial r}$ (17)
	$r = r_m$	$-\kappa_{eff} \frac{\partial \Phi_{e,m}}{\partial r} = 0$ (18)
$\Phi_{s,m}$	$r = r_c$	$-\sigma_{eff,m} \frac{\partial \Phi_{s,m}}{\partial r} = 0$ (19)
	$r = r_m$	$-\sigma_{eff,m} \frac{\partial \Phi_{s,m}}{\partial r} = I_{app}$ (20)

derived for a gel electrolyte where a lithium hexafluorophosphate (LiPF₆) salt is dissolved in an ethylene carbonate-propylene carbonate mixture and a poly(vinylidene fluoride-hexafluoropropylene) copolymer, the derivations can be found in Nyman.²⁵ A set of nine transport properties are required to describe the mass transport in the gel electrolyte. These include one ionic conductivity κ ; two coefficients describing the relation between the potential gradient and the concentration gradients, η_{salt} and η_{solv} ; four apparent diffusion coefficients, D_{SS} , D_{SL} , D_{LS} , and D_{LL} , based on Maxwell-Stefan diffusivities; two transport numbers, t_+ and t_L , describing the fraction of the total current carried in the electrolyte by the Li⁺ and the solvent, respectively. These nine transport properties can be obtained through a series of characterization experiments as described by Nyman et al.²⁶ and have proven to be solvent concentration dependent.

The governing equations describing the concentration distributions (salt and solvent) in the gel electrolyte coating are

$$r \frac{\partial c_{salt,c}}{\partial t} = \frac{\partial}{\partial r} \left[r \left(D_{SS} \frac{\partial c_{salt,c}}{\partial r} + D_{SL} \frac{\partial c_{solv,c}}{\partial r} + (1 - t_+) \frac{i_{e,c}}{F} \right) \right] \quad (22)$$

and

$$r \frac{\partial c_{solv,c}}{\partial t} = \frac{\partial}{\partial r} \left[r \left(D_{LS} \frac{\partial c_{salt,c}}{\partial r} + D_{LL} \frac{\partial c_{solv,c}}{\partial r} + t_L \frac{i_{e,c}}{F} \right) \right] \quad (23)$$

where $c_{salt,c}$ and $c_{solv,c}$ are the electrolyte salt and solvent concentrations in the coating.

The material balance equations (22) and (23) describe both diffusion and migration mechanisms by which ions are transported. The current density in the electrolyte coating, $i_{e,c}$, seen in the last term of the right-hand side of equations (22) and (23) is calculated from

$$i_{e,c} = \kappa \left(-\frac{\partial \Phi_{e,c}}{\partial r} + \eta_{salt,c} \frac{\partial c_{salt,c}}{\partial r} + \eta_{solv,c} \frac{\partial c_{solv,c}}{\partial r} \right) \quad (24)$$

where κ is the ionic conductivity of the electrolyte. The variation of the potential across the coating separator, $\Phi_{e,c}$, is described by equation (25). The potential increases with higher current densities and higher concentration gradients

$$\frac{\partial}{\partial r} \left(r \frac{\partial \Phi_{e,c}}{\partial r} \right) = \frac{\partial}{\partial r} \left(\eta_{salt,c} \frac{\partial c_{salt,c}}{\partial r} r \right) + \frac{\partial}{\partial r} \left(\eta_{solv,c} \frac{\partial c_{solv,c}}{\partial r} r \right) \quad (25)$$

Coefficients $\eta_{salt,c}$ and $\eta_{solv,c}$, also seen in equation (24) describe the relation between potential and concentration gradients, the empirical fitting expressions are²⁶

$$\eta_{salt,c} = 5.326 \cdot 10^{-5} + 2.470 \cdot 10^{-2} \frac{1}{c_{salt,c}} \quad (26)$$

$$\eta_{solv,c} = -5.394 \cdot 10^{-6} - 3.616 \cdot 10^{-2} \frac{1}{c_{solv,c}} \quad (27)$$

The boundary conditions for solving equations (22), (23), and (25) are given in Table 5 (equations (7), (8), (11), and (12)) and (equations (15) and (16)).

Matrix region. The matrix material is a porous electrode, composed by a mixture of solids that include electrolyte, electrochemically active material, electronic conductors, and polymer binder material. Mass transport in the electrolyte phase of the electrode and reaction rates in the electrode active material depend on the physical structure of the electrode.

Li concentration in the active material phase, c_a , in the positive electrode, which is assumed to be spherical particles, can be described by Fick's second law in spherical coordinates

$$\frac{\partial c_a(R, r, t)}{\partial t} R^2 = \frac{\partial}{\partial R} \left(R^2 D_a \frac{\partial c_a}{\partial R} \right) \quad (28)$$

where R is the radial coordinate and D_0 is the constant diffusion coefficient for Li in LiFePO_4 particle.

There is no flux at the center of the spherical particle (equation (5)). On the surface of the particle, the flux, equation (42), is determined by the reaction rate of Li ions from the electrochemical reaction occurring on the interface at the active material/electrolyte interface (equation (6)).

The porous electrode is described with a macro-homogenous model, where the porous structure is disregarded. Instead the porous electrode is regarded as a superposition of two continuous phases, electrode and electrolyte, being present at every point in the volume of the electrode.²⁷ The transport properties, such as diffusion coefficients and conductivities, are then given averaged values that account for the effects of porosity, ε_e^+ (the ratio of electrolyte volume to total volume) and tortuosity ("labyrinth" effect) through effective properties with subscript *eff*

$$P_{eff} = P \cdot \varepsilon_e^{+\beta_e^+} \quad P = D_{SS}, D_{SL}, D_{LS}, D_{LL}, \kappa \quad (29)$$

where β_e^+ is the electrolyte phase Bruggeman coefficient, constant for all properties P , the power function describes the accessibility for the species transport in the electrode.

The material balance in the electrolyte phase of the porous electrode is then calculated similarly to equations (22) and (23)

$$\varepsilon_e^+ r \frac{\partial c_{salt,m}}{\partial t} = \frac{\partial}{\partial r} \left[r \left(D_{SS,eff} \frac{\partial c_{salt,m}}{\partial r} + D_{SL,eff} \frac{\partial c_{solv,m}}{\partial r} + (1 - t_+) \frac{i_{e,m}}{F} \right) \right] \quad (30)$$

and for solvent

$$\varepsilon_e^+ r \frac{\partial c_{solv,m}}{\partial t} = \frac{\partial}{\partial r} \left[r \left(D_{LS,eff} \frac{\partial c_{salt,m}}{\partial r} + D_{LL,eff} \frac{\partial c_{solv,m}}{\partial r} + t_L \frac{i_{e,m}}{F} \right) \right] \quad (31)$$

At the interfaces between the positive electrode/coating the concentrations of the electrolyte and its flux are continuous (equations (8) and (12)). Also, at the battery cell outer surface in the radial direction, there is no mass flux (equation (10)).

Similar to the electrolyte current density in the coating (24), the electrolyte phase current in the matrix is given by

$$i_{e,m} = \kappa_{eff} \left(-\frac{\partial \Phi_{e,m}}{\partial r} + \eta_{salt,m} \frac{\partial c_{salt,m}}{\partial r} + \eta_{solv,m} \frac{\partial c_{solv,m}}{\partial r} \right) \quad (32)$$

The potential $\Phi_{e,m}$ is given by

$$\begin{aligned} \frac{\partial}{\partial r} \left(r \frac{\partial \Phi_{e,m}}{\partial r} \right) &= \frac{\partial}{\partial r} \left(\eta_{salt,m} \frac{\partial c_{salt,m}}{\partial r} r \right) \\ &+ \frac{\partial}{\partial r} \left(\eta_{solv,m} \frac{\partial c_{solv,m}}{\partial r} r \right) - \frac{A \cdot j_{loc,m} r}{\kappa_{eff}} \end{aligned} \quad (33)$$

Coefficients $\eta_{salt,m}$ and $\eta_{solv,m}$ in equations (32) and (33) are given similarly to equations (26) and (27)²⁶

$$\eta_{salt,m} = 5.326 \cdot 10^{-5} + 2.470 \cdot 10^{-2} \frac{1}{c_{salt,m}} \quad (34)$$

$$\eta_{solv,m} = -5.394 \cdot 10^{-6} - 3.616 \cdot 10^{-2} \frac{1}{c_{solv,m}} \quad (35)$$

The solid phase electrical potential $\phi_{s,m}$ is calculated by Ohm's law, given by

$$\sigma_{eff,m} \frac{1}{r} \frac{\partial}{\partial r} \left(\frac{\partial \phi_{s,m}}{\partial r} r \right) = A \cdot j_{loc,m} \quad (36)$$

Where σ_{eff} is the effective conductivity of the matrix corrected for porosity using power function $\sigma_{eff,m} = \sigma_{eS}^+ \beta_{eS}^+$, where ε_{eS}^+ and β_{eS}^+ are volume fraction of the electronic conductor and solid phase Bruggeman coefficient, $j_{loc,m}$ is the local current density calculated from the reaction kinetics (see next section). A is the surface area of the active material per total electrode volume calculated by

$$A = \frac{3}{R_p} (\varepsilon_S^+) \quad (37)$$

where R_p is the radius of the active material particle, and ε_S^+ is the volume fraction active material in the electrode. Properties of the porous matrix positive electrode are shown in Table 3.

The net electron flux at the matrix/coating (electrode/separator) interface is zero (equation (19)). At the outer surface of the matrix electrode, the boundary condition for the charge flux is the current density applied to the cell (equation (20)).

Reaction kinetics. The reaction is assumed to take place only at the surface of the active materials. The process kinetics is described by the Butler–Volmer equation stating the relationship between the current density, concentration, and overpotential

$$J_f|_{r=r_f} = i_{0,f} \left[\exp \left(\frac{\alpha_a F \eta_f}{R_g T} \right) - \exp \left(-\frac{\alpha_c F \eta_f}{R_g T} \right) \right] \quad (38)$$

where α_a and α_c are the transfer coefficients for the anodic and cathodic reaction in the electrode, R_g is the universal gas constant, F is Faraday's constant, T is the temperature, and η_f is the overpotential at the negative electrode, given by

$$\eta_f|_{r=r_f} = \Phi_{s,f} - \Phi_{e,c} - E_{OCP,f} \quad (39)$$

$E_{OCP,f}$ is the open-circuit potential (OCP) for a single fiber, obtained from curve-fitting experimental data from electrochemical cycling.⁴ The exchange current density of the fiber, $i_{0,f}$, is a measure of the rate of electron transfer at equilibrium,²⁸ obtained from electrochemical impedance spectroscopy⁴ and shown to be strongly Li concentration dependent (Table 4). The Li concentration is expressed through state of charge (SOC), defined as

$$SOC = \frac{c_f}{c_{f,max}} \quad (40)$$

For the positive porous electrode, electrochemical processes taking place on the surface of the active material particles need to account for the presence of other phases within the electrode and also variations in shape. The flux of Li^+ to and from the surface of the active material is defined per total electrode volume in the model, calculated from the product of the flux density, J_m and the interfacial (surface) area per total electrode volume.

The active material and electrolyte phases are coupled by the flux of Li^+ to or from the surface of the active material phase, since the charge entering the electrolyte must leave the active material and vice versa. The current density in the electrolyte ($i_{e,m}$) is coupled to the local current per active material area and the flux of ions over the interface between the active particle surface and the electrolyte (J_m) by

$$\frac{\partial i_{e,m}}{\partial r} = A \cdot j_{loc,m} = A \cdot F \cdot J_m \quad (41)$$

The Butler–Volmer equation remains locally valid at each point of the active electrode material–electrolyte interface according to

$$\begin{aligned} j_{loc,m}(r, t) = & c_{a,avg} k_{a,0} \exp\left[\frac{\alpha_a F}{R_g T} \cdot (\phi_{s,m} - \phi_{e,m} - E_{ref})\right] \\ & - c_{salt,m} \cdot (c_{a,max} - c_{a,avg}) \cdot k_{c,0} \\ & \times \exp\left[-\frac{\alpha_c F}{R_g T} \cdot (\phi_{s,m} - \phi_{e,m} - E_{ref})\right] \end{aligned} \quad (42)$$

$c_{a,avg}$ and $c_{a,max}$ are the average and the maximum concentration of lithium in the active material of the

positive electrode, respectively. α_a and α_c , which is also included in equation (38), are so-called dimensionless charge transfer coefficients, here assumed to be 0.5. Reaction rate constants, $k_{a,0}$ and $k_{c,0}$, are the anodic and cathodic reactions, respectively, and are coupled by the following expression

$$k_{c,0} = k_{a,0} \cdot \frac{c_{a,avg}}{c_{salt,m} \cdot (c_{a,max} - c_{a,avg})} \exp\left[\frac{F}{R_g T} \cdot (E_{OCP,a} - E_{ref})\right] \quad (43)$$

where $E_{OCP,a}$ is the OCP of the active material, which is concentration dependent and measured elsewhere.²⁹ E_{ref} (also seen in equation (42)) is an arbitrary value that is introduced to keep the anodic and cathodic reaction rate constants within a comparable order of magnitude.²²

Simulation procedure

The mathematical model described in previous section is a multiscale model. The equations presented are used to describe the spatial and time-dependent variation in lithium concentration as well as the potential in the solid (active material) and electrolyte phases. The model is divided into three domains: fiber negative electrode, coating separator and matrix electrode, denoted Ω_f , Ω_c , and Ω_m , respectively (Figure 2(a)).

The simulation consists of two coupled 1D models (Figure 2). The first model represents the macroscopic level, consisting of the three domains Ω_f , Ω_c , and Ω_m . The second model represents the microscopic level,

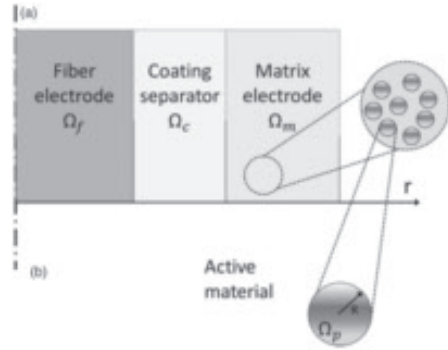


Figure 2. Schematic of the micro-battery computational domains. (a) On the macroscopic scale the micro-battery is divided in three domains, Ω_f , Ω_c and Ω_m , two phases are present in the matrix: the homogenized electrolyte mixture phase with respect to porosity and the solid active material phase. (b) The porous nature of the matrix electrode is considered by assuming spherical particles of active material in the positive electrode.

which has only one domain, Ω_p , the active material phase. It models a spherical particle of the positive electrode active material.

The two-way coupling between macroscopic and microscopic problem occurs by solving for the conservation of current for the ionically conducting electrolyte phase with equations (24) and (32), the material balances on the salt and solvent in the electrolyte phase use equations (22) and (23), and equations (30) and (31) in the Ω_c and Ω_m domains. These equations couple to equations (38) and (41) that define the flux of lithium exiting/entering the solid active phase into the electrolyte phase. The flux of lithium provides boundary conditions for using Fick's second law to characterize the diffusion of the lithium species in the active material particle in Ω_f and Ω_p domains, equations (21) and (28). The macroscopic model uses equation (36) for conservation of current for the electronically conducting solid phase, where the local current density $j_{loc,m}$ is solved for each r -coordinate in Ω_m using equations (42) and (43). $j_{loc,m}$ is dependent on the microscopic solution of the Li concentration in the active material particles in equation (28) in Ω_p domain, while the corresponding boundary condition equation (6) includes the flux of ions over the interface between the active particle surface and the electrolyte, equation (41) in Ω_m domain.

Intercalation-induced volume changes

As a result of battery operation, the composite unit cell will undergo volume changes. In the micro-battery cell model described as an axi-symmetric problem in Figure 1, an infinite long fiber is assumed. All shear stress components are equal to zero and the only non-trivial equilibrium equation is

$$\frac{\partial \sigma_r^k}{\partial r} + \frac{\sigma_r^k - \sigma_\theta^k}{r} = 0 \quad (44)$$

where σ_i^k are stress components in cylindrical coordinate system. The stress-strain relationship for transversely isotropic materials with intercalation-induced volumetric changes can be introduced through a thermomechanical analogy,¹⁹ where the dimensional changes are assumed to be proportional to the Li concentration, c

$$\sigma_i^k = C_{ij}^k \left(\varepsilon_j^k - \varepsilon_j^{k, \text{free swelling}} \right) \quad k = f, c, m \quad (45)$$

where index $k = m$ for the matrix, $k = c$ for the coating, and $k = f$ for the fiber, and $i, j = r, \theta, 1$ are cylindrical coordinates. Repeating indexes in equation (45) denote summation. C_{ij}^k is the stiffness matrix using Voigt notation, $\varepsilon_j^{k, \text{free swelling}}$ is the free swelling

strain in j -direction due to Li-ion intercalation which does not have shear components. For fiber $\varepsilon_j^{f, \text{free swelling}} = \beta_j^f \frac{c_f}{c_{f,max}}$, where β_j^f is constant coefficients of proportionality called intercalation-expansion coefficients to characterize the dimensional changes in the three directions. $\frac{c_f}{c_{f,max}}$ is the normalized Li concentration in the fiber, where c_f is the time-dependent Li concentration in the electrode material (equation (21)). $c_{f,max}$ is the maximum concentration reached when Li have intercalated into all available sites. The maximum Li concentration in the fiber is a physical property given by the specific capacity = 372 mAh/g⁵ and its density = 1780 kg/m³ for IMS65 carbon fiber. Similarly, the maximum concentration of lithium in the active material in the matrix is given by its specific capacity = 169 mAh/g and density = 3600 kg/m³.

The fiber is taken as a transverse isotropic material, with $C_{13} = C_{12}$, $C_{22} = C_{33}$, $\beta_r = \beta_\theta$.

The matrix material is assumed to be a particle composite with effective isotropic properties. The effective properties of matrix electrode material are calculated using the composite spheres assemblage introduced by Hashin,³⁰ assuming two phases present. The spherical LiFePO₄ active material represents the particle phase, and the remaining constituents (SBE, carbon black, and additional binder material) together comprise the so-called binder phase. The bulk modulus K is given by

$$K^* = K_b + (K_p - K_b) \frac{(3K_b + 4G_b)V_p}{3K_p + 4G_b - 3(K_p - K_b)V_p} \quad (46)$$

with superscript * denoting the effective property of the particle composite and subscripts b and p denote binder and particle phases, respectively. V is the volume fraction, and G is the shear modulus for each phase calculated by equation (47), where E is the Young's modulus and ν is the Poisson's ratio

$$G = \frac{E}{2(1 + \nu)} \quad (47)$$

The shear modulus for the particle composite is then given by

$$G^* = G_b + \frac{V_p}{1/(G_p - G_b) + 6V_p(K_p + 2G_b)/5G_b(3K_b + 4G_b)} \quad (48)$$

Since the matrix material is regarded macroscopically isotropic, Young's modulus, E^* , is calculated from the bulk and shear modulus

$$E^* = \frac{9K^*G^*}{3K^* + G^*} \quad (49)$$

The free swelling strain of the homogenized matrix, assuming $\beta_b = 0$, is given by

$$\varepsilon^{m, \text{ free swelling}} = \beta_p V_p + \frac{4(K_p - K_b)\beta_p G_b V_b V_p}{3K_b K_p + 4G_1(K_b V_b + K_p V_p)} \frac{c_p}{c_{p, \text{max}}} \quad (50)$$

where $\frac{c_p}{c_{p, \text{max}}}$ is the normalized Li concentration in the LiFePO_4 particle, calculated from equation (28).

Results and discussion

A galvanostatic (current controlled) discharge process is modeled. The rate for charging/discharging a battery is specified by means of C-rate. 1C is defined as the required current to obtain full charge or discharge in 1 h. The battery cannot be discharged below a certain level or permanent damage may be done to the battery, this voltage is called the ‘‘cut-off voltage,’’ it is set to 2.7 V.

It is natural to assume that the electrochemical cycling of the battery cell starts with a pristine fiber, i.e. without the presence of any Li in its structure, and with the active material particles in the matrix fully lithiated, which is also the stress-free state. After charging the lithium concentration in the fiber at the start of the simulation is assumed uniform, $c_f/c_{f, \text{max}} = 0.99$ and the battery is not stress free. The potential in the electrolyte phase is zero and the potential in the solid phase is the OCP. The discharge curves shown in Figures 3 and 4 correspond to the initial stress-free state when the matrix is fully lithiated.

Another possibility, requiring different manufacturing technique, is assuming stress-free state to be when the fiber is fully lithiated with all host sites for Li in the matrix material being empty. In this case the simulation starts with $c_f/c_{f, \text{max}} = 0.01$ for a delithiated fiber.

Effect of porosity of the positive electrode

The volume fraction of the solid active material in the positive electrode, ε_s^+ , affects the battery in terms of overall capacity. In Figure 3 the voltage drop during discharge for micro-batteries with identical geometries, i.e. fiber volume fractions and coating thickness, but with different positive electrode matrix compositions is shown.

The cell voltage is plotted against specific capacity, C_{spec} , defined as

$$C_{\text{spec}} = \frac{\int Idt}{m} \quad (51)$$

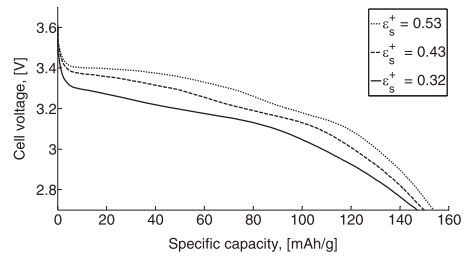


Figure 3. Discharge characteristics for different ε_s^+ when the fiber is considered stress free when delithiated during 1C discharge $V_f = 0.34$.

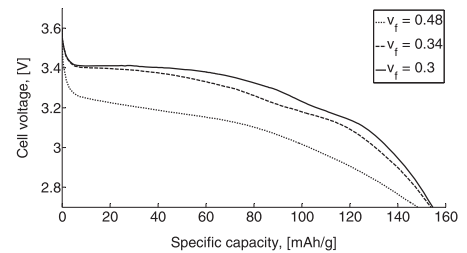


Figure 4. Discharge characteristics dependent on V_f when the fiber is considered stress free when delithiated during 1C discharge $\varepsilon_s^+ = 0.533$.

where $\int Idt$ is the summation of electric current delivered during the discharge time, t , and m is the mass of the electrochemically active material in the positive electrode (in the matrix material).

If ε_s^+ is low, the voltage drops faster and the capacity of the battery is lower because there is less active material into which Li can intercalate.

For a structural battery material, which must also possess mechanical performance, it is important not to focus solely on the voltage drop, which is greater for low porosities, but also consider factors affecting the stress distributions.

In addition to the high diffusion coefficient for the fiber that enables fast transport also a fairly slow discharging rate is used in this parametric study, which results in a uniform Li distribution in the fiber at all instants of time. The distribution of Li in the active material particles in the matrix is also fairly even; however, the magnitude of lithiation (average c_a) in the active material depends on the position in the matrix thickness direction.

At low ε_s^+ the active material particles uptake Li+ more evenly, whereas a high ε_s^+ in the matrix prohibits the Li^+ from effectively moving through the electrolyte

phase in the matrix in the radial direction, resulting in higher gradients of lithiated and partially lithiated active material across the positive electrode causing gradient in swelling behavior.

Effect of fiber volume fraction

In Figure 4 the voltage profiles for micro-batteries with positive electrodes with $\varepsilon_S^+ = 0.533$ in the matrix and thicknesses of 1, 1.7, and 2 μm during the constant current discharging at discharge rate of 1C are shown. The voltage drop (y-axis) in the discharge curve is increasing with increased fiber volume fraction. Also, the slopes appear different; higher slopes represent a higher internal resistance.

It should be noted that although the applied current, I_{app} corresponds to discharge rate 1C for all cases, the actual current differs for the different designs. The applied current is calculated for Li stored in the active material particles in the matrix material to be enough for extraction during 1 h. Since the amount of active material in the matrix material differs greatly between the different micro-battery designs, the

difference between the applied current is large. The charging/discharging rates affect the rated battery capacity. If the battery is being discharged very fast (i.e. the discharge current is high), then the amount of energy that can be extracted from the battery is reduced and the battery capacity is lower. This is because the components for the electrochemical reaction to occur do not have enough time to move to their necessary positions. Additional simulations with the same discharge current should be run in order to investigate the effect on polarization from internal resistance caused by changing micro-battery designs, and thus to exclude the combined effect of higher discharge rate and changes in V_f .

Effect of initial and boundary condition on volume changes

The analytical model proposed by Hashin, equations (46) to (50), was used to assess the effective elastic properties of the matrix material. The constituent material properties of the particle composite material used in this study are presented in Table 7. The

Table 7. Elastic properties of constituents in matrix material.

Constituents	Young's modulus (GPa)	Poisson's ratio (-)	Volume change (%)	Reference
Particle	$E_p = 125$	$\nu_p = 0.28$	$\beta_p = 7$	Zhang ²¹
Binder mixture	$E_b = 0.1$	$\nu_b = 0.3$	$\beta_b = 0$	Assumed

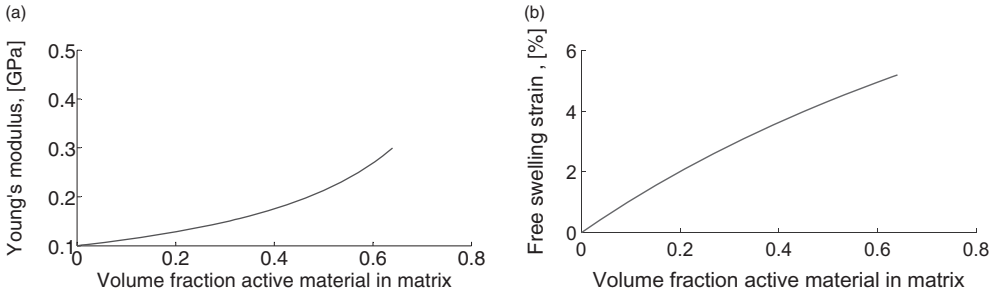


Figure 5. Effective properties. (a) Young's modulus and (b) the maximum swelling strain of the matrix electrode versus volume fraction ε_S^+ of the electrochemically active material.

Table 8. Elastic properties of fiber and coating.

Constituents	Young's modulus (GPa)	Poisson's ratio (-)	Volume change (-)	Reference
Fiber	$E_f^l = 300$ $E_f^z = 30$	$\nu_f^l = 0.2$ $\nu_f^{zl} = 0.45$	$\beta_z^f = 0.009$ $\beta_z^f = 0.05$	Jacques et al. ²⁰
Coating	$E_c = 0.1$	$\nu_c = 0.3$	$\beta_c = 0$	Assumed

influence of the volume fraction of the active material on material elastic modulus and swelling strain is shown in Figure 5.

The material properties for the fiber and coating is presented in Table 8.

Since the diffusion coefficients used in this study enable fast transport, concentration gradients are negligible at the time instant when the greatest volume change is to be expected, which represents the state most divergent from the initial state. Therefore, the axial swelling of the battery can be predicted in a simple and reliable manner by rule of mixture. The radial swelling behavior is very different depending on the two possible cases of the stress-free states discussed in the beginning of "Results and discussion" section.

The discharge in the stress-free state with a fully lithiated matrix in Figure 3 can be compared with the stress-free state with fully lithiated fiber (Figure 6). In the latter case, the electrochemical cycling starts with a discharge, which is shown in Figure 6 where the discharge voltages for different ϵ_s^+ are shown. It can be seen that for the so-called reference micro-battery design, with $\epsilon_s^+ = 0.533$ curves have similar appearance. Furthermore, one can see that the specific

capacity increases with decreased volume fraction of the active material, and also that the slope of the curve decreases with decreasing volume fraction active material.

It appears that these two different initial conditions generate different trends for the extracted capacity. These differences reflect themselves, in the maximum radial swelling strain and the specific capacity dependence on volume fraction of the active material shown for both initial stress-free states in Figure 7.

In Figure 7(a) it can be seen that the capacity normalized to the amount of active material in the positive electrode increases with increasing volume fraction of the active material. The maximum dimensional change occurs when the battery is fully charged, which leads to shrinkage of the battery in the radial direction. As the available amount of Li for intercalation is determined by the amount of active material in the matrix, it is natural that the swelling is less for a lower volume fraction active material in the matrix.

Figure 7(b) shows the opposite to Figure 7(a): the specific capacity is decreasing and the battery's swelling increases with increasing ϵ_s^+ . It should be noted that for the case of initially fully lithiated fiber the maximum swelling occurs at full discharge (cut-off voltage). The fact that the carbon fiber is lithiated in the stress-free

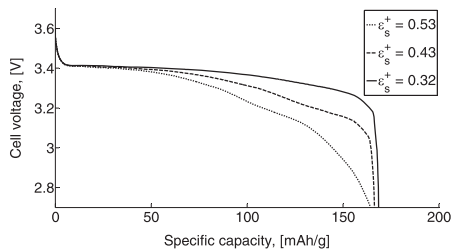


Figure 6. Discharge characteristics for different porosities when the fiber is considered stress free when lithiated. $V_f = 0.34$.

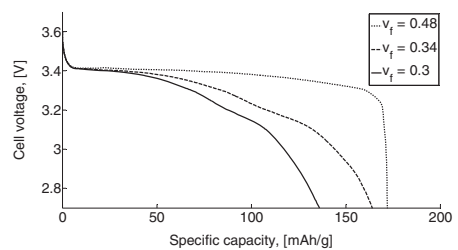


Figure 8. Discharge characteristics of various cell designs with $\epsilon_s^+ = 0.533$ when the fiber is considered stress free when lithiated.

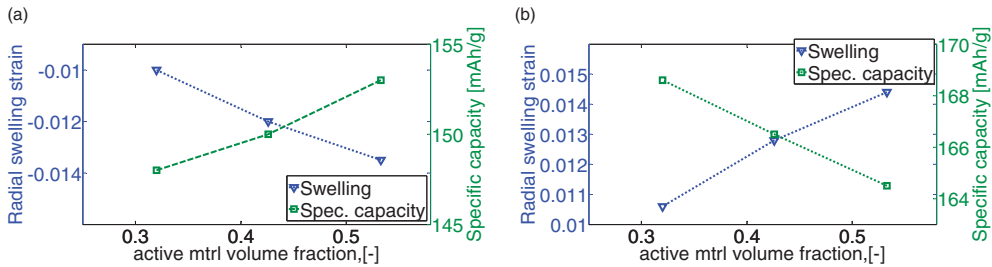


Figure 7. Radial swelling strain and specific capacity versus matrix porosity. (a) Fiber stress free when delithiated and (b) fiber stress free when fully lithiated from start. $V_f = 0.34$.

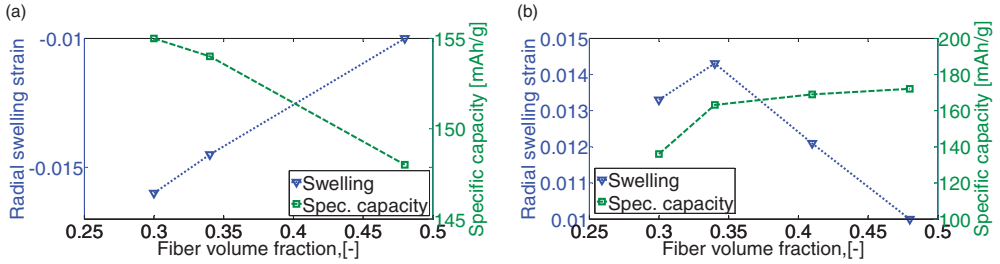


Figure 9. Radial swelling strain and specific capacity dependence on fiber volume fraction with constant $\epsilon_s^+ = 0.533$. (a) Fiber stress free delithiated and (b) fiber stress free fully lithiated.

state means that in the case of $\epsilon_s^+ < 0.533$ (which is the active material volume fraction when the two electrodes are balanced with regard to the intercalation ability) the amount of Li available exceeds the available sites in the matrix material. For low ϵ_s^+ a fairly large amount of Li is trapped inside the carbon fiber at the end of discharge, which means that the carbon fiber shrinks less than for high ϵ_s^+ . The reason why the dimensional change in the radial direction of the battery is positive, is the swelling of the matrix; which is greater than the shrinkage of the fiber; which dominates the global behavior for a fiber volume fraction of $V_f = 0.34$. A higher swelling for higher ϵ_s^+ , despite similar normalized Li utilization in the matrix is explained by the ϵ_s^+ dependency of the matrix material's properties, as shown in Figure 5.

In Figure 8 the discharge curves for batteries with different fiber volume fraction, but the same matrix composition, are shown for the case where the fiber is assumed to be fully lithiated at start.

It appears that for cells with different V_f , different initial conditions generate different trends for the extracted specific capacity and maximum radial swelling dependence on volume fraction of the active material. In Figure 9 these trends are shown for both initial condition assumptions.

Figure 9(a) shows that maximum radial shrinkage of the battery, which occurs at fully charged state, is less for higher V_f . To explain, we consider a pristine fiber and the active material in the matrix being fully lithiated at stress-free state in beginning of the electrochemical cycling. At fully charged state the fiber is swollen. For $V_f < 0.34$ there is more Li available in the matrix material than can be intercalated into the carbon fiber, and for $V_f > 0.34$ more available intercalation sites are in the carbon fiber than Li available in the system, meaning that the fiber swells more for lower V_f . The reason for negative global dimensional change for the battery in the radial direction is the greater shrinkage in the matrix material than the expansion of the fiber. Hence, higher V_f results in lower shrinkage extent.

When the initial stress-free condition is assumed to be a fully lithiated fiber and delithiated matrix, respectively, the cycling consequently starts with a discharge and the maximum radial swelling shown in Figure 9(b) occurs at the cut-off voltage. In this case the opposite applies concerning available sites for Li intercalation in each electrode, that is for $V_f > 0.34$ Li available from the carbon fiber exceeds the ability to be intercalated in to active material in the matrix, and for $V_f < 0.34$ there are more available sites for intercalation in the matrix than there is Li coming from the carbon fiber. In general, the maximum radial swelling decreases with increasing v_f , because the amount of fully lithiated matrix material surrounding the carbon fiber decreases resulting in Li enclosed in fiber, and the role of the fiber becomes more dominant. However, it can be seen that for very low fiber volume fraction ($V_f < 0.34$) the degree of swelling is slightly reduced again. The reason is that the radial size of the matrix material is too large to allow for efficient transport of Li^+ , meaning that the distribution of the Li in the matrix is nonuniform.

Conclusions

A framework for modeling a novel type of multifunctional composite material is presented, where a composite unit consisting of single carbon fiber microelectrode coated with an ion-conducting polymer electrolyte surrounded by a matrix material is considered as a micro-battery in a physics-based electrochemical model. Mathematical formulation for a single fiber lithium-ion battery under operation describing the electrochemical processes occurring is outlined. The modeled processes include (i) mass transport in electrolyte and in active electrode material particles, (ii) electrochemical reaction at active electrode material surfaces, and (iii) electronic and ionic conduction.

The multiscale character of the battery is addressed by coupling equations solved across the macroscopic domains of the battery (fiber electrode, coating

separator, and matrix electrode) and microscopic domains (active particle of the positive electrode). At macroscale the porous electrode model was extended for a SBE and coupled with a mechanical model, whereas at microscale Butler–Volmer kinetics was used for the Li^+ flux into the active material.

The effect on electrochemical and mechanical performance of altering the fiber volume fraction and the matrix composition in the structural battery was investigated, comparing the radial swelling and extracted capacity. When the fiber initially does not contain any Li, instead all Li is stored in the active material particles in the matrix, the swelling and capacity are conflicting properties, showing that an optimal design solution can be found.

However, simulations assuming that the system is stress free when the fiber is fully lithiated while the matrix is delithiated show that higher fiber volume content is favorable for both reduced mechanical swelling and electrochemical performance. Also a lower volume fraction of the active material in the matrix is beneficial when evaluating swelling and normalized capacity with respect to the mass of the active material.

Acknowledgement

KOMBATT-II project members are acknowledged for fruitful discussions.


Declaration of conflicting interests

The author(s) declared no potential conflicts of interest with respect to the research, authorship, and/or publication of this article.

Funding

The author(s) disclosed receipt of the following financial support for the research, authorship, and/or publication of this article: The Swedish Energy Agency, project 37712-1 is acknowledged for financial support.

ORCID iD

Johanna Xu  <http://orcid.org/0000-0003-3186-9561>
Göran Lindbergh  <http://orcid.org/0000-0001-9203-9313>

References

- Pereira T, Guo Z, Nieh S, et al. Embedding thin-film lithium energy cells in structural composites. *Compos Sci Technol* 2008; 68: 1935–1941.
- Asp LE and Greenhalgh ES. Structural power composites. *Compos Sci Technol* 2014; 101: 41–61.
- Snyder JF, Wong EL and Hubbard CW. Evaluation of commercially available carbon fibers, fabrics, and papers for potential use in multifunctional energy storage applications. *J Electrochem Soc* 2009; 156: A215–A224.
- Kjell MH, Zavalis TG, Behm M, et al. Electrochemical characterization of lithium intercalation processes of PAN-based carbon fibers in a microelectrode system. *J Electrochem Soc* 2013; 160: A1473–A1481.
- Hagberg J, Leijonmarck S and Lindbergh G. High precision coulometry of commercial PAN-based carbon fibers as electrodes in structural batteries. *J Electrochem Soc* 2016; 163: A1790–A1797.
- Jacques E, Kjell MH, Zenkert D, et al. Impact of electrochemical cycling on the tensile properties of carbon fibres for structural lithium-ion composite batteries. *Compos Sci Technol* 2012; 72: 792–798.
- Willgert M, Leijonmarck S, Lindbergh G, et al. Cellulose nanofibril reinforced composite electrolytes for lithium ion battery applications. *J Mater Chem A* 2014; 2: 13556–13564.
- Sun B, Mindemark J, Edström K, et al. Realization of high performance polycarbonate-based Li polymer batteries. *Electrochem Commun* 2015; 52: 71–74.
- Yue L, Ma J, Zhang J, et al. All solid-state polymer electrolytes for high-performance lithium ion batteries. *Energy Storage Mater* 2016; 5: 139–164.
- Liaw BY, Jungst RG, Nagasubramanian G, et al. Modeling capacity fade in lithium-ion cells. *J Power Sources* 2005; 140: 157–161.
- Fuller TF, Doyle M and Newman J. Simulation and optimization of the dual lithium ion insertion cell. *J Electrochem Soc* 1994; 141: 1–10.
- Doyle M, Fuller T and Newman J. Modeling of galvanostatic charge and discharge of the lithium/polymer/insertion cell. *J Electrochem Soc* 1993; 140: 1526–1533.
- Doyle M and Newman J. The use of mathematical modeling in the design of lithium/polymer battery systems. *Electrochim Acta* 1995; 40: 2191–2196.
- Ramadesigan V, Northrop PWC, De S, et al. Modeling and simulation of lithium-ion batteries from a systems engineering perspective. *J Electrochem Soc* 2012; 159: R31–R45.
- Cheng Y and Verbrugge MW. The influence of surface mechanics on diffusion induced stresses within spherical nanoparticles. *J Appl Phys* 2008; 104: 083521.
- Cheng Y and Verbrugge MW. Evolution of stress within a spherical insertion electrode particle under potentiostatic and galvanostatic operation. *J Power Sources* 2009; 190: 453–460.
- Cheng Y and Verbrugge MW. Application of Hasselman's crack propagation model to insertion electrodes. *Electrochem Solid-State Lett* 2010; 13: A128–A131.
- Botte GG. Modeling volume changes due to lithium intercalation in a carbon fiber. *Electrochim Acta* 2005; 50: 5647–5658.
- Pupurs A and Varna J. Modeling mechanical stress and exfoliation damage in carbon fiber electrodes subjected to cyclic intercalation/deintercalation of lithium ions. *Compos Part B* 2013; 65: 69–79.
- Jacques E, Hellqvist Kjell M, Zenkert D, et al. Expansion of carbon fibres induced by lithium intercalation for structural electrode applications. *Carbon* 2013; 59: 246–254.

21. Zhang W. Structure and performance of LiFePO₄ cathode materials: a review. *J Power Sources* 2011; 196: 2962–2970.
22. Nyman A, Zavalis TG, Elger R, et al. Analysis of the polarization in a Li-ion battery cell by numerical simulations. *J Electrochem Soc* 2010; 157: A1236–A1246.
23. Ekstedt S, Wysocki M and Asp LE. Structural batteries made from fibre reinforced composites. *Plast Rubber Compos* 2010; 39: 148–150.
24. Leijonmarck S, Carlson T, Lindbergh G, et al. Solid polymer electrolyte-coated carbon fibres for structural and novel micro batteries. *Compos Sci Technol* 2013; 89: 149–157.
25. Nyman A. *An experimental and theoretical study of the mass transport in lithium-ion battery electrolytes*. Stockholm: KTH, 2011.
26. Nyman A, Behm M and Lindbergh G. A theoretical and experimental study of the mass transport in gel electrolytes II. Experimental characterization of LiPF₆-EC-PC-P(VdF-HFP). *J Electrochem Soc* 2011; 158: A636–A643.
27. Newman J and Tiedemann W. Porous-electrode theory with battery applications. *AIChE J* 1975; 21: 25–41.
28. Hamann CH, Hamnett A and Vielstich W. *Electrochemistry*. Weinheim: Wiley-VCH, 2007.
29. Zavalis TG, Klett M, Kjell MH, et al. Aging in lithium-ion batteries: model and experimental investigation of harvested LiFePO₄ and mesocarbon microbead graphite electrodes. *Electrochim Acta* 2013; 110: 335–348.
30. Hashin Z. Analysis of composite materials – a survey. *J Appl Mech Trans Mech* 1983; 50: 481–505.

Paper II

Carbon fiber composites with battery function: Stresses and dimensional changes due to Li-ion diffusion

Johanna Xu¹, Göran Lindbergh² and Janis Varna¹

Journal of Composite Materials
2018, Vol. 52(20) 2729–2742
© The Author(s) 2018
Article reuse guidelines:
sagepub.com/journals-permissions
DOI: 10.1177/0021998317752825
journals.sagepub.com/home/jcm


Abstract

Structural composite materials that simultaneously carry mechanical loads, while storing electrical energy offers the potential of significantly reduced total component weight owing to the multifunctionality. In the suggested micro-battery, the carbon fiber is employed as a negative electrode of the battery and also as a composite reinforcement material. It is coated with a solid polymer electrolyte working as an ion conductor and separator while transferring mechanical loads. The coated fiber is surrounded by a conductive positive electrode material matrix. This paper demonstrates a computational methodology for addressing mechanical stresses arising in a conceptualized micro-battery and dimensional changes of the cell during electrochemical cycling, caused by time-dependent gradients in lithium ion concentration distribution.

Keywords

Micro-battery, carbon fibers, lithium ion, intercalation, swelling, stress state

Introduction

Since the research on high performance fiber-reinforced polymer matrix composites began in the early 1960s, the focus has been on improving their structural properties. Recently, research on multifunctional composite materials has started to accelerate, with a particular interest in structural power composites.^{1–4} A structural composite that undertakes the two roles of mechanical load bearing and electrical energy storage is an attractive solution, as both the reduction of vehicle weight and the electrification of vehicles can contribute towards meeting the increased requirements on lowered emissions.⁵

For this novel structural battery composite, lithium-ion (Li-ion) battery chemistry has been selected mainly because of its high specific energy. In a typical Li-ion cell, there are four main components, (i) the negative electrode connected to the negative terminal of the cell, (ii) the positive electrode connected to the positive terminal of the cell, and (iii) a separator preventing short circuiting and (iv) liquid electrolyte between the two electrodes. The electrodes consist of nano to micrometer sized electrochemically active electrode material particles, taking part in the electrochemical reaction,

mixed together with conductive additives and binder material. Examples of active electrode material are graphite (powder) in the negative electrode and lithiated metal phosphate (e.g. LiFePO₄) in the positive electrode, both serving as host materials allowing for lithium-ion extraction and insertion as the battery is charged and discharged. This insertion process of lithium active materials is called intercalation. In-depth information on Li-ion battery and their use can be found in Linden and Reddy⁶ and Hamann et al.⁷

When a lithium-ion battery is in use, i.e. during discharge, Li diffuses to the surface of graphite particles in the negative electrode where they undergo electrochemical reaction, and then the ions travel through the electrolyte solution via diffusion and ionic conduction to the positive electrode where they react and diffuse

¹Department of Engineering Sciences and Mathematics, Luleå University of Technology, Sweden

²School of Chemical Science and Engineering, KTH Royal Institute of Technology, Sweden

Corresponding author:

Johanna Xu, Luleå University of Technology, Luleå 97187, Sweden.
Email: Johanna.Xu@ltu.se

towards the inner regions of the LiFePO_4 particles. During charging, the process is reversed.

To introduce an energy storage feature in the structural composites, it is necessary to stipulate additional requirements for the constituent materials to allow the above-mentioned mechanisms to take place. The role of the carbon fiber, see Figure 1, must be extended from only carrying load to also function as an active electrode material in a battery, allowing for lithium intercalation. The matrix material contribution extends beyond acting as load transfer to also function as electrode material. With two electrodes, one negative (fiber) and one positive (matrix), two additional functions are required in order to realize a battery, namely a separator to prevent short circuiting, and electrolyte for ion transportation. In conventional batteries, these two functions are often incorporated into one material, a separator soaked in liquid electrolyte. It is apparent that a liquid cannot be part in the material if it is to carry structural load while delivering electrical energy. The liquid electrolyte needs to be replaced with a solid polymer electrolyte (SPE)⁸⁻¹¹ interphase between the fiber and the matrix. The purpose of the SPE material in this energy storage structural composite material is to transfer load, act as an ion conductive medium and to prevent short-circuiting. A major drawback for using SPE is the decreased ion conductivity with increased electrolyte stiffness. However, the effect of low ion conductivity is overcome in the suggested micro-battery cell design, reducing the thickness of the electrolyte to a less than $1\ \mu\text{m}$ by electropolymerization.¹²

Within this conceptualized micro-battery design, each repeating unit is a concentric cylinder assembly where the negative electrode consists of one single carbon fiber, coated with a thin layer of SPE embedded in matrix cylinder (the positive electrode).

In a traditional Li-ion battery development, the capability to deliver electrical charge at different charging/discharging rates is an important battery performance metric, affected by several parameters, including the ionic conductivity of the electrolyte, distance between

the electrodes, the diffusivity of Li in the electrodes and electrical conductivity of the electrodes.¹³ The rate for charging/discharging a battery is specified by means of C-rate. 1C is defined as the required current to obtain full charge or discharge in 1 h, 10C in 1/10 h. In this study, the effect of Li diffusion coefficient in the carbon fiber on Li distribution is investigated for different C-rates.

During electrochemical cycling (repeated charging/discharging), the constituents of the three-cylinder unit undergo volume changes due to the migration of lithium ions between them. These volume changes together with the applied mechanical load affect the internal stress state, potentially causing micro damage formation in the material, which results in electrical and mechanical performance degradation.

The Li diffusion in a carbon fiber and the resulting internal stresses, possibly causing damage formation has been studied in Pupurs and Varna¹⁴ and Cheng and Verbrugge.¹⁵ In the work by Pupurs and Varna,¹⁴ the internal stresses in the fiber due to Li concentration gradients were studied, with the simplification that the fiber is surrounded by an infinite source of Li^+ and it is not constrained by surrounding materials, which allowed the Li concentration distribution in the fiber to be calculated as a heat conduction problem with convection boundary conditions. It was shown that high hoop stresses during deintercalation can initiate radial crack growth in the fiber and that during subsequent intercalation cycles, arc cracks may deflect from this radial crack. These two types of cracking were analyzed using linear elastic fracture mechanics approach. However, in the present paper, we will show that (a) the Li concentration is different than in Pupurs and Varna¹⁴; (b) the fiber stresses are not the result of the Li concentration gradient only; the effect of the mechanical interaction between the coated fiber and the matrix (during Li diffusion one of them is swelling and the other one is shrinking) has to be accounted for in a proper analysis.

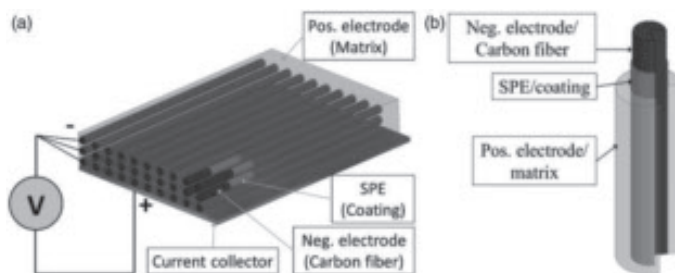


Figure 1. (a) Schematics of Li-ion battery operating principle. (b) Micro-battery.

This paper demonstrates computational methodology for addressing mechanical stresses arising in the carbon fiber, at its interface and in the matrix in a conceptualized micro-battery cell during electrochemical cycling. Physics-based mathematical modeling is used to analyze the following electrochemical processes simultaneously:

- Mass transport in active materials.
- Mass transport in electrolyte.
- Electronic conduction.
- Electrochemical reaction at the surface of the active material.

The objective of the present paper is to analyze the following:

- The effect of carbon fiber diffusion coefficient on Li distribution for different charge rates. The micro-battery is charged from its fully discharged state (no Li in fiber), with charge/discharge rates corresponding to 1C and 10C. At full charge, the subsequent discharging takes place without any resting period.
- Swelling and shrinking of the carbon fiber micro-battery due to Li diffusion as affected by elastic properties of constituents.
- The effect of the charge rate on stress distribution in the carbon fiber, at the fiber/electrolyte interface and in the matrix caused by Li distribution.

Theoretical background

Design considerations

In the conceptual cylindrical micro-battery, see Figures 1(a) and 2(a), the negative electrode is an

individual carbon fiber coated by a gel electrolyte (lithium salt and solvent dissolved in a polymer) surrounded by a solid positive electrode (matrix). The positive electrode partially consists of electrochemically active material LiFePO_4 , i.e. the Li host material.

The positive electrode (matrix) is the source of lithium, providing lithium to the negative electrode (fiber) during the first and subsequent charges. The Li-ions carry the current within the battery from one electrode to the other. However, the ability to intercalate Li differs between the LiFePO_4 active material in the matrix and the carbon fiber. It is desirable to have a balanced cell composition, where the ability to intercalate Li is equivalent for the two electrodes. The matrix volume fraction in the multifunctional composite is adjusted to ensure this balance. The maximum Li concentration in the fiber is a physical property given by the specific capacity = 372 mAh/g¹⁶ and its density = 1780 kg/m³ for IMS65 carbon fiber. Similarly, the maximum concentration of lithium in the active material in the matrix is given by its specific capacity = 169 mAh/g and density = 3600 kg/m³.

The fiber used in this study is an intermediate modulus carbon fiber, with a radius $r_f = 2.5 \mu\text{m}$. The coating thickness is set to $r_c = 0.1 \mu\text{m}$, and the outer radius of the micro-battery system is calculated to be $r_m = 4.3 \mu\text{m}$ in order to fulfill the matching in intercalation ability, from which it can be realized that the matrix thickness is 1.7 μm and the fiber volume fraction in the composite material is $V_f = 0.34$.

Stresses in micro-battery due to ion migration

The mechanisms of lithium ion intercalation in the structure of carbon fibers are still not fully understood. Empirical studies have shown that the ability to intercalate Li-ion is far superior for PAN-based fibers with

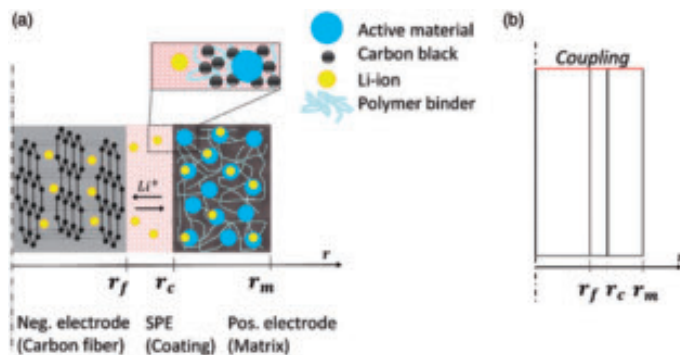


Figure 2. (a) Schematics of micro-battery constituents. (b) Model geometry.

intermediate modulus than fibers with high and ultra-high modulus fibers.¹⁷ The turbostratic microstructure of these fibers which also contains amorphous parts are suggested to be favorable for Li-ion intercalation. It is believed that lithium intercalation leads to changes in the crystal lattice of the carbon fiber, both in the direction of basal planes and interplane, resulting in dimensional changes of the carbon fiber, corresponding well with experimental observations in Jacques et al.¹⁸ In linear elasticity theory, these dimensional changes are assumed to be proportional to the Li concentration, c . In the concentric micro-battery, where the concentration distribution is not uniform and the carbon fiber is constrained by the battery constituent materials, intercalation induces stresses.

For a transverse isotropic material, two different constant coefficients of proportionality called intercalation-expansion coefficients are required to characterize the dimensional changes in the three directions.

The stress-strain relationship for transversely isotropic active materials with intercalation induced volumetric changes can be introduced through a thermo-mechanical analogy.¹⁴

$$\sigma_i^k = C_{ij}^k \left(\varepsilon_j^k - \beta_j \frac{c_k}{c_{k,max}} \right) \quad k = f, c, m \quad (1)$$

where index $k = m$ for the matrix, $k = c$ for the coating, and $k = f$ for the fiber, and $i, j = r, \theta$ are cylindrical coordinates. C_{ij}^k is the stiffness matrix using Voigt notation. Here $\beta_j \frac{c_k}{c_{k,max}}$ is the free swelling strain in j -direction due to Li-ion intercalation which does not have shear components. $\frac{c_k}{c_{k,max}}$ is the normalized Li concentration in the active material, where c_k is the time-dependent Li concentration in the active material, $c_{k,max}$ is the maximum concentration corresponding to Li intercalated into all available sites in the host materials. The maximum Li concentration in the fiber is a physical property given by the specific capacity¹⁶ of the active material and its density.

For a transversally isotropic material $C_{13} = C_{12}, C_{22} = C_{33}, \beta_r = \beta_\theta$.

For an axi-symmetric problem, (Figure 2(b)), assuming an infinite long fiber, when all shear stress components are equal to zero, the only non-trivial equilibrium equation is

$$\frac{\partial \sigma_r^k}{\partial r} + \frac{\sigma_r^k - \sigma_\theta^k}{r} = 0 \quad (2)$$

The strain relationship to radial displacement u_r is given by

$$\varepsilon_r^k = \frac{\partial u_r^k}{\partial r} \quad \varepsilon_\theta^k = \frac{u_r^k}{r} \quad \varepsilon_l = \varepsilon_{10} = \varepsilon_{1f} = \varepsilon_{1m} = \varepsilon_{1c} \quad (3)$$

The third expression in equation (3) states that axial strains are the same in all constituents, where ε_{10} is an unknown constant axial swelling strain of the micro-battery. The displacement and stress solutions obtained for each phase separately must satisfy the following interface conditions:

- (i) Radial displacement must be zero on the symmetry axis.
- (ii) Radial displacement and radial stress continuity at all interfaces.
- (iii) Outer boundary of the cylinder assembly is stress-free.

Lithium concentration distribution in carbon fiber

The lithium transportation in the negative electrode, which is composed exclusively of the active material, the carbon fiber, is described by Fick's law of diffusion¹⁹

$$\frac{\partial c_f}{\partial t} = \nabla \cdot (D_f \nabla c_f) \quad (4)$$

where subscript f denotes the fiber phase, D is the diffusion coefficient, t is the time, and ∇ is the Nabla operator. Boundary conditions are

$$-D_f \frac{\partial c_f}{\partial r} \Big|_{r=0} = 0 \quad -D_f \frac{\partial c_f}{\partial r} \Big|_{r=r_f} = J_f(t) \Big|_{r=r_f} \quad (5)$$

where J_f is the molar flux at the carbon fiber surface describing the process kinetics, which depends on the exchange current density and the overpotential. The electrochemical reaction kinetics yielding the molar flux J_f at the electrode surface is given by the Butler-Volmer equation⁷

$$J_f \Big|_{r=r_f} = i_{0,f} \left[\exp \left(\frac{\alpha_a F \eta_f}{R_g T} \right) - \exp \left(- \frac{\alpha_c F \eta_f}{R_g T} \right) \right] \quad (6)$$

where R_g is the universal gas constant, F is the Faraday constant, $i_{0,f}$ is a material property termed exchange current density which is the rate of oxidation and reduction at equilibrium, $\alpha_a = 0.5$ and $\alpha_c = 0.5$ are the electrochemical reaction symmetry factors, and η_f is the overpotential defined as

$$\eta_f \Big|_{r=r_f} = \Phi_{s,f} - \Phi_{e,c} - E_{OCP,f} \quad (7)$$

where $\Phi_{e,c}$ is the electrolyte phase electric potential in the SPE coating, resulting from concentration distributions of salt and solvent in the coating, and $\Phi_{s,f}$ is the solid phase electrical potential for the fiber (here the

carbon fiber is assumed to be grounded, $\Phi_{s,f} = 0$, E_{OCP} is the electrode equilibrium potential, a material property describing the potential observed experimentally at zero current.

Similar equations as (4) to (7) are describing the Li concentration in the active material of the matrix and the flux on the surface of the active material in the matrix.

The solid phase electric potential is calculated by Ohm's law describing the relation between the electric field, current density and material effective conductivity, $\sigma_{eff,m}$, in the micro-battery, with the applied current density as boundary condition

$$-\sigma_{eff,m} \left. \frac{\partial \Phi_{s,m}}{\partial r} \right|_{r=r_m} = I \quad (8)$$

where the current density I is related to the applied current i_{app} at the outer surface of the battery, A , as

$$I = i_{app}/A \quad (9)$$

It has to be realized that in order to assess lithium concentration distribution in the carbon fiber (negative electrode), c_f , equation (4), also electrolyte phase charge and mass balances need to be described. The macroscopic modeling of the mass transport in the electrolyte is adapted from work by Nyman et al.²⁰

In summary, the model to describe the ion concentration distribution in this micro-battery consists of a coupled system of 11 nonlinear partial differential equations (PDE) with 11 unknowns, which are: 2 active material concentrations c_f , c_a , 2 concentrations in the polymer electrolyte coating containing both salt and solvent $c_{salt,c}$, $c_{solvent,c}$, 2 concentrations in the matrix material consisting partially of the polymer electrolyte, $c_{salt,m}$, $c_{solvent,m}$, 3 potentials $\Phi_{e,c}$, $\Phi_{e,m}$, $\Phi_{s,m}$, and 2 fluxes J_f and J_m . The governing equations along with corresponding boundary conditions are discussed in detail in Xu et al.²¹

COMSOL model

COMSOL Multiphysics 5.2²² software is employed to model the concentration distributions during Li intercalation and deintercalation. The electrochemical model is formulated for a cylindrical coordinate system to describe the Li diffusion in and out of the electrodes in conjunction with appropriate boundary conditions.²¹

An axisymmetric representation is used to model the three concentric phases, the mechanical stresses are obtained by assuming generalized plane strain conditions, $\varepsilon_1 = \varepsilon_{10} = const$. Further, the carbon fiber is considered stress free with no lithium present, i.e. in a fully

discharged state. The matrix material is also stress free in the discharged state, when it contains the highest lithium concentration. For convergence reasons, the initial concentration in the fiber was set as a small non-zero value.

Results and discussion

Input parameters

The electrochemical properties of the carbon fiber are extracted from Kjell et al.²³ for PAN-based IMS65 carbon fiber. The electrochemical properties of the gel polymer electrolyte are adopted from an extensive characterization study for a gel polymer in Nyman et al.²⁰ Both the composition and the electrochemical properties for the positive electrode (matrix) material are assumed to correspond to Zavalis et al.²⁴

The experimentally measured diffusion coefficient of the carbon fiber²³ shows strong concentration dependence, $D = D(c)$, ranging over three orders of magnitudes. The effect of the diffusion coefficient is studied by adopting in simulations two extreme constant values (low and high), Table 1, and comparing two different charge/discharge C-rates; 1C and 10C. Considering the relatively low ionic conductivity of the SPEs, these C-rates might be too high to enable sufficient transport. However, the gel polymers used in this study have higher conductivity than SPEs, and researchers are constantly striving to achieve higher conductivities for SPEs. Also, SPE may give a higher ion-conductivity at elevated temperatures, in such case, the temperature effects on the mechanical properties of all the components should be considered during modelling. However, this is outside the scope of this study, which only considers isothermal conditions.

The applied current (i_{app}) for one cycle has the same C-rate during charge and discharge without any break between these two steps.

The input parameters for the mechanical model are listed in Table 2. The free swelling strain in the fiber axial direction was obtained by fitting experimental data from Jacques et al.¹⁸ The radial swelling coefficient for carbon fibers is not available in literature, but it has been approximated from observations.⁴

The expansion coefficients $\beta_z^c = \beta_z^m = \beta_r^c = \beta_r^m = 0$ can be interpreted as no macroscopic swelling due to intercalation. In fact, swelling in the active material

Table 1. Fiber diffusion coefficients used in this study.

Parameter	Low	High
Diffusion coeff. of carbon fiber, $D_f(\text{m}^2/\text{s})$	10^{-14}	10^{-11}

particles which are constituents of the matrix does occur, causing a change in volume fraction of the active material in the matrix. Since the description of the resulting matrix swelling is rather complex and depends on the porous matrix microstructure, we simplify the analysis by setting the overall expansion coefficient of the matrix to zero for the reference elastic property data set and using it as a parameter in following analysis. Swelling of the coating is neglected, because the properties are unknown, and the stiffness and thickness are very low, and hence insignificant influence on stresses expected.

In addition to the reference case presented in Table 2, calculations were also performed with 10 times higher elastic modulus of the coating and the matrix, and a non-zero expansion coefficient for the matrix $\beta_m^c = \beta_m^z = 0.05$.

Charge rate and diffusion coefficient

The battery is operable in a certain voltage interval, outside this range the battery system risks chemical instability and damages,⁶ which is outside the scope

of this present study. The battery is operable until the cell voltage, E_{cell} , defined as the potential difference between the solid phase electrical potential of the matrix and solid phase electrical potential at the fiber surface, reaches the upper and lower cut-off voltage; the highest and lowest voltage at which the system is allowed to operate, respectively. In the modeled system, the upper cut-off voltage is set to 3.6 V and the lower cut-off voltage to 2.7 V, commonly specified by battery manufacturers.^{24,25}

The lithium concentration profiles during the charge/discharge cycle, Figure 3, for various time instances in the charge/discharge, given in Table 3, show the influence of the diffusion coefficient in combination with the charge/discharge rate.

In Figure 3, the difference in Li concentration gradients corresponding to the two diffusion coefficients is shown. In the case of 1C charge/discharge rate (Figure 3(a)) slow diffusion in the fiber (solid lines) leads to small but noticeable gradient in the beginning of the charge, which is maintained throughout charging, and then mirrored during discharging. During

Table 2. Elastic constants and expansion coefficients of constituents: Reference case.

Constituent	E_z (GPa)	E_r (GPa)	ν_{zr} (-)	$\nu_{r\theta}$ (-)	Expansion	
					$\beta_z(-)$	$\beta_r(-)$
Fiber	300	30	0.2	0.45	0.009	0.05
SPE coating	0.1	0.1	0.3	0.3	0	0
matrix	0.3	0.3	0.3	0.3	0	0

Table 3. Time instants of studied concentration and stress distributions during the charge/discharge.

Designation	Progression in the charge/discharge cycle
a	After the onset of charging
b	Half-way through charging
c	Before the end of charging
d	After the onset of discharging
e	Half-way through discharging
f	End of discharging

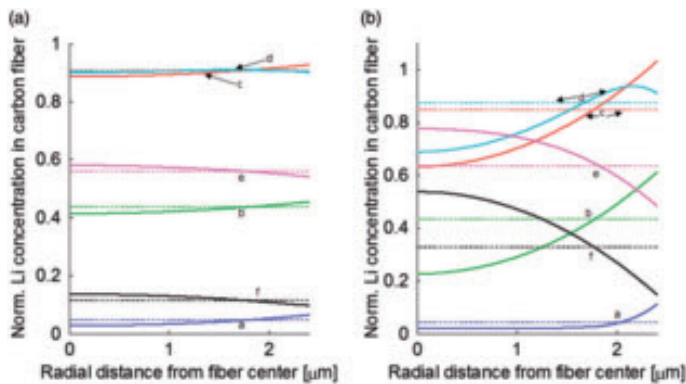


Figure 3. Li distribution in fiber radial position during (a) 1C charge/discharge rate, (b) 10C charge/discharge rate; slow diffusion (solid lines) and fast diffusion (dotted lines) for time instants given in Table 3.

the charging (curves a, b c), the Li concentration is always higher at the fiber surface than on the axis. The normalized concentration never reaches 1, because of the conservatively set upper cut-off voltage. When the discharging starts, the Li concentration is first reduced at the fiber surface, whereas in the region close to the fiber axis, the concentration may still slightly increase, a process driven by the previously created concentration gradient. With continued discharging, the Li concentration is always lower in the fiber surface region. In contrast, when the diffusion is fast, there are no discernible concentration gradients. The average Li concentration in the considered slow diffusion case is rather close to the value in the fast diffusion case.

At 10C charge/discharge, the previous observation regarding uniform concentration distributions for a fast diffusion remains. A slow diffusion shows highly non-uniform concentration distribution in the fiber, with a slope changing dependent on the charge/discharge progression. The discussion regarding the 1C rate case given above is still applicable, the effects are just even more pronounced.

In the beginning of the charge in the case of low diffusion coefficient, the Li supply from the electrochemical reactions to the fiber surface exceeds the ability to transport Li from the fiber surface to the center of the fiber, which remains empty of Li for a time, before the concentration of Li begins to increase. For the rest of the charge interval, the rate of the concentration change with time is rather similar at the surface and at the center of the fiber as shown in Figure 4. If the diffusion coefficient is high, the difference between concentration in the center of the fiber and on the surface is negligible.

The time-dependent gradients in Li concentration distribution in the carbon fiber obtained through multi-physics modeling differ from the concentration profiles presented by Pupurs and Varna¹⁴ and Cheng and

Verbrugge,¹⁵ where the concentration gradients are decreasing during charging, until finally becoming uniform. This shows that assumptions (boundary conditions) made in order to obtain Li concentration profiles through analytical series expansion are oversimplified. To perform an accurate analysis of mechanical stresses caused by non-uniform fiber swelling, gradients in Li concentration distribution should originate from modeling all the physical events (mass transport in active material, mass transport in electrolyte, electronic conduction and electrochemical reactions).

The diffusion coefficient is directly related to whether the concentration gradients arise in the fiber: fast diffusion results in no gradients regardless of the two used charge/discharge rates. However, the gradients that occur during slow diffusion show a dependence on the charge/discharge rate.

Since the influence of charging/discharging rate is noticeable only for a low diffusion coefficient, from now on, the stress analysis will only consider a slow diffusion in fiber ($D_f = 10^{-14} \text{ m}^2/\text{s}$) with charge/discharge rates corresponding to 1C and 10C.

Macroscopic swelling

The swelling strain of the micro-battery is the largest at the end of the charge when the Li concentration in the fiber is as shown in Figure 3 and the Li concentration in the matrix as shown in Figure 5. The swelling strain of the composite micro-battery at the end of the charge calculated using the stress model described in 'Stresses in micro-battery due to ion migration' section is shown in Figures 6 and 7. Results for three cases of matrix Young's modulus (0.3 GPa, 1.5 GPa and 3 GPa), two extreme cases of matrix swelling (no swelling and 0.05 swelling coefficient) and two cases of charge rate (1C and 10C) are presented. Thus, the results cover a range of all possible combinations within these extreme cases.

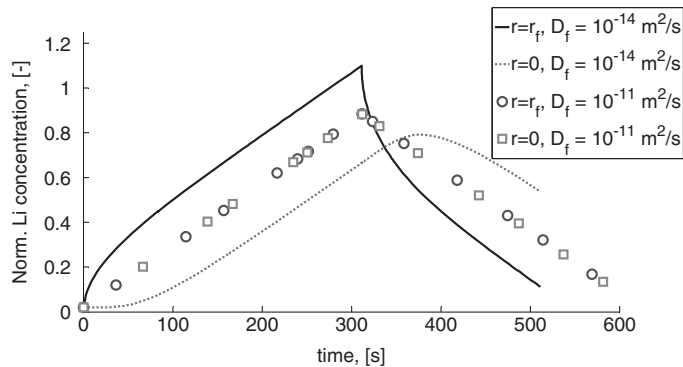


Figure 4. Lithium concentration in carbon fiber center and at surface, respectively, for 10C charging/discharging.

The calculated longitudinal swelling strain for different combinations of matrix stiffness and swelling coefficients is shown in Figure 6. At full charge, the total amount of Li in the fiber differs for the two charging

rates; hence, a higher degree of swelling for 1C charging than 10 C charging can be read in Figure 6. It can be seen that for the case with no matrix/cathode swelling, a 10-fold increase in matrix stiffness gives very little contribution to lowering the longitudinal macroscopic swelling. However, the stiffness of the matrix has significant impact when the matrix material also experiences volume changes during electrochemical cycling: a higher stiffness renders less longitudinal swelling of the battery and the dependence is rather linear.

A simple one-dimensional analytical model based on force balance and iso-strain assumption was used to explain this behavior. Analytical expression for the longitudinal expansion strain is

$$\epsilon_1 = \frac{E_z^f V_f \beta_z^f \Delta c_{fn} + E_m V_m \beta_m^m \Delta c_{mn}}{E_z^f V_f + E_m V_m} \quad (10)$$

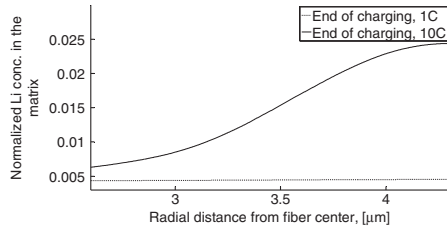


Figure 5. Li distribution in matrix during 1C (dotted lines) and 10C (solid lines), at the end of charging.

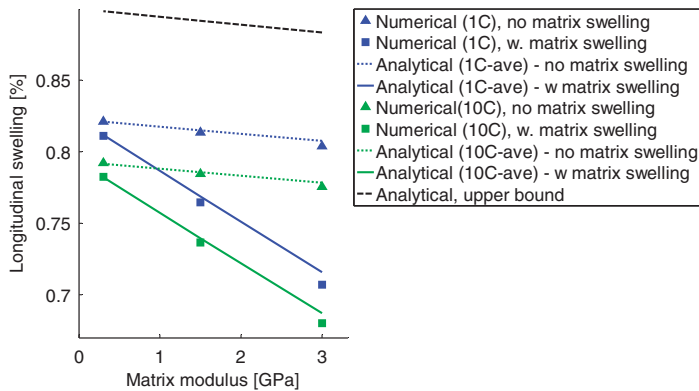


Figure 6. Longitudinal swelling strain at the end of the charge, as a function of matrix modulus, with 1C and 10C charge/discharge rate.

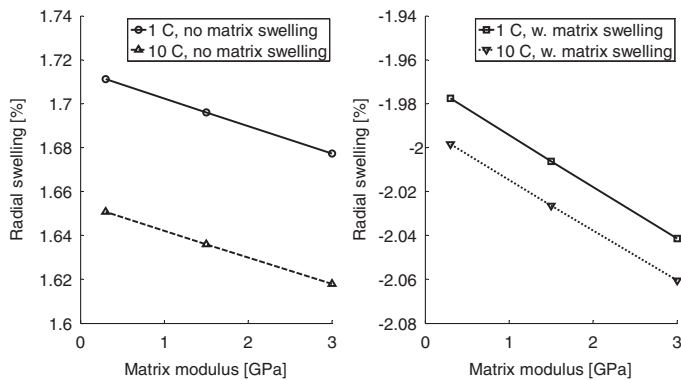


Figure 7. Radial swelling strain at the end of charging (1C and 10C charge rates) as a function of matrix stiffness, a) with matrix swelling and b) without matrix swelling.

The effect of the coating is neglected in this expression. Δc_{fn} and Δc_{mn} are average concentration changes with respect to the initial state (when no Li is present in fiber, and matrix has maximum possible Li content). Δc_{fn} is calculated from Figure 3, and Δc_{mn} is calculated from Figure 5. According to equation (10), if the matrix is not swelling, the matrix modulus which is much lower than the fiber modulus enters only the denominator in equation (10) and the effect of swelling is small. In contrary, if β^m is large, the effect of the matrix modulus is more significant.

In all presented cases, the longitudinal swelling strain calculated from the analytical model using the real average concentrations is in a good agreement with numerical results. If the matrix is not swelling the agreement is excellent.

The upper bound analytical value of the swelling strain can be calculated using the maximum uniform Li distribution in the fiber and no extractable Li is present in the matrix. This situation would correspond to a very slow charge ($\ll 0.1C$) introduced shortly before a full charge is reached. This would allow the concentration gradients to relax, and would also result in an increase in amount of Li in the carbon fiber before upper voltage limit is reached. In this case, the longitudinal swelling strain of the micro-battery would asymptotically increase approaching the curve “Analytical, upper bound” in Figure 6. It can be seen that the “Analytical, upper bound” greatly exceeds the swelling strain obtained from numerical calculations, because the real Li concentration due to cut-off is lower than the assumed in “Analytical, upper bound.”

The free radial swelling strain occurs as the composite unit in Figures 1 and Figure 2 changes its outer radius without any external constraint, see Figure 7

where the radial swelling strain is defined by expression $\varepsilon_r = u_r(r_m)/r_m$.

The biggest difference compared to the longitudinal swelling is a negative radial dimension change of the unit, i.e. radial shrinkage of a fully charged micro-battery when the matrix material shrinkage is accounted for, Figure 7(b). The radial shrinking of the composite unit occurs as a result of Li leaving the matrix, causing the matrix to shrink, and then as Li enters the fiber, the fiber swells and pushes the electrolyte prohibiting the matrix hoop shrinkage at that boundary. There is also a Poisson’s ratio contribution adding to the shrinkage: (a) tension to the matrix in the hoop direction leads to contraction in the radial; (b) tensile swelling strain of the micro-battery leads to shrinkage of the matrix in radial direction. As an adaption to these constraints, the matrix at the outer radius shrinks even more.

Since the results in Figure 7 show that the expansion of the composite in the radial direction can be positive as well as negative, it may be possible to optimize the swelling of the matrix during material development in order to minimize the radial swelling of the composite micro-battery by “tailoring”.

Stress distributions

Stresses at the fiber surface. Stresses at the carbon fiber boundary during charge/discharge cycle for slow diffusion are shown in Figures 8 and 9. The elastic modulus and the swelling coefficient of the matrix are used as parameters in simulations.

It can be seen that the contribution from matrix swelling to the stresses at the fiber surface is limited in the case of low matrix stiffness, regardless of the rate of charging/discharging. It is clear that increased matrix stiffness is unfavorable for the stresses in the

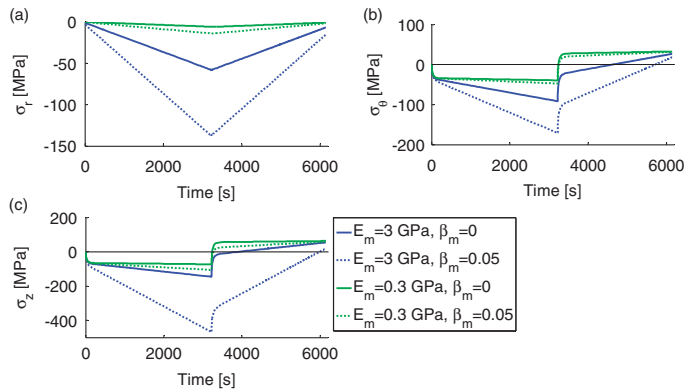


Figure 8. Stresses at fiber boundary as a function of time for 1C charging/discharging, with slow Li diffusion in the carbon fiber.

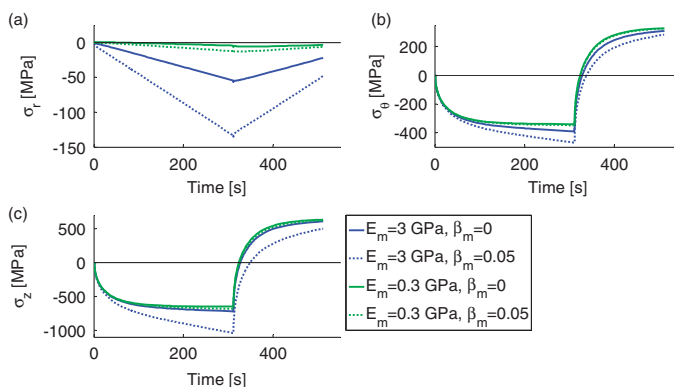


Figure 9. Stresses at fiber boundary as function of time for 10C charging/discharging, with slow Li diffusion in the carbon fiber.

fiber, which is further emphasized when matrix undergoes volume changes as well.

During charging, all stress components in the fiber at the surface are compressive. The radial stress change is very similar for both charge rates, whereas other stress components are much larger at 10C charge rate. Differences between 1C and 10C charge rate can be explained by two phenomena: (a) the matrix shrinkage during charging and (b) the non-uniform Li concentration distribution in the fiber. In the 1C case, the concentration distribution in the fiber is much more uniform than in the 10C case (compare Figure 3(a) and (b)). Therefore, in 1C case, the compressive radial and axial stresses during charging, Figure 8, are mostly due to interaction with the matrix, and the interaction is stronger when the matrix is stiff and prone to shrinkage. In the 10C case, the Li distribution in the fiber is very non-uniform and different regions of the fiber have different values of the free expansion strain. Thus, in addition to the interaction with the matrix, the force balance between different fiber regions affects the stress distribution: during charging, the Li concentration in the fiber surface region is higher than in the bulk and this region tends to expand more than the bulk part. This results in rather small change of the radial stress at the interface, but the axial compressive stress at the fiber surface, see Figure 9(c), is much higher because now not only the matrix but also the bulk part of the fiber resists the expansion of the fiber surface region. The hoop stress, σ_θ , at the surface is negative during the charging because the expansion in this direction is constrained by the surrounding matrix and in 10C case also by the bulk of the fiber.

During discharging, the stress building mechanisms are the same but the process is reversed. For example, the outer fiber region, close to the fiber/SPE interface, which in 10C charge rate case contains considerably

less Li than the bulk, attempts to contract in the θ direction. The contraction is constrained by the inner region which due to the still high concentration of Li, contracts much less, resulting in tensile hoop stresses in the outer region. Contribution of the matrix to this process is rather small. At the end of the discharge, corresponding to the cut-off voltage, there is still certain non-uniform Li distribution in the fiber, which is the reason for stresses at the end of the cycle. The conclusions from the above analysis are: (i) since radial stresses are always compressive, the fiber/coating interface failure is unlikely; (ii) at high discharge rate, large tensile hoop stresses develop which may lead to initiation of radial cracks in the fiber; (iii) large axial tensile stresses during discharge may initiate fiber breaks.

Radial distribution of stresses in the fiber. In order to analyze potential damage growth in the carbon fiber induced by charge/discharge, the stress distributions along the carbon fiber radial direction are needed. Figures 10 and 11 show stress distributions in the fiber for different matrix elastic properties at 1C and 10C charging/discharging rate in the instant, when the upper voltage limit is reached. Figures 12 and 13 show stresses at the lower cut-off voltage.

Charging with 1C stresses have rather uniform distribution when the battery cell is fully charged, this is due to the charge rate being sufficiently slow for enabling the Li transport inside the carbon fiber. Note that the stress distributions would be uniform and $\sigma_r = \sigma_\theta$ if the Li concentration distribution is uniform. Stress components in the fiber in the 1C case are very sensitive to the value of the matrix modulus. The effect of the swelling in the matrix on fiber stresses as a result of intercalation is rather small for a low modulus matrix, but if the matrix is stiff, the matrix swelling has significant influence. For a 10C charging/discharging

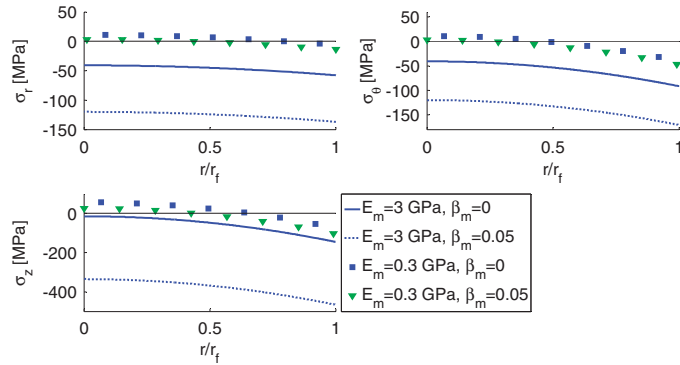


Figure 10. Stress distribution along fiber radial direction at full charge with 1C charge rate.

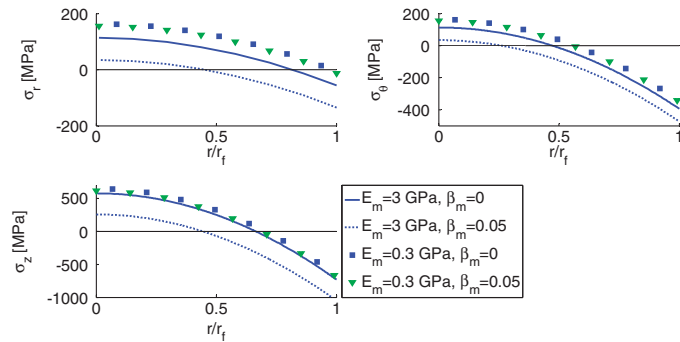


Figure 11. Stress distribution along fiber radial direction at full charge with 10C charge rate.

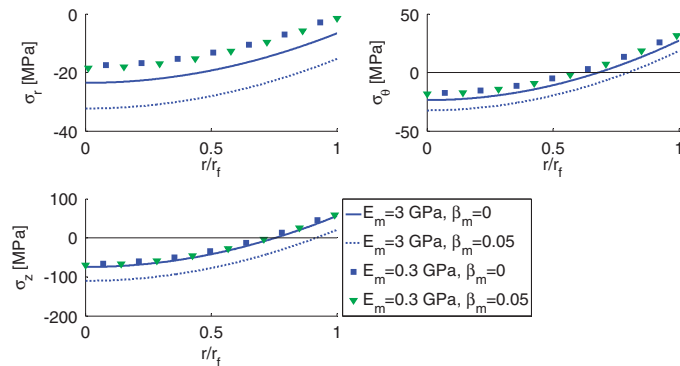


Figure 12. Stress distribution along fiber radial direction at cut-off voltage = 2.7V, with 1C discharging.

rate, when the Li transport is not sufficiently fast, higher stress gradients are expected, since they are resulting from concentration gradients. Indeed, hoop and axial stresses at the fiber center experience tensile

stresses, while the outer part of the fiber is under compressive loading. This is due to the non-uniform Li concentration distribution creating a Li-rich shell exerting additional forces on the Li-poor fiber core. This is valid

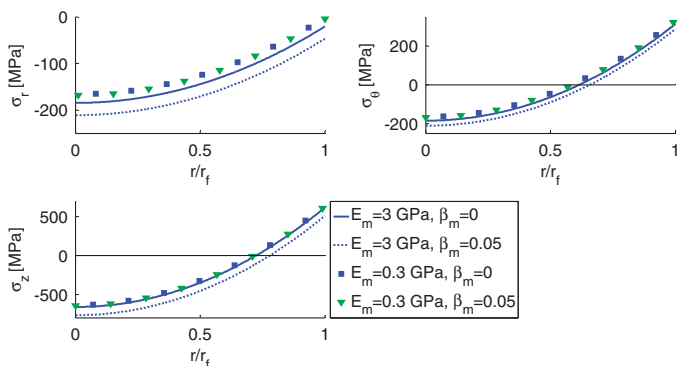


Figure 13. Stress distribution along fiber radial direction at cut-off voltage = 2.7 V, with 10 C discharging.

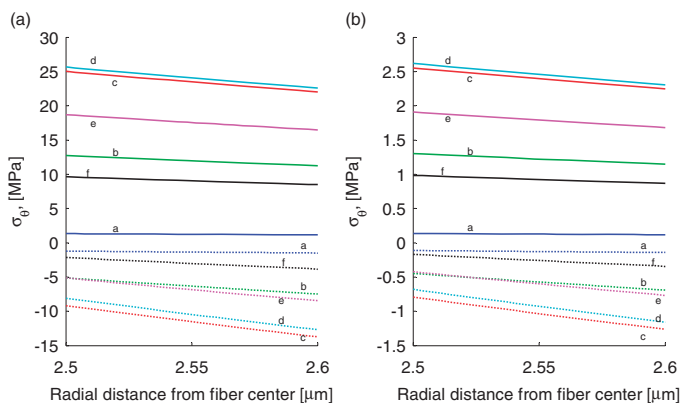


Figure 14. Hoop stress in the coating for a) high $E_m = 3$ GPa and b) low $E_m = 0.3$ GPa, with and without matrix swelling (solid resp. dashed lines), for time instances shown in Table 3.

during the entire charging. At discharge, the stress state is reversed, resulting in tensile axial and hoop stresses at the outer fiber parts, Figure 13.

At the end of the discharge with 1C-discharge rate, Figure 12, the fiber is approaching its initial delithiated stress free state, however, due to the lower cut-off voltage being conservatively set to 2.7 V, a small amount of Li remains in the carbon fiber, meaning there will be non-uniform residual swelling in the material.

From a damage and fracture mechanics point of view, tensile stresses are more critical than compressive stresses, potentially causing crack initiation and growth during cycling. For a high C-rate, there are large tensile hoop stresses present both during charging and discharging of the battery cell, meaning that if radial cracks are initiated at the surface, they may grow inside the fiber

in fatigue during both charging and discharging in repeating cycles.

Stresses in the coating. Since the task of the SPE coating in addition to transferring load is also to act as an electrical insulator preventing short-circuiting and also as an ion conductor between the fiber and matrix, it is of great importance that it is damage-free. This motivates studying stresses in the coating and at the interface. Radial stresses at the fiber/coating interface analyzed in ‘Stresses at the fiber surface’ section are compressive. Since they do not change much over the thickness of the coating, we can exclude that as a possible threat. Remaining possible damage modes are radial cracks introduced by tensile hoop stresses and cracks due to high tensile axial stress with a normal in axial direction fragmenting the coating. In Figure 14, the hoop stress

Table 4. Stresses at the coating/matrix interface and at the outer boundary at full charge for 10C charging.

E_m (GPa)	β_m (-)	σ_r ($r = r_c$) (MPa)	σ_θ ($r = r_c$) (MPa)	σ_θ ($r = r_m$) (MPa)	σ_z ($r = r_c$) (MPa)	σ_z ($r = r_m$) (MPa)
3	0.05	-129.9	281.7	148.3	215	211.5
3	0	-52.9	113.9	61.0	41.6	41.6
0.3	0.05	-13.2	28.7	15.1	29.1	21.5
0.3	0	-5.4	11.6	6.2	4.2	4.2

radial distributions during 10C charging/discharging at selected time instants detailed in Table 3 are shown.

In addition to a higher modulus in the matrix resulting in higher hoop stresses in the coating material, it can also be seen that the hoop stress in the coating material is positive for both the charge and discharge if the matrix material does not swell. In a more realistic case when the matrix material swells, the stress in the coating is negative during both charge and discharge.

This result eliminates the hoop stress as the potential cause of coating damage. However, not only mechanical stresses cause damages to the material, at an excessive reduction of the coating thickness, there is a risk of dielectric breakdown. Therefore, the changes in thickness of the coating should be reported. The reduction of coating thickness reaches 12 nm with matrix swelling and 6 nm without swelling.

The axial stress in the coating for the case of a stiff matrix with swelling reaches -36.5 MPa for charging to upper cut-off voltage and -12.2 MPa for discharging to lower cut-off voltage, with only insignificant change through the thickness of the thin coating. In the case of zero matrix swelling, the axial stress varies between -1.2 MPa (at upper cut-off) and -0.4 MPa (lower cut-off). The axial stress in the coating is compressive because radial shrinkage of the matrix leads to large compressive radial stresses and strains in the coating causing very large Poisson's effect (strain) in the axial direction - larger than the axial swelling of the composite micro-battery.

The results presented in this section show that the coating damage is not likely for matrix materials with a relatively large swelling coefficient.

Stresses in the matrix. Stresses in the matrix are greatly affected by the matrix swelling. In Table 4, the matrix stresses at the outer boundary ($r = r_m$) and at the coating/matrix interface ($r = r_c$) are shown. The radial stress at the outer boundary is zero.

The dependency of all stresses on matrix stiffness and swelling coefficient is evident. The most noticeable difference between a matrix that shrinks

during charging and the one which does not, is the enormous tensile axial stress arising in the matrix during charging, since the matrix is constrained from shrinking (it cannot shrink more than the whole micro-battery). These stresses can cause multiple matrixes cracking with cracks oriented transverse to the fiber direction.

The high tensile hoop stresses when the matrix is shrinking during charging, indicating that radial cracks at the coating-matrix interface also is a possible damage mechanism to consider.

Conclusions

Lithium diffusion in a single carbon fiber composite micro-battery was analyzed numerically by a physics-based electrochemical model. The resulting transient Li concentration distributions were used in combination with FEM-based elastic stress analysis in order to assess the mechanical stresses in the fiber, coating and matrix caused by non-uniform swelling and shrinking of the micro-battery.

The effect of the increase in the matrix stiffness alone on the free expansion of the composite unit in the axial direction is very limited. However, a higher stiffness of the matrix renders significantly lower swelling of the composite if the matrix material also changes volume during electrochemical cycling. There is a relationship between the swelling and the charging rate, since the Li content and radial distribution differ. Results show that estimations from analytical expression based on average Li concentration correspond well to swelling obtained from numerical solution.

The expansion of the composite in the radial direction may be either positive or negative, depending on the matrix material swelling character, indicating the possibility to minimize the radial swelling of the composite by optimizing the swelling of the matrix during material development.

There are two mechanisms governing the stresses, (i) the interaction with the surrounding material and (ii) the non-uniform Li concentration distribution in the fiber, the latter is dominant for a fast charge rate.

The fiber boundary is under radial compression during both charging and discharging, regardless of matrix stiffness and with or without matrix swelling, whereas the hoop and axial stresses are negative only during charging and switch to positive during discharging. Radial cracks in the fiber may be initiated in this region. Matrix shrinkage delays damage initiation in the fiber at the interface and makes the coating damage unlikely.

Due to matrix shrinkage, large tensile hoop and axial stresses develop in the matrix, which may lead to matrix failure.

Acknowledgment

The authors would like to acknowledge KOMBATT-II project members for fruitful discussions.

Declaration of Conflicting Interests

The author(s) declared no potential conflicts of interest with respect to the research, authorship, and/or publication of this article

Funding

The author(s) disclosed receipt of the following financial support for the research, authorship, and/or publication of this article: The Swedish Energy Agency, project 37712-1 is acknowledged for financial support.

References

- Gibson RF. A review of recent research on mechanics of multifunctional composite materials and structures. *Compos Struct* 2010; 92: 2793–2810.
- Greenhalgh ES, Ankersen J, Asp LE, et al. Mechanical, electrical and microstructural characterisation of multifunctional structural power composites. *J Compos Mater* 2015; 49: 1823–1834.
- Shirshova N, Qian H, Shaffer MSP, et al. Structural composite supercapacitors. *Compos Part A* 2013; 46: 96–107.
- Ekstedt S, Wysocki M and Asp LE. Structural batteries made from fibre reinforced composites. *Plast Rubber Compos* 2010; 39: 148–150.
- Asp LE and Greenhalgh ES. Structural power composites. *Compos Sci Technol* 2014; 101: 41–61.
- Linden D and Reddy TB. *Handbook of batteries*. New York: McGraw-Hill, 2002.
- Hamann CH, Hamnett A and Vielstich W. *Electrochemistry*. Weinheim: Wiley-VCH, 2007.
- Sun B, Mindemark J, Edström K, et al. Realization of high performance polycarbonate-based Li polymer batteries. *Electrochem Commun* 2015; 52: 71–74.
- Willgert M, Kjell MH, Lindbergh G, et al. New structural lithium battery electrolytes using thiol-ene chemistry. *Solid State Ionics* 2013; 236: 22–29.
- Willgert M, Leijonmarck S, Lindbergh G, et al. Cellulose nanofibril reinforced composite electrolytes for lithium ion battery applications. *J Mater Chem A* 2014; 2: 13556–13564.
- Yue L, Ma J, Zhang J, et al. All solid-state polymer electrolytes for high-performance lithium ion batteries. *Energy Storage Mater* 2016; 5: 139–164.
- Leijonmarck S, Carlson T, Lindbergh G, et al. Solid polymer electrolyte-coated carbon fibres for structural and novel micro batteries. *Compos Sci Technol* 2013; 89: 149–157.
- Buqa H, Goers D, Holzapfel M, et al. High rate capability of graphite negative electrodes for lithium-ion batteries. *J Electrochem Soc* 2005; 152: A474–A481.
- Pupurs A and Varna J. Modeling mechanical stress and exfoliation damage in carbon fiber electrodes subjected to cyclic intercalation/deintercalation of lithium ions. *Compos Part B* 2014; 65: 69–79.
- Cheng Y and Verbrugge MW. Diffusion-induced stress, interfacial charge transfer, and criteria for avoiding crack initiation of electrode particles. *J Electrochem Soc* 2010; 157: A508–A516.
- Hagberg J, Leijonmarck S and Lindbergh G. High precision coulometry of commercial PAN-based carbon fibers as electrodes in structural batteries. *J Electrochem Soc* 2016; 163: A1790–A1797.
- Kjell MH, Jacques E, Zenkert D, et al. PAN-based carbon fiber negative electrodes for structural lithium-ion batteries. *J Electrochem Soc* 2011; 158: A1455–A1460.
- Jacques E, Hellqvist Kjell M, Zenkert D, et al. Expansion of carbon fibres induced by lithium intercalation for structural electrode applications. *Carbon* 2013; 59: 246–254.
- Bard AJ and Faulkner LR. *Electrochemical methods: fundamentals and applications*. New York: Wiley, 2001.
- Nyman A, Behm M and Lindbergh G. A theoretical and experimental study of the mass transport in gel electrolytes II. Experimental characterization of LiPF₆-EC-PC-P(VdF-HFP). *J Electrochem Soc* 2011; 158: A636–A643.
- Xu J, Varna J and Lindbergh G. Multiphysics modeling of mechanical and electrochemical phenomena in structural single fiber micro-battery. Submitted to Smart Materials and Structures.
- COMSOL Multiphysics® v. 5.2. www.comsol.com. COMSOL AB, Stockholm, Sweden, 2016.
- Kjell MH, Zavalis TG, Behm M, et al. Electrochemical characterization of lithium intercalation processes of PAN-based carbon fibers in a microelectrode system. *J Electrochem Soc* 2013; 160: A1473–A1481.
- Zavalis TG, Klett M, Kjell MH, et al. Aging in lithium-ion batteries: model and experimental investigation of harvested LiFePO₄ and mesocarbon microbead graphite electrodes. *Electrochim Acta* 2013; 110: 335–348.
- Vazquez-Arenas J, Gimenez LE, Fowler M, et al. A rapid estimation and sensitivity analysis of parameters describing the behavior of commercial Li-ion batteries including thermal analysis. *Energy Convers Manage* 2014; 87: 472–482.

Paper III

Matrix and interface microcracking in carbon fiber/polymer structural micro-battery

Johanna Xu, Janis Varna

Department of Engineering Sciences and Mathematics, Luleå University of Technology SE-97187 Luleå, Sweden

ABSTRACT

In this paper propagation of radial matrix cracks and debonds at the coating/matrix interface in unidirectional (UD) carbon fiber structural micro-battery composite are studied numerically. The micro-battery consists of a solid electrolyte coated carbon fiber embedded in an electrochemically active polymer matrix. Stress analysis shows that high hoop stress in the matrix during charging may initiate radial matrix cracks at the coating/matrix interface. Several 2-D finite element models of the transverse plane with different arrangements of fibers and other matrix cracks were used to analyze the radial matrix crack growth from the coating/matrix interface of the central fiber in a composite with a square packing of fibers. Energy release rates (ERR) of radial cracks along two potential propagation paths are calculated under pure electrochemical loading. The presence of a radial matrix crack imposes changes in the stress distribution along the coating/matrix interface, making debonding relevant for consideration. Results for ERR show that the debond crack growth is governed by Mode II.

1. INTRODUCTION

In a conventional fiber reinforced polymer (FRP) composite laminate, cracking within plies, often referred to as matrix cracking or transverse cracking is a well-studied phenomenon [1]. This failure mode, which is caused by the combined action of in-plane tensile transverse and shear stresses in the ply, is the first to occur under tensile loading of the laminate. By itself, it leads to laminate thermo-elastic properties reduction, but the performance reduction is not necessarily significant. However, other failure modes can be initiated through the presence of matrix cracks, such as interlayer delaminations and fiber failures in neighboring layers, which

certainly have detrimental effects on the load bearing capability of the laminate.

The initiation of these ply-scale cracks is a sequence of phenomena on the fiber/matrix scale. In polymeric composites under mechanical and thermal loads it usually starts with fiber/matrix interface crack (debond) initiation and growth (because of large tensile radial and shear stresses at the interface). When the load increases these debonds deviate from the interface to link by building a ply-scale crack. Mechanics of these processes has been studied on many models of varying degree of complexity. Most often the analysis is based on energy release rate (ERR) calculations based on linear elastic fracture mechanics (LEFM) [2-5] or sometimes using cohesive elements at the interface [6-8]. The basics of the debond growth were understood in studies of a single fiber embedded in an infinite matrix [5,9,10] finding that there is an opening in a certain part of the interface crack while a relatively large part at the crack tip is in contact with sliding. So, with increasing debond arc length the crack propagation changes from predominantly Mode I to mixed mode and finally the growth is in a pure Mode II. The effect of the position of the neighboring fiber was studied in [11] considering a two fiber system embedded in an infinite matrix. In [12] the effect of a local hexagonal cluster with high local fiber content and with the partially deboned fiber in the middle was studied embedding this cluster in a homogenized composite material. Among other studies we can mention [13] where the debond growth in a local cluster and its deviation from the interface were analyzed assuming that the neighboring fiber also has a debond of a certain size.

In all these studies the fiber/matrix debonding is the first phenomenon and the crack can (or may be it cannot) deviate in the matrix. Thermal shrinkage of the matrix material during the cool-down after curing adds some compressive radial stresses at the interface which are expected to improve the interface resistance to debonding in Mode I. When performing FEM studies on carbon fiber/epoxy unidirectional (UD) composites subjected to 0.5% transverse strain it was shown that the Mode I ERR decreases by about 20% whereas the Mode II ERR

remained almost unchanged [14]. These microscale effects were “overshadowed” by thermal stresses on the ply scale for cases when the layer is a part of a multi-directional laminate. For example, the ply scale thermal transverse stresses in a cross-ply laminate almost triple the Mode I and the Mode II ERR comparing with the values in a stand-alone UD composite layer at the same 0.5% applied strain.

In addition, due to larger thermal expansion coefficient of the matrix, tensile hoop stresses at the interface rise in the matrix during the cool-down. Potentially these stresses could cause radial micro-crack formation at the interface. However, this stress component in polymeric composites is relatively small and the radial micro-crack scenario has not been addressed seriously in the literature.

However, there is another shrinkage mechanism in polymers taking place during cross-linking; chemical shrinkage. For epoxy resins the volumetric chemical shrinkage is less than 5% but for unsaturated polyester (UP) it can reach 10%. The residual stresses related to this phenomenon were analyzed in [15-17] finding that the hoop stresses may be large and lead to matrix crack initiation without debonding before that.

In the current paper we analyze a different physical phenomenon which also results in large swelling and shrinking strains not only in the matrix but also in the fiber. The material is structural UD composite battery and the shrinking and swelling is caused by electrochemical reactions resulting in diffusion of ions into the carbon fiber during charging and back into the matrix during discharging.

Structural batteries is a concept aiming to combine two functionalities into one material; mechanical load carrying and electrical energy delivering capabilities. The concept can be realized by utilizing the lithium-ion battery (LIB) technology, using carbon fibers as a) an active electrode material (host material for lithium intercalation/deintercalation: the reversible insertion and extraction of ions into materials structures) and b) as a high strength and stiffness

reinforcement in a polymeric composite material. The achieved synergetic multifunctionality has the potential to enable vast mass and volume savings in the transportation sector in particular [18].

One of many possible concepts for implementing structural composite batteries is through the so called micro-battery design, with single carbon fibers acting as negative electrodes. Each carbon fiber is individually coated with a thin layer of a solid battery electrolyte (SBE) surrounded by a matrix material acting as a positive electrode [18].

Volume changes in the intercalated carbon fibers were studied experimentally [19], measuring a longitudinal expansion of 1% and an approximately 5% radial expansion. The active material in the positive electrode (matrix) is also swelling/shrinking upon lithiation/delithiation [20].

The arising stresses during the charging and discharging can be so high that microcracks may initiate and grow without any applied external load [21]. Particularly, the hoop stresses close to the fiber surface are so high that radial crack formation is one of the most probable micro-damage modes. This microdamage mode with a possible extension to create interface cracks is analyzed in the present paper.

A simplified modelling strategy for analyzing the initiation and propagation of possible damage mechanisms in the micro-battery is presented based on analysis of ion distribution and stress changes during intercalation/deintercalation. The static elasticity problem is solved and the ERR is calculated at time instant corresponding to the worst case, corresponding to fully charged battery. Radial matrix microcracks, which are assumed not to affect radial diffusion in the battery, were introduced and trends in their growth were analyzed using the virtual crack closure technique (VCCT) [22], well known in LEFM. Conditions for interface crack initiation at the radial crack tip are also analyzed.

2. STRUCTURAL MICRO-BATTERY

Conventional LIB cells have three main constituents, a cathode (positive electrode), an electrically insulating separator, and an anode (negative electrode), stacked in layered structure and immersed in an ionically conductive liquid electrolyte. During operation, oxidation takes place at one electrode, releasing electrons to an external circuit via the current collector and lithium ions to the electrolyte, and reduction at the other electrode where lithium ions and electrons are collected [23].

Structural batteries have not yet progressed far enough for implementation and much more research is required – a comprehensive review of the subject area is carried out in [18].

In the so called micro-battery a single carbon fiber acts as a negative electrode. Each carbon fiber is individually coated with a thin (a few hundred nanometers thick) layer of solid battery electrolyte (SBE) surrounded by a matrix material mixed with intercalation compounds acting as a positive electrode, Figure 1.

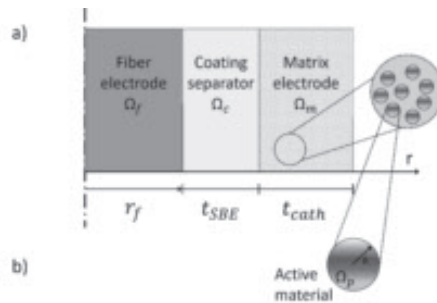


Figure 1. Schematic of the computational domains in micro-battery. a) on the largest scale the micro-battery is divided in three domains, Ω_f , Ω_c and Ω_m . Two phases are present in the matrix domain: the electrolyte mixture phase homogenized with respect to porosity and the solid active material phase. b) The matrix (positive electrode) is porous, with spherical active material particles.

The multi-scale physics-based electrochemical model to describe the micro-battery contains a coupled system of 11 nonlinear partial differential equations (PDEs), solved in COMSOL Multiphysics [24], following the mathematical methodology developed by Newman et al [25,26]. The PDEs describe the spatial and time dependent variation in lithium ion

concentration in the matrix and in the fiber, see more details in Appendix 1.

Conventional LIB are manufactured with the negative electrode (anode) capable of accommodating more charge than can be stored in the positive electrode (cathode) [27]. For a structural micro-battery this means that the capacity for Li intercalation in the matrix has to be balanced with Li intercalation capacity in the fiber. There is no advantage of storing more ions in the matrix than can be transferred and inserted in the fiber, since it is associated with safety issues which ultimately leads to battery failure [28]. On the other hand, if the storage capacity in the matrix is too small, the fiber's ability to intercalate is not fully utilized. An important parameter in the following analysis is the capacity ratio of the positive to negative electrode, $R_{P/N}$, see Appendix 2 for details. A consequence of improper $R_{P/N}$ is lithium plating and dendrite formation during charging process, which in turn results in irreversible capacity loss, extensive mechanical swelling and potentially internal short circuit within the battery cell [29]. In order to avoid this type of damage, whilst optimizing the battery performance, electrodes have to be designed to hold $R_{P/N}$ as close as possible but less than 1 (i.e. with over-dimensioned negative electrode). In Figure 2 the relation between V_f and capacity ratio $R_{P/N}$ is shown, with input data from [30], including non-feasible micro-battery designs with $R_{P/N} > 1$. In this present study, as well as previous studies [21,30] $R_{P/N} = 0.92$ is used. It is referred to as the "reference case" with corresponding $V_f = 0.338$, highlighted in Figure 2.

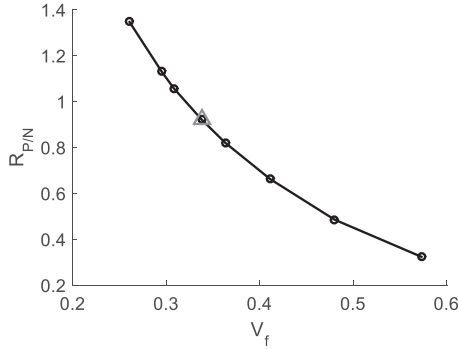


Figure 2. $R_{P/N}$ as a function of V_f , with the “reference case” highlighted.

3. ELASTIC PROPERTIES OF MATERIALS

The micro-battery is a multiscale composite material: it is a UD coated fiber composite with the matrix by itself being a spherical particle reinforced composite. In this section we present material laws for constituents and expressions for calculating the homogenized properties of the matrix.

3.1 MATERIAL MODELS FOR CONSTITUENTS

The dimensional changes and internal stresses in the constituents of the composite are due to mismatch and anisotropy of expansion coefficients, and local concentration changes of Li in active species in the composite. The dimensional changes are not free expansion of constituents but rather a result of interaction with mechanical constrains from other parts of the structural battery.

The stress-strain relationship for a transversely isotropic material with intercalation induced volumetric changes can be introduced using the thermo-mechanical analogy [31], assuming that the dimensional changes are proportional to the Li concentration, c .

$$\sigma_i^k = C_{ij}^k (\varepsilon_j^k - \varepsilon_j^{k,free\ swelling}) \quad (1)$$

For the cylindrical unit cell index $k = m$ is for the matrix, $k = c$ for the coating, and $k = f$ for the fiber, and indices $i, j = r, \theta, 1$ are cylindrical coordinates. For the spherical unit cell

representing the matrix, the upper index is for the particle and the surrounding slurry and the lower index for spherical coordinates. Repeating indexes in Eq. (1) denote summation. C_{ij}^k is the stiffness matrix using Voigt notation, $\varepsilon_j^{k,free\ swelling}$ is the free swelling strain in j -direction due to Li-ion intercalation; swelling does not have shear components. For fiber $\varepsilon_j^{f,free\ swelling} = \beta_j^f \frac{c_f}{c_{s,max}^-}$, where β_j^f are constant coefficients of proportionality called intercalation-expansion coefficients to characterize the dimensional changes in the three directions. $\frac{c_f}{c_{s,max}^-}$ is the normalized Li concentration in the fiber, where c_f is the time dependent Li concentration in the electrode material, $c_{s,max}^-$ is the maximum concentration reached when Li has intercalated into all available sites. The free swelling strain $\varepsilon^{m,free\ swelling}$ of the matrix is analyzed in *Section 3.2*.

3.2 MATRIX MATERIAL – SPHERICAL PARTICLE COMPOSITE

The matrix material is a particle composite with isotropic effective properties. The micromechanical model used to obtain effective properties of the matrix uses the composite spheres assemblage (CSA) introduced by Hashin [32], assuming two phases present. The spherical LiFePO_4 active material represents the particle phase, and the remaining constituents (SBE, carbon black and additional binder material) together comprise the so called slurry phase, shown schematically in Figure 3

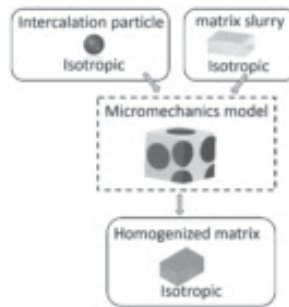


Figure 3. Modeling scheme for effective matrix elastic properties.

In the CSA the bulk modulus K given by

$$K^* = K_s + (K_p - K_s) \frac{(3K_s + 4G_s)V_p}{3K_p + 4G_s - 3(K_p - K_s)V_p} \quad (2)$$

with superscript * denoting the effective property of the particle composite and subscript s and p denotes slurry and particle phases, respectively. V is the volume fraction, and G is the shear modulus for each phase calculated by Eq. (3), where E is the Young's modulus and ν is the Poisson's ratio

$$G = \frac{E}{2(1 + \nu)} \quad (3)$$

The shear modulus for the particle composite, G^* , is then given by

$$G^* = G_s + \frac{V_p}{1/(G_p - G_s) + 6V_p(K_p + 2G_s)/5G_s(3K_s + 4G_s)} \quad (4)$$

Since the matrix material is regarded macroscopically isotropic, Young's modulus, E^* , can be calculated from the bulk and shear modulus as

$$E^* = \frac{9K^*G^*}{3K^* + G^*} \quad (5)$$

The free swelling strain of the homogenized matrix, assuming $\beta_s = 0$, is given by

$$\varepsilon^{m,f \text{ free swelling}} = \beta_p V_p \left(1 - \frac{4(K_p - K_s)G_s V_s}{3K_s K_p + 4G_s(K_s V_s + K_p V_p)} \right) \frac{c_p}{c_{p,max}} \quad (6)$$

where $\frac{c_p}{c_{p,max}}$ is the normalized Li concentration in the LiFePO_4 particle, calculated from the electrochemical model, Appendix 1.

In this study, the volume fraction of the active material is $V_p = 0.553$, the isotropic constituent material properties of the particle composite are presented in Table 1. The elastic properties of the fiber and SBE coating are shown in Table 2.

Table 1. Elastic properties of the constituents of the matrix.

Constituent	E (GPa)	ν (-)	β (-)
LiFePO_4	125	0.28	0.07
Slurry	1	0.3	0

Table 2. Elastic constants and swelling parameters of the composite constituents for reference case.

Constituent	E_z	E_r	ν_{zr}	$\nu_{r\theta}$	Expansion	
	(GPa)	(GPa)	(-)	(-)	$\beta_z(-)$	$\beta_r(-)$
Matrix	2.5	2.5	0.3	0.3	0.04	0.04
SBE coating	1	1	0.3	0.3	0	0
Fiber	300	30	0.2	0.45	0.009	0.05

4. STRESS DISTRIBUTION IN UNDAMAGED COMPOSITE

4.1 UNIT CELL WITH AXIAL SYMMETRY

In [21] the transient lithium ion diffusion in the carbon fiber and the arising stresses were studied numerically using an axisymmetric unit cell representation of the UD composite. It was concluded that the two mechanisms governing the stresses in the fiber are a) the interaction with the surrounding material and b) the non-uniform Li concentration distribution in the fiber, which is only dominant for a fast charge rate. However, in reality such fast charge rates are not likely.

The intercalation expansion induced stresses in a transversely isotropic active materials can be considered through a thermo-mechanical analogy [30,31,33] using the material model described in *Section 3.1*. In the micro-battery cell model described as an axisymmetric problem in Figure 1, an infinite long fiber is assumed. All shear stress components are equal to zero and the only non-trivial equilibrium equation is

$$\frac{\partial \sigma_r^k}{\partial r} + \frac{\sigma_r^k - \sigma_\theta^k}{r} = 0 \quad (7)$$

where σ_i^k are stress components in cylindrical coordinate system.

Figure 4a show the Li concentration in the fiber (to the left in graph) and matrix (to the right in graph) during charge, for four time instants evenly distributed throughout the charge of one hour (1C charge rate). The battery is fully charged when all Li initially stored in the matrix active material has been intercalated into the fiber. Figure 4b show the corresponding Li

distribution during discharge. The difference in Li concentration at the center of the fiber ($r = 0$) and the fiber surface ($r = 2.5\mu\text{m}$) is negligible during both charging and discharging. In the matrix the difference in Li concentration between the coating/matrix interface ($r = r_c$) and the matrix outer surface ($r = r_m$) is evident. At the beginning of charging all available Li is stored in the active material of the matrix. As the charging progresses via electrochemical reactions Li-ions are transported to the fiber via the SBE coating, starting at the coating/matrix interface. The concentration gradient arise due to low ionic conductivity in the matrix, with the concentration at the coating/matrix constantly lower than the outer surface, although the difference decreases closer to full charge, and at full charge there is no difference. At discharging the reverse applies, although due to the discharging being disrupted at a so called cut-off voltage the concentration distribution never fully levels out.

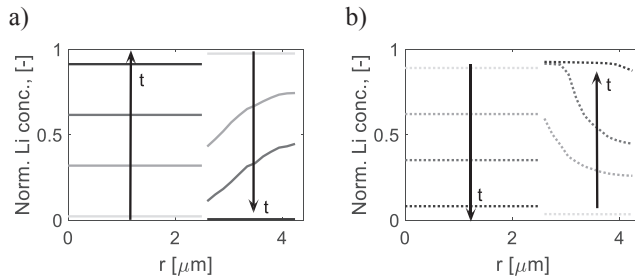


Figure 4. a) Li distribution in micro-battery during charge, curves on the left represent Li concentration in the fiber and on the right the Li concentration in the matrix. b) Li distribution in micro-battery during discharge, curves on the left represent Li concentration in the fiber and on the right the Li concentration in the matrix.

The initial state corresponding to completely delithiated fiber and fully lithiated matrix is assumed stress-free. As shown in Figure 5a and Figure 6a, the radial stresses at the fiber boundary are compressive during both charging and discharging, meaning that debonding between fiber and coating is not likely to occur without applying external constraints.

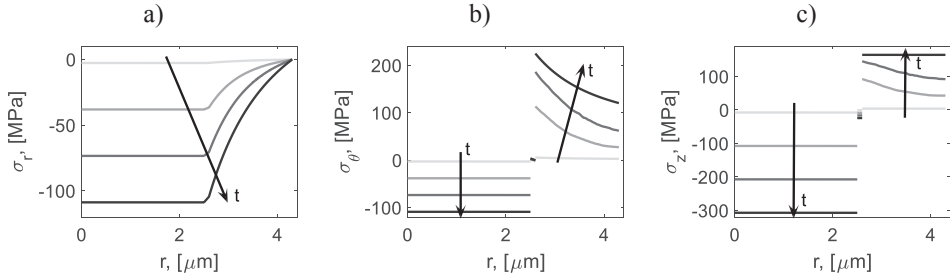


Figure 5. Stress distribution during charging. a) radial stress. b) hoop stress. c) axial stress

Due to matrix axial shrinkage and fiber swelling, large tensile axial stresses develop in the matrix during charging, Figure 5c, which may lead to multiple matrix fragmentation with crack plane transverse to the fiber direction. However, since the axial stress is rather uniform in the matrix at full charge, implying unstable crack propagation with initiation anywhere, fracture mechanics analysis of this failure mode is not feasible. The high tensile hoop stresses built up during charging, Figure 5b, indicate that radial cracks at the coating-matrix interface are a possible damage mechanism to consider. Radial cracks are of particular interest because they may contribute to debonding phenomena under mechanical transverse loading, which in this structural composite battery material would lead to impaired electrochemical performance as well, since transport mechanisms (diffusion and migration) are hindered. Having radial cracks present before the application of transverse tensile loading may change the matrix/interface failure evolution.

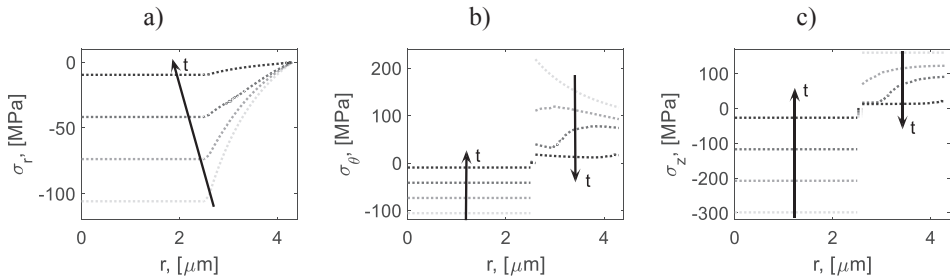


Figure 6. Stress distribution during discharging. a) radial stress. b) hoop stress. c) axial stress

In Figure 4a (solid black line) it can be seen that the Li distributions in both fiber and matrix are uniform at instant of full charge. Furthermore, Figure 5-Figure 6 show that all stresses are the highest at full charge, making this time instant the most dangerous from a damage point of view. Therefore, when studying microcracking we can focus on uniform Li distribution corresponding to the fully intercalated fiber with uniform Li distribution. The stresses in other instants are lower. Due to this feature, the computational time can be reduced significantly assuming perfectly uniform distribution. In Figure 7 the accuracy of the uniform concentration distribution assumption is demonstrated, the hoop stress distribution obtained from the transient (electrochemical) model in the instant when the fiber is fully charged is plotted together with the stress from the model with assumed uniform Li distribution in the fiber, and near zero uniform distribution in the matrix. The two curves in the graph correspond very well, with less than 0.1% difference.

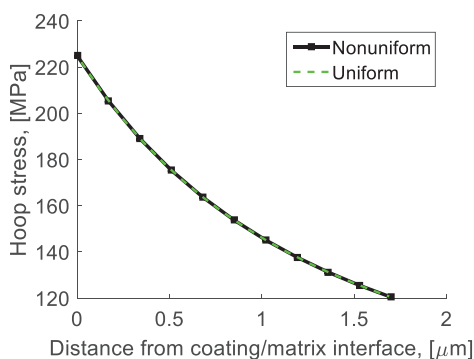


Figure 7. Hoop stress distribution along matrix radial direction; from coating/matrix interface to matrix outer boundary. In “Nonuniform” the Li distribution is from the electrochemical model corresponding to a fully charged state, in “Uniform” the Li distribution is assumed uniform.

It can be seen in Figure 7 that the hoop stress is high comparing with typical tensile strength values for polymers, which is due to very large shrinkage in matrix and expansion in fibers. The mismatch in volume change in both main constituents is similar to that of the chemical shrinkage of the UP matrix discussed in the *Introduction*. Similarly as studying cure shrinkage

of the UP, where hoop stresses may be large and lead to matrix crack initiation without prior debonding, radial matrix crack caused by Li intercalation is a phenomenon of interest to this study.

4.2 MULTIFIBER MODELS WITH SQUARE PACKING

When a model with multiple fibers is analyzed or when a radial crack parting from the coating/matrix interface is the subject of interest, the axial symmetry of the problem is lost. Therefore, a 2-D transversal representation of the problem in generalized plane strain formulation is discussed in the following. Square packing of 9 fibers is shown in Figure 8, with coordinate systems $x - y$ and $x' - y'$ shown for the so called “central fiber”. The interfiber distances, l_{ID} , between the central fiber and the neighboring fibers for the reference case are listed in Table 3.

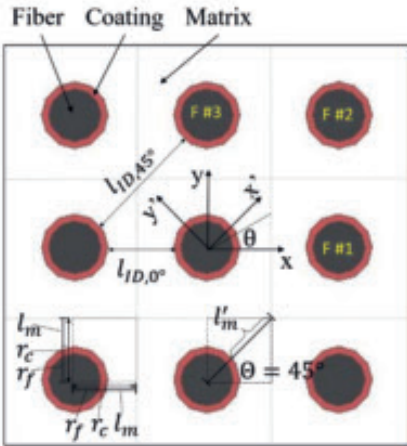


Figure 8. Square packing of 9 fibers.

Table 3. Geometrical parameters of the unit cell for the reference case, Figure 8

Parameter	Value [μm]
r_f	2.5
r_c	0.1
l_m	1.2
$l_{ID,0^\circ}$	2.4
$l_{ID,45^\circ}$	5.6

Analysis of the local stresses in the composite micro-battery under electrochemical loading was conducted using commercial finite element (FE) software ANSYS APDL[®]. Eight-node “PLANE183” quadrilateral elements were used, with generalized plane strain behavior. Displacement coupling conditions were applied to outer boundary of the unit cell to reflect the repeatability of the microstructure. With the assumed uniform Li concentration distribution in the fiber with $c_{f,max} = R_{P/N}$ and no Li in the matrix, the stress distribution with respect to the two potential (in this section cracks are not introduced) crack growth paths ($\theta = 0^\circ$ and $\theta = 45^\circ$ directions) denoted as x and x' is shown in Figure 9a. The hoop stress along the coating/matrix interface of the central fiber is not constant, with a slightly higher stress at $\theta = 0^\circ$, meaning that most probably the crack will be initiated there, growing towards the nearest adjacent fiber. The hoop stress value at the interface at $\theta = 0^\circ$ is slightly higher than in the CCA model and very similar to CCA, when $\theta = 45^\circ$, see Figure 7.

Figure 9a shows large difference in the normal stress σ_y and $\sigma_{y'}$ distribution along the x and x' path respectively. The minimum stress value that occurs in the middle between two fibers is much higher than the $\sigma_{x'}$ value at $x'/l_{ID,45^\circ} = 0.5$. The main reason for higher stresses along the x -paths is the shorter inter-fiber distance: since fiber F#1 is closer to the central fiber than F#2, there is less distance for stress reduction. Another difference is presence of F#3 and F#1 fibers, Figure 8, which are close to the considered x' -path and may affect the stress distribution.

There are no such close fibers in the vicinity of the x -path. To analyze the possible effect of these fibers on the stress field, a square packing model with lower $V_f=0.17$ was introduced where l_m is equal to l'_m used in the previous model with $V_f = 0.338$. In Figure 9b the σ_y distribution for this case is shown together with the $\sigma_{y'}$ distribution along x' for $V_f = 0.338$. In both cases, the same Li distribution was assumed in both the fiber and the matrix. It can be seen, comparing curves in Figure 9b, that the stress at the coating/matrix interface decreases when lowering the V_f . Further, the σ_y stress in Figure 9b is larger than $\sigma_{y'}$, proving that the presence of F#1 and F#3 on both sides of the x' -path has a shielding effect.

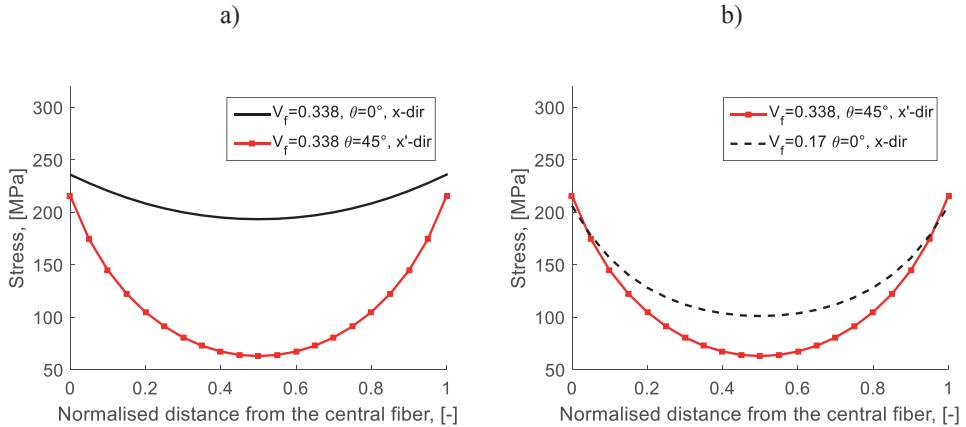


Figure 9. σ_y and $\sigma_{y'}$ distribution between the central fiber and fibers F#1 and F#2, respectively, without damage, for a) $V_f = 0.338$; b) σ_y for $V_f = 0.17$ and $\sigma_{y'}$ for $V_f = 0.338$

4.3 EFFECT OF CURING TEMPERATURE

In Section 4.2 the stresses possibly leading to matrix cracks were investigated as caused by pure electrochemical loading. It is of interest to investigate the influence of stresses arising as a result of manufacturing features. In the initial stage of SBE development UV-curing was used [34,35]. However, due to practical limitations such as carbon fiber in itself being black, UV cure of an entire laminate is impossible and it is inevitable to switch to heat curing. In heat curing, the

cool-down of the laminate from the curing temperature causes local thermal stresses. Figure 10 show distribution of σ_y and $\sigma_{y'}$, stress in the matrix, with and without thermal effects generated by the cool-down temperature difference $\Delta = -80^\circ\text{C}$. The temperature change was applied uniformly to the model before applying intercalation loading. However, the thermal stress contribution is small, as shown in Figure 10 and not included in the calculations of the strain energy release rate presented in the following sections.

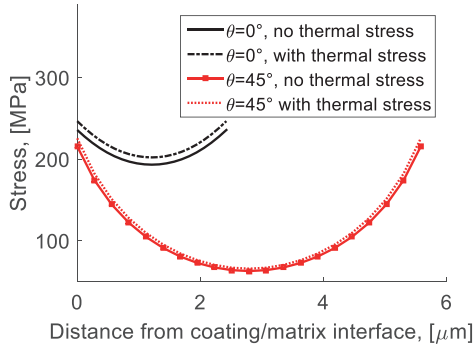


Figure 10. σ_y and $\sigma_{y'}$, distribution between fibers with and without thermal stress.

5. MULTIFIBER MODELS WITH MATRIX CRACK

Based on results presented in *Section 4* we expect that the first mode of damage will be formation of radial cracks near the coating/matrix interface due to high tensile hoop stresses arising during intercalation. Since the ion transport in the battery is in the radial direction, the Li distribution is not affected by the presence of any radial cracks.

In the models shown in Figure 11, symmetry conditions were assigned to $y = 0$ and $y' = 0$, respectively, depending on the assumed crack growth direction. All remaining outer boundaries are assigned with coupling boundary conditions to represent a repeating unit in a UD composite. In all models one radial crack, L_r , was introduced at the coating/matrix interface at either $x = r_f + r_c$ or $x' = r_f + r_c$, Figure 8. Appropriate mesh refinement was used in the vicinity

of the crack tip, Figure 12, where uniform quadrilateral elements were generated ahead of and behind the crack tip.


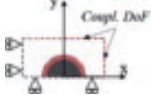

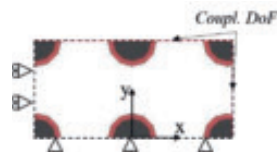
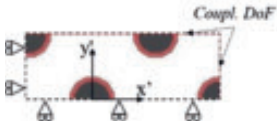
Model geometry and boundary conditions	Description	Designation
	One crack growing towards free surface	CCA
	One $\theta = 0^\circ$ crack towards oncoming crack tip in the opposite propagation direction	$\theta = 0^\circ$, 1 CF
	$\theta = 0^\circ$ crack in every layer, growing towards neighboring fiber in x-dir.	$\theta = 0^\circ$, 3 CF
	$\theta = 0^\circ$ crack in every 2 nd layer, growing towards neighboring fiber in x-dir.	$\theta = 0^\circ$, 9 CF
	$\theta = 45^\circ$ crack in every 2 nd layer, growing towards neighboring fiber in x'-dir.	$\theta = 45^\circ$, 6 CF

Figure 11. Model geometry and boundary conditions for cracking analysis in UD micro-battery composite material .

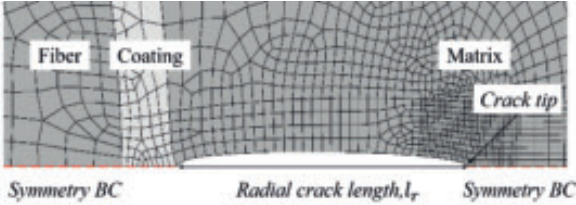


Figure 12. FE model for calculating radial crack growth related energy release rate; deformed FE mesh near the crack tip.

5.2 ENERGY RELEASE RATE FOR MATRIX CRACK PROPAGATION

In Figure 13 the Mode I ERR, G_I [J/m^2] at the instant when the fiber is fully intercalated is shown as a function of normalized radial crack length, $l_{r,n} = l_r/l_{ID,0^\circ}$. l_r is the length of the matrix crack.

In multifiber units containing 3 and 9 fibers the ERR of a crack propagating towards F#1 is proportional to the crack length, as typical for cracks in an infinite medium. May be an insignificant shielding effect can be noticed from the fiber in front of the central, slightly slowing down the ERR increase. For the CCA unit the linearity is lost when the crack approaches the free surface that facilitates its growth. It is obvious that boundary conditions in the concentric cylinder model with one radial crack and free boundary do not apply to a composite material, where the micro-battery units are surrounded and affected by the rest of the material.

For the “ $\theta = 0^\circ, 1 CF$ ”-model, one crack approaching to the boundary means that two cracks are growing towards each other. For small crack lengths there is no difference in ERR with other models. At normalized crack lengths > 0.35 when the crack tip is interacting with the oncoming crack, the available energy increases rapidly, although less than for the CCA case.

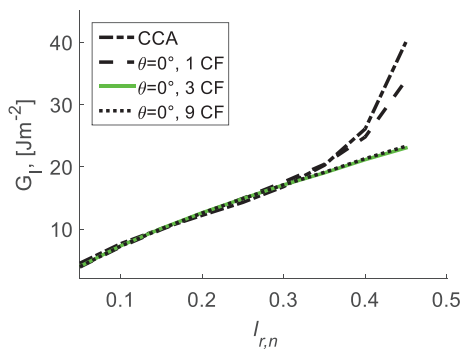


Figure 13. Variation of ERR as a function of normalized radial crack length $l_{r,n} = l_r/l_{ID,0^\circ}$, for the reference case $V_f=0.338$, with different boundary conditions.

The “ $\theta = 0^\circ, 3 CF$ ” model is a repeating element in the y -direction, which means that it represents a composite that is a stack of thin layers of thickness $h = r_f + r_c + l_m$. Each layer in this model contains only one fiber in the thickness direction and the central fiber has a radial matrix crack in the x -direction. Parallel cracks in neighboring layers in the “ $\theta = 0^\circ, 3 CF$ ” model could shield each other, reducing the ERR. In the “ $\theta = 0^\circ, 9 CF$ ”-model we have three layers of thickness h and only the central layer has a crack (the surrounding two layers of thickness h do not have cracks). Certainly, due to coupling conditions, the following layer also contains a central fiber with a radial crack in the x -direction, but this layer with a crack is rather far away from the investigated crack. If there is an interaction (shielding) between these parallel cracks it should be more pronounced in the “ $\theta = 0^\circ, 3 CF$ ”-model. However, in Figure 13 the G_I shows no difference, this means that the interaction of these cracks is negligible.

In Figure 14 G_I is shown for crack growth in $\theta = 0^\circ$ and $\theta = 45^\circ$ directions towards fibers F#1 and F#2, respectively, (Figure 8), according to the “ $\theta = 0^\circ, 9 CF$ ”-model and the “ $\theta = 45^\circ, 6 CF$ ”-model, models which we consider as the most adequate for the problem. Based on the above presented conclusion of the negligible shielding effect, we assume that the “ $\theta = 45^\circ, 6 CF$ ”-model ERR results are not affected by the crack in the next repeating element.

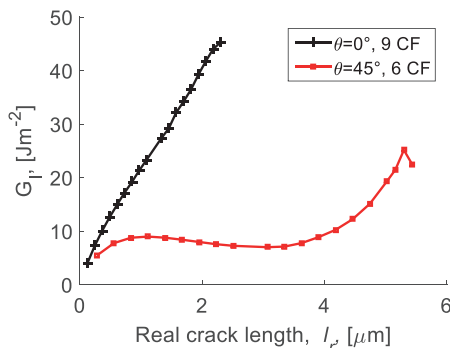


Figure 14. Variation of ERR as a function of the radial crack length for crack growth in different directions, for the reference case $V_f=0.338$.

The difference in behavior for the two directions of crack growth is mainly due to the large differences in stress distribution in the matrix in the undamaged state, Figure 9a. In the $\theta = 0^\circ$ direction where the interfiber distance is significantly shorter than for $\theta = 45^\circ$, σ_y is significantly higher than $\sigma_{y'}$, and the ERR is larger. Further, Figure 14 shows that the crack growth in $\theta = 0^\circ$ direction is unstable regardless of the crack length. For $\theta = 45^\circ$ direction crack there exists a local maximum and minimum of ERR. The local maximum at approximately $l_r = 1\mu\text{m}$ is associated with a following stable crack growth region whereas after the local minimum at approximately $l_r = 3.5\mu\text{m}$ the growth is unstable, until the crack reaches the coating/matrix interface of the neighboring fiber and reduces again. These local variations are caused by the general stress reduction with the distance from the fiber and the shielding effect of fibers F#1 and F#3 described in Section 4.2.

5.3 EFFECT OF FIBER VOLUME FRACTION ON CRACK GROWTH

The analysis above only treats the reference case ($V_f = 0.338$), but it is of interest to clarify whether the results hold for other V_f as well. In Figure 2 the trade-off between increased fiber volume fraction and decreased capacity ratio is shown: mechanical performance increases, but at the same time each fiber cannot be fully intercalated due to limited Li available in the matrix.

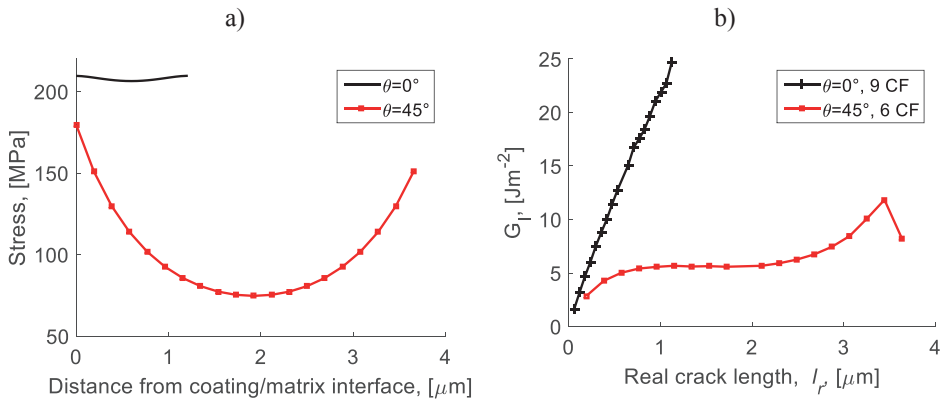


Figure 15. a) The σ_y and $\sigma_{y'}$ stress distribution in $\theta = 0^\circ$ and $\theta = 45^\circ$ directions for $V_f = 0.482$. b) G_I vs crack length.

In Figure 15a the σ_y and $\sigma_{y'}$ stress in the matrix for $V_f = 0.482$ is shown. In the same manner as for the reference case the stress at the coating/matrix interface in the undamaged composite is higher along the x -direction compared to the x' -direction, meaning higher probability for crack initiation at $\theta = 0^\circ$.

G_I for crack growth in the two directions $\theta = 0^\circ$ and $\theta = 45^\circ$ is shown in Figure 15b based on the “ $\theta = 0^\circ, 9 CF$ ” and “ $\theta = 45^\circ, 6 CF$ ”-models. The same trends apply for the $V_f = 0.482$ as for the reference case shown in Figure 14, but with lower values. As in the reference case, the matrix material is fully deintercalated, but the difference is that for higher V_f each fiber is only partially intercalated. In addition, the distance between fibers is shorter and the crack never reaches the length as in the reference case. Since the ERR is roughly proportional to the crack length, it explains the significantly lower values of ERR in the $V_f = 0.482$ case.

6. ENERGY RELEASE RATE FOR DEBOND CRACK PROPAGATION

In *Section 4* it was shown that radial stresses at the fiber boundary and also at the coating/matrix interface in the undamaged composite are compressive during both charging and discharging, eliminating the risk of debonding. However, due to the presence of a radial crack in the matrix, the stress distribution changes. In Figure 16 the radial and shear stress in the matrix along the coating/matrix interface are shown for different (normalized) crack lengths in the $\theta = 0^\circ$ direction. For a short radial crack, the radial stress distribution is very similar to that without damage, compressive along the entire interface; except for a very local radial crack tip region where it is tensile and very high, Figure 16a. For longer radial cracks, especially when the crack has almost reached the next fiber; the high tensile radial stresses region slightly increases. In Figure 16 b it can be seen that the shear stress distribution along the interface is greatly affected, due to the presence of a radial crack, leading to large values not only at the radial crack tip but in a large region. The combined action of high tensile radial stresses and shear stresses near the tip of the crack is a very probable cause for initiation of small debonds. Growth of these debonds

will be analyzed in this section using geometry shown in Figure 17a. Due to the used symmetry, this model simulates a case of two radial cracks starting in opposite points of the interface, each with a debond of the same size

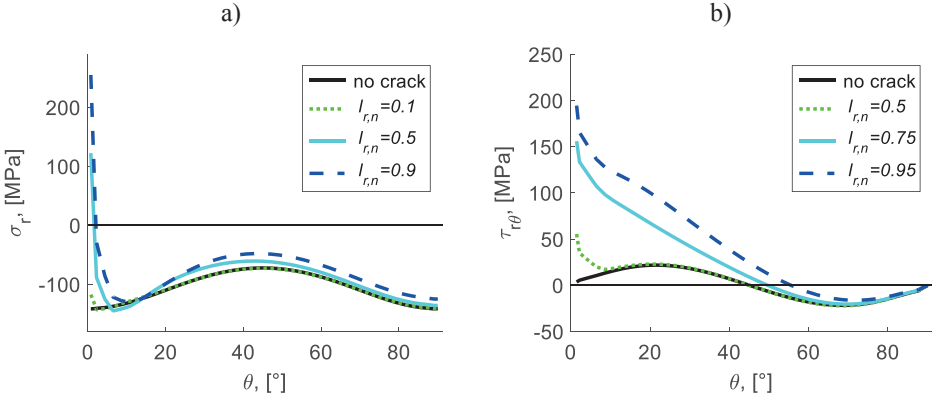


Figure 16. a) Matrix radial stress distribution at coating/matrix interface. b) Matrix shear stress distribution at coating/matrix interface

The ERR for coating/matrix debond crack growth for two different normalized matrix crack lengths with respect to the distance between fibers, $l_{r,n} = 0.5$ and $l_{r,n} = 0.9$, are shown in Figure 17b. The debond growth at the coating surface is governed by the Mode II ERR, with diminishing values with increasing debond angle α . As expected, the ERR for the debond growth increases with the length of the radial crack.

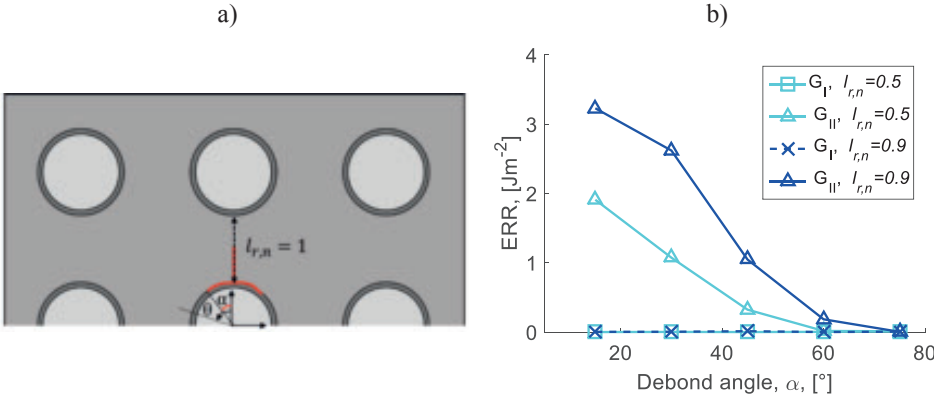


Figure 17. a) Schematic of coating/matrix debonding in the presence of a radial matrix crack. b) ERR of debond crack subjected to electrochemical loading.

In Figure 18 the radial stress distribution in the matrix is shown for the two normalized matrix crack lengths with respect to the distance between fibers, $l_{r,n} = 0.5$ and $l_{r,n} = 0.9$, with debond angular length $\alpha = 15^\circ$ and $\alpha = 75^\circ$, respectively. The debond crack tip is indicated on each stress curve. As can be seen, close to the debond crack tip, the radial stress is negative, which means that the front part of the debond crack is closed and the two debond surfaces are in contact by sliding. For debond angle $\alpha = 15^\circ$, for both radial crack lengths the radial stress is compressive over the whole debond crack surface. For a $\alpha = 75^\circ$ debond in the case of radial crack length $l_{r,n} = 0.5$, the matrix remains in compression along the entire coating surface. However, for $\alpha = 75^\circ$ with long radial crack, $l_{r,n} = 0.9$, the radial stress becomes zero between $\theta = 35^\circ$ and $\theta = 50^\circ$, meaning that there is a radial separation of the two debond surfaces in this region.

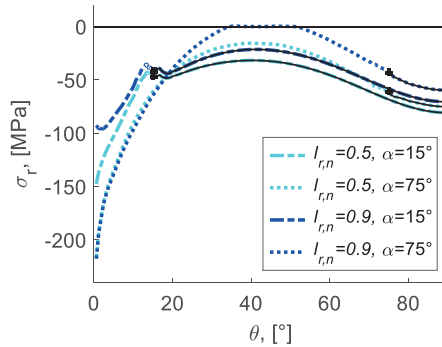


Figure 18. Radial stress distribution in the matrix along the debonded and bonded parts of the coating/matrix interface.

From a battery application point of view debonds with arc type of separation are worse than radial matrix cracks, since they result in lost connectivity between the constituents, while creating new surfaces for unwanted side-reactions.

Comparing the ERR values for matrix cracks in Figure 13 with the ERR values for interface cracks presented in Figure 17, we see that in the latter case the ERR is about 10 times lower.

Neither the fracture toughness of the matrix nor that of the interface is known, but the values could be similar. For the interface crack we have Mode II propagation with fracture toughness in Mode II usually being several times higher than in Mode I. The presented values lead to conclusion that most probably the matrix crack will keep growing until stopping at the next fiber and only then, the interface crack will develop (most probably during cyclic charging and discharging).

7. CONCLUSIONS

In this work, multiphysics simulations and linear elastic fracture mechanics have been used to analyze radial crack propagation in the matrix material under pure electrochemical loading of the micro-battery consisting of a solid electrolyte coated carbon fiber embedded in a electrochemically active polymer matrix. It was shown that a simplified modeling strategy can be adopted by assuming uniform Li distribution in the fiber and in the matrix corresponding to the capacity ratio $R_{P/N}$ in the fiber.

Stress analysis shows that high hoop stress in the matrix at the coating/matrix interface during charging may be a reason for radial matrix cracks initiating at the coating/matrix interface. Propagation of these cracks was studied by calculating energy release rate (ERR) assuming square packing of fibers. For a micro-battery (unit in the structural composite) containing electrodes balanced with respect to storage capacity, with $V_f = 0.338$, results show that the crack growth towards the nearest fiber in $\theta = 0^\circ$ direction is unstable, whereas the crack growth in the $\theta = 45^\circ$ direction includes both stable and unstable propagation regions. The ERR for growth in $\theta = 0^\circ$ direction is larger. Composites with higher V_f have the same trends, but with lower G_I values.

In the presence of a radial crack, large tensile radial and shear stresses at the coating/matrix interface make the debonding relevant for consideration. Results for ERR show that the debond crack growth is governed by Mode II. The ERR values for the interface crack growth are of an order of magnitude lower than for the radial matrix crack growth.

Acknowledgments

The Swedish Energy Agency, project 37712-1 is acknowledged for financial support. KOMBATT-II project members are acknowledged for valuable discussions and input on this work.

References

1. Garrett KW, Bailey JE. Multiple transverse fracture in 90° cross-ply laminates of a glass fibre-reinforced polyester. *J Mater Sci* 1977;12(1):157-168.
2. McCartney LN. Predicting transverse crack formation in cross-ply laminates | this article represents the author's contribution to a world-wide exercise to confirm the state-of-the-art for predicting failure in composites, organised by Hinton and Soden. *Compos Sci Technol* 1998;58(7):1069-1081.
3. Nairn JA, Hu S, Bark JS. A critical evaluation of theories for predicting microcracking in composite laminates. *J Mater Sci* 1993;28(18):5099-5111.
4. Dvorak GJ, Laws N. Analysis of Progressive Matrix Cracking In Composite Laminates II. First Ply Failure. *J Compos Mater* 1987;21(4):309-329.
5. Varna J, Berglund LA, Ericson ML. Transverse single-fibre test for interfacial debonding in composites: 2. Modelling. *Compos Part A Appl Sci Manuf* 1997;28(4):317-326.
6. Bouhala L, Makradi A, Belouettar S, Kiefer-Kamal H, Frères P. Modelling of failure in long fibres reinforced composites by X-FEM and cohesive zone model. *Compos Part B: Eng* 2013;55:352-361.
7. Kushch VI, Shmegeera SV, Brøndsted P, Mishnaevsky Jr. L. Numerical simulation of progressive debonding in fiber reinforced composite under transverse loading. *Int J Eng Sci* 2011;49(1):17-29.
8. Távara L, Mantic V, Graciani E, París F. Modelling interfacial debonds in unidirectional fibre-reinforced composites under biaxial transverse loads. *Compos Struct* 2016;136:305-312.
9. Toya M. A crack along the interface of a circular inclusion embedded in an infinite solid. *J Mech Phys Solids* 1974;22(5):325-348.
10. París F, Caño JC, Varna J. The fiber-matrix interface crack — A numerical analysis using Boundary Elements. *Int J Fract* 1990;82(1):11-29.

11. Sandino C, Correa E, Paris F. Numerical analysis of the influence of a nearby fibre on the interface crack growth in composites under transverse tensile load. *Eng Fract Mech* 2016;168:58-75.
12. Zhuang L, Pupurs A, Varna J, Ayadi Z. Fiber/matrix debond growth from fiber break in unidirectional composite with local hexagonal fiber clustering. *Compos B Eng* 2016;101:124-131.
13. Zhuang L, Talreja R, Varna J. Transverse crack formation in unidirectional composites by linking of fibre/matrix debond cracks. *Compos Part A Appl Sci Manuf* 2018;107:294-303.
14. Zhuang L, Pupurs A, Varna J, Talreja R, Ayadi Z. Effects of inter-fiber spacing on fiber-matrix debond crack growth in unidirectional composites under transverse loading. *Compos Part A Appl Sci Manuf* 2018;109:463-471.
15. Busschen At. Micromechanical Modelling of the Transverse Strengths of Unidirectional Glass Fibre Reinforced Polyester. Ph.D Thesis, Delft University of Technology, The Netherlands, Faculty of Mechanical Engineering and Marine Technology, 1996.
16. Zhang L. Time-Dependent Behaviour of polymers and Unidirectional Polymeric Composites. Ph. D, Delft University of Technology, The Netherlands, Faculty of Mechanical Engineering and Marine Technology, 1995.
17. Penn LS, Chou RCT, Wang ASD, Binienda WK. The Effect of Matrix Shrinkage on Damage Accumulation in Composites. *J Compos Mater* 1989;23(6):570-586.
18. Asp LE, Greenhalgh ES. Structural power composites. *Composites Sci Technol* 2014;101:41-61.
19. Jacques E, Hellqvist Kjell M, Zenkert D, Lindbergh G, Behm M. Expansion of carbon fibres induced by lithium intercalation for structural electrode applications. *Carbon* 2013;59:246-254.
20. Zhang W-. Structure and performance of LiFePO₄ cathode materials: A review. *J Power Sources* 2011;196(6):2962-2970.
21. Xu J, Göran Lindbergh, Varna J. Carbon fiber composites with battery function: Stresses and dimensional changes due to Li-ion diffusion. *J Compos Mater* 2018:0021998317752825.
22. Krueger R. Virtual crack closure technique: History, approach, and applications. *Appl Mech Rev* 2004;57(1-6):109-143.
23. Hamann CH, Hamnett A, Vielstich W. *Electrochemistry*. Weinheim: Wiley-VCH, 2007.
24. COMSOL Multiphysics® v. 5.2. www.comsol.com. COMSOL AB, Stockholm, Sweden.
25. Doyle M, Fuller T, Newman J. Modeling of galvanostatic charge and discharge of the lithium/polymer/insertion cell. *J Electrochem Soc* 1993;140(6):1526-1533.
26. Fuller TF, Doyle M, Newman J. Simulation and Optimization of the Dual Lithium Ion Insertion Cell. *J Electrochem Soc* 1994;141(1):1-10.
27. Gabrielli G, Marinaro M, Mancini M, Axmann P, Wohlfahrt-Mehrens M. A new approach for compensating the irreversible capacity loss of high-energy Si/C|LiNi_{0.5}Mn_{1.5}O₄ lithium-ion batteries. *J Power Sources* 2017;351:35-44.

28. Williard N, He W, Hendricks C, Pecht M. Lessons learned from the 787 dreamliner issue on Lithium-Ion Battery reliability. *Energies* 2013;6(9):4682-4695.
29. Kim C, Jeong KM, Kim K, Yi C. Effects of Capacity Ratios between Anode and Cathode on Electrochemical Properties for Lithium Polymer Batteries. *Electrochimica Acta* 2015;155:431-436.
30. Xu J, Lindbergh G, Varna J. Multiphysics modeling of mechanical and electrochemical phenomena in structural composites for energy storage: Single carbon fiber micro-battery. *J Reinf Plast Compos* 2018;37(10):701-715.
31. Pupurs A, Varna J. Modeling mechanical stress and exfoliation damage in carbon fiber electrodes subjected to cyclic intercalation/deintercalation of lithium ions. *Compos B Eng* 2013.
32. Hashin Z. Analysis of Composite Materials- A Survey. *J Appl Mech Trans ASME* 1983;50(3):481-505.
33. Dionisi F, Harnden R, Zenkert D. A model to analyse deformations and stresses in structural batteries due to electrode expansions. *Compos Struct* 2017;179:580-589.
34. Ihrner N, Johannisson W, Sieland F, Zenkert D, Johansson M. Structural lithium ion battery electrolytes: Via reaction induced phase-separation. *J Mater Chem A* 2017;5(48):25652-25659.
35. Ihrner N, Johansson M. Improved performance of solid polymer electrolytes for structural batteries utilizing plasticizing co-solvents. *J Appl Polym Sci* 2017;134(23).
36. Arora P, White RE, Doyle M. Capacity fade mechanisms and side reactions in lithium-ion batteries. *J Electrochem Soc* 1998;145(10):3647-3667.

Appendix 1

The physics-based electrochemical model to describe the micro-battery is a multi-scale model, consisting of a coupled system of 11 nonlinear partial differential equations (PDE) with 11 unknowns, presented in Table A1.1. The governing equations and corresponding boundary conditions are presented in detail in [30]. The equations describe the spatial and time dependent variation in lithium concentration as well as the electrical potential in the solid (active material) and electrolyte phases. The model is divided into three domains: fiber (negative electrode), coating (separator) and matrix (positive electrode), denoted Ω_f, Ω_c and Ω_m respectively, Figure 1.

Table A1.1. The variables in the electrochemical model

Symbols	Description	Unit
$\Phi_{s,m}$	Electrical potential in solid phase of matrix electrode	V
$\Phi_{e,c}$ and $\Phi_{e,m}$	Electrical potential in electrolyte phase in coating and matrix, respectively	V
J_f and J_m	Molar fluxes	mol/m^3
$c_{salt,c}$ and $c_{salt,m}$	Salt concentration in electrolyte phase in coating and matrix, respectively	mol/m^3
$c_{solv,c}$ and $c_{solv,m}$	Solvent concentration in electrolyte phase in coating and matrix, respectively	mol/m^3
c_f and c_p	Li concentration in active materials, fiber and particle	mol/m^3

Appendix 2

Lithium-ion cells operate by cycling lithium ions between two insertion electrode hosts having different capacities. For optimum performance, the ratio of the lithium-ion capacities of the two host materials should be balanced, as described in details in [36]. The ratio between the capacity of the negative and the positive electrode, $R_{P/N}$, is defined as

$$R_{P/N} = \frac{j_{1C}^+}{j_{1C}^-} \quad (A2.1)$$

where j_{1C} is the current density [A/m^2] for 1C discharge rate, superscripts + and - represent the positive (matrix) and negative (fiber) electrode respectively, j_{1C} is given by

$$j_{1C}^+ = \frac{c_{s,max}^+ \cdot \varepsilon_s^+ \cdot F \cdot V^+}{1[h]} \quad j_{1C}^- = \frac{c_{s,max}^- \cdot F \cdot V^-}{1[h]} \quad (A2.2)$$

where ε_s^+ is the porosity of the positive electrode, F is the Faraday constant, $F = 96487 \text{ A s} \cdot \text{mol}^{-1}$, V^+ and V^- is the volume of the positive and negative electrodes, respectively, $c_{s,max}^+$ and $c_{s,max}^-$ is the maximum Li concentration in the positive electrode active material (LiFePO₄) and fiber electrode, respectively, defined as

$$c_{s,max}^+ = \frac{Q_{spec}^+ \cdot \rho^+}{F} \quad c_{s,max}^- = \frac{Q_{spec}^- \cdot \rho^-}{F} \quad (A2.3)$$

where Q_{spec}^+ and Q_{spec}^- are specific capacities, defined as the amount of charge per weight that a battery electrode material contains. This is a fundamental characteristic of the materials, and depends upon its redox chemistry and structure. Parameters of the electrochemical model for calculating the capacity ratio are listed in Table A2.1.

Table A2.1 Properties of the electrode active material.

Parameter	Description	Value
Q_{spec}^+	Specific capacity, positive electrode	169 [mAh/g]
Q_{spec}^-	Specific capacity, negative electrode	372 [mAh/g]
ρ^+	Density, positive electrode	3600 [kg/m ³]
ρ^-	Density, negative electrode	1780 [kg/m ³]

Eq. (A2.2)-(A2.3) in Eq. (A2.1) gives:

$$R_C = \frac{j_{1C}^+}{j_{1C}^-} = \varepsilon_s^+ \cdot \frac{Q_{spec}^+}{Q_{spec}^-} \cdot \frac{\rho^+}{\rho^-} \cdot \frac{Vol^+}{V^-} \quad (A2.4)$$

where

$$\frac{V^+}{V^-} = \frac{(r_f + t_{SBE} + t_{cath})^2 - (r_f + t_{SBE})^2}{r_f^2} \quad (A2.5)$$

r_f , t_{SBE} and t_{cath} are dimensions for the fiber radius and thicknesses of the coating and matrix, shown in Table A2.2.

Table A2.2. Dimensions of battery cell constituents for the reference case.

Constituent	Description	Symbol	Value
Carbon fiber	radius	r_f	2.5 μ m
SBE	thickness	t_{SBE}	0.1 μ m
Matrix	thickness	t_{cath}	1.7 μ m

Paper IV

MATRIX AND INTERFACE CRACKING IN CROSS-PLIED COMPOSITE STRUCTURAL BATTERY UNDER COMBINED ELECTROCHEMICAL AND MECHANICAL LOADING

Johanna Xu, Janis Varna

¹Department of Engineering Sciences and Mathematics, Luleå University of Technology SE-97187 Luleå, Sweden

ABSTRACT

In this paper propagation of matrix cracks and debonds at the coating/matrix interface in the 90°-layer of a cross-ply structural composite battery are studied numerically. The structural composite battery consists of micro-battery units, made of a solid electrolyte coated carbon fiber embedded in an electrochemically active polymer matrix. During charging the fiber swells and the matrix shrinks leading to high stresses on the fiber/matrix scale and to anisotropic free expansion of the composite ply. Two load cases are considered, pure electrochemical load (intercalation) and combined electrochemical and thermomechanical load. Energy release rates (ERR) of radial matrix cracks along two potential propagation paths are calculated using 2-D finite element models of the transverse plane in a cross-ply laminate with a square packing of fibers in the 90°-ply and using homogenized 0°-ply. Results show that the matrix crack growth towards the nearest fiber is unstable, and that the debond crack growth is in mixed mode. For a cross-ply structural battery composite the sequence of macro-scale crack forming events differs from a conventional cross-ply composite, as well as for a UD composite battery laminate. The most likely course of failure events in a cross-ply laminate are: 1) vertical radial matrix crack initiation and unstable growth; 2) debond is initiated at certain length of the matrix crack.

1. INTRODUCTION

For a conventional high performance composite laminate subjected to tensile (and/or hygrothermal) loading, a ply transverse cracking is the damage formed first [1]. This failure mode, often referred as matrix cracking is caused by the combined action of in-plane tensile transverse and shear stresses in the ply. Although the immediate effect of microcracking can be a rather

insignificant deterioration of mechanical properties of the laminate, its subsequent failure events such as interlayer delaminations and fiber failures in neighboring layers may certainly lead to severe degradation of the structure [1-3].

The transverse failure on microscale is widely studied, the sequence of phenomena usually starts with a debond crack running circumferentially at the fiber/matrix interface. After these cracks have grown to a certain length, due to large tensile radial and shear stresses acting on the interface, in a second step they kink-off from the interface, giving rise to a macro-crack formation in the composite. Mechanics of these processes has been studied in many models of varying degree of complexity. Most often the analysis is using the energy release rate (ERR) calculations based on linear elastic fracture mechanics [4-6]. The basic mechanisms of fiber/matrix debond growth were understood in studies of a single fiber embedded in an infinite matrix [6-9].

In the current paper the material considered is a so called structural composite battery, where both the cause for damage initiation and the course of damage events appear different from the above-mentioned conventional composite. The structural composite battery is a multifunctional fiber composite, which delivers electrical energy via electrochemical reactions while carrying mechanical load. The achieved synergetic multifunctionality of such material may allow for large mass and volume savings [10]. One route for realization of structural composite batteries is via the three-dimensional (3D) structural battery concept developed by Asp and co-workers [10-12].

A conventional lithium-ion battery does not have structural functions. It is composed of a negative electrode, a positive electrode, and an electrolyte that allows for ionic conductivity. Batteries also have separators to prevent short circuits. The negative electrode typically consists of graphite-based materials. The positive electrode is commonly a porous mixture containing lithium metal oxide/phosphate. The task of the electrolyte is to transport ions between the electrodes. Usually the electrolyte consists of a lithium salt and solvent in liquid form. During charge lithium-ions (Li) are

oxidized and extracted from the positive electrode. Electrons travel in an external circuit and the lithium-ions diffuse to the negative electrode via the electrolyte. At the negative electrode the lithium ions are inserted. This insertion/extraction mechanism of lithium ions is called intercalation/deintercalation, and the material hosting the lithium ions is referred to as “active material”. When we discharge the battery, the processes are reversed, Figure 1a.

Intercalation/deintercalation causes swelling/shrinking in the electrodes. For conventional batteries where it is mainly a battery safety and durability concern (short-circuiting, self-discharge etc), this phenomenon is well-known and studied. However, for a structural battery it is a completely different matter, as the swelling/shrinking results in mechanical stresses that may cause damage to the composite impairing both mechanical and battery performances. In the 3D structural composite battery architecture, carbon fibers constitute the negative electrode, with individual carbon fibers coated by a few hundred nanometers thick solid battery electrolyte (SBE) material [13]; which is electrically insulating as well. A solid positive electrode material, called the cathode, made from a LiFePO_4 doped solid polymer electrolyte matrix material, surrounds the coated fibers. The shrinking and swelling of fibers and matrix happens as lithium ions intercalate into the fiber during charging and back into the matrix during discharging. Experimental work by Jacques et. al [14] showed that intercalation of lithium ions into PAN-based carbon fiber causes a 1% longitudinal expansion, and a 8-13% increase in cross sectional area. It is known that the active material in the positive electrode, LiFePO_4 is swelling approximately 7% upon lithiation [15]. In Figure 1b the 3D structural composite battery is shown on different length scales, from the matrix which is a particulate composite with active electrode material, via the three-phase (fiber, coating, matrix) concentric cylinder assemble for each battery unit, to a unidirectional (UD) lamina scale. As with conventional composite laminates, the UD plies are stacked in well-designed configurations (laminates), to be useful in a load bearing structure.

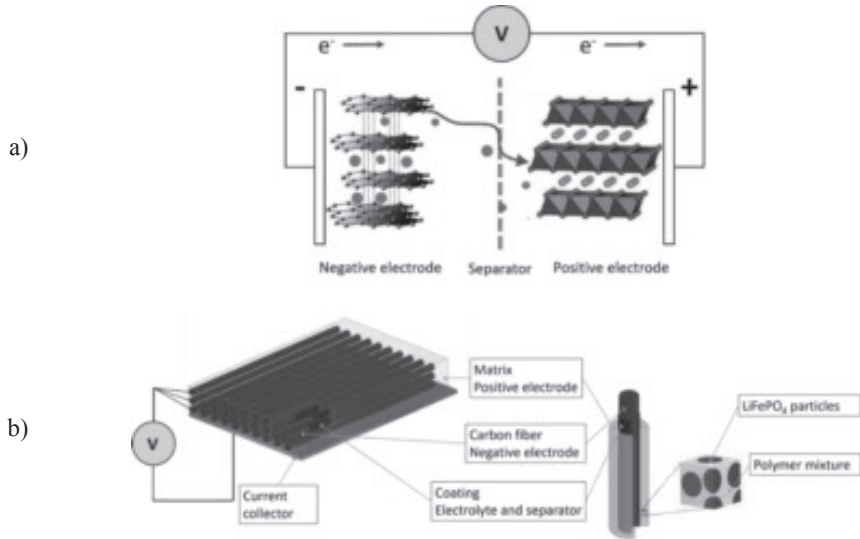


Figure 1. a) Schematic representation of a conventional lithium-ion battery during discharge. b) Schematic illustration of the 3D structural composite battery on different length scales. (From left to right: unidirectional composite lamina, single battery unit, matrix as a particle composite.)

In [16] initiation and growth of radial and arc-shaped cracks in the fiber was studied. The transient ion concentration distribution and corresponding stress distribution showed that radial cracks may appear in the fiber during intercalation/deintercalation, from which arc cracks may deflect. However, the ion concentration obtained from heat transfer analogy with convection boundary conditions on the fiber surface used in [16], overestimates the gradients in the fiber and thus the mechanical stresses.

Li distributions obtained from multi-physics model [17,18] show that damage due to intercalation is likely to occur in the matrix material rather than in the fiber. The arising stresses in the matrix during the charging and discharging can be so high that microcracks may initiate and grow without any applied external load[18]. Particularly, the tensile hoop stresses close to the fiber surface are so high that radial crack formation in the matrix is one of the most probable micro-damage modes.

In [19] the ERR for radial crack growth along two potential propagation paths in a square packing

configuration were calculated for pure electrochemical loading of the UD lamina. Furthermore, in the presence of a radial crack, large tensile radial and shear stresses at the coating/matrix interface make the debonding relevant for consideration as well. Debonding is critical for mechanical as well as electrochemical performance of the material as it impedes load transfer and ion-transport between constituents in the structural battery. Results for ERR show that the debond crack growth in a UD composite is governed by Mode II. The ERR values for the interface crack growth are of an order of magnitude lower than for the radial matrix crack growth.

In a multidirectional laminate, the anisotropic swelling of an individual lamina causes mesoscale (ply-level) stresses in addition to micro-stresses due to fiber/matrix interaction. Thermo-mechanical loading applied to the laminate is also contributing to the stress build-up. In this present work Mode I and Mode II ERR are analyzed using stress fields calculated with finite element method (FEM) for a cross-ply laminate with assumed square packing of fibers. The fiber/coating/matrix microstructure of the 90°-layer in the laminate is explicitly included in the model, whereas homogenized properties are used for the 0°-layer in the laminate. The objective is to study the matrix and debond crack growth under combined intercalation and thermomechanical loading.

2. HOMOGENIZATION

Homogenization is used to compute: a) the effective properties of the matrix, which is a particulate composite, and b) the homogenized properties of the UD composite, Figure 2. The UD ply properties are necessary in developing multi-fiber models for microcracking analysis to reduce the number of explicitly considered fibers and to adequately account for the constraint applied by surrounding layers in a multidirectional laminate.

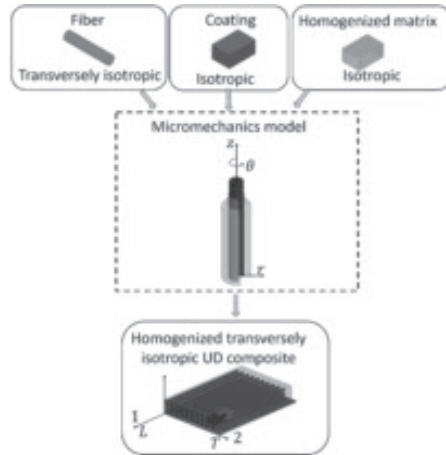


Figure 2. Modeling scheme for effective properties of UD composite.

In this study only one fiber volume fraction, $V_f=0.338$, is considered, which is referred to as the “reference case”, to be consistent with previous studies [17,18]. The reason for this particular V_f is to accommodate for the lithium ion storing capacity in the fiber and in the active material of the matrix. The aim is to have a volume fraction ensuring that a) almost all Li from the matrix can be transported to the fiber, and b) the fiber can be fully intercalated.

Elastic properties of the UD composite are calculated using the concentric cylinder assembly (CCA) model introduced by Hashin [21,22]. Explicit expressions are obtained for the effective plane-strain bulk modulus K_{23} , the shear modulus G_{12} , longitudinal modulus E_1 and Poisson’s ratio ν_{12} . The transverse shear modulus is obtained by using a self-consistent scheme, first introduced by Christensen and Lo [23]. The entire set of equations can be found in [24]. In [20] the effect of state of charge on elastic properties of 3D structural composite battery was studied using the CCA model, it was found that the effect is significant for transverse properties E_2 and G_{23} for high V_f , which is not considered in this present study.

The matrix is a particulate composite with isotropic effective properties. The composite spheres

assemblage (CSA) introduced by Hashin [22] is a micromechanical model that can be used to obtain the effective properties of the matrix. Assuming two phases present, the spherical LiFePO₄ active material represents the particle phase, and the remaining constituents (SBE, carbon black and additional binder material) together comprise the so-called slurry phase. The LiFePO₄ particles expand/shrink upon intercalation/deintercalation with a swelling coefficient β [15]. The used values of elastic and swelling parameters for the matrix constituents are shown in Table 1.

Table 1. Assumed properties of matrix constituents.

Constituent	E (GPa)	ν (-)	β (-)
LiFePO ₄	125	0.28	0.07
Slurry	1	0.3	0

In Table 2 the properties of the fiber, coating and the homogenized matrix (with a particle volume fraction $V_p = 0.553$) are presented along with the calculated the UD composite properties.

Table 2. Assumed and calculated elastic constants and intercalation swelling parameters.

Constituent	E_z (GPa)	E_r (GPa)	ν_{zr} (-)	$\nu_{r\theta}$ (-)	Expansion	
					β_z (-)	β_r (-)
Fiber	300	30	0.2	0.45	0.009	0.05
SPE coating	1	1	0.3	0.3	0	0
matrix, $V_p = 0.553$	2.5	2.5	0.3	0.3	0.04	0.04
	E_L (GPa)	E_T (GPa)	ν_{LT} (-)	ν_T (-)	β_L (-)	β_T (-)
UD composite, ($V_f=0.338$)	103.0	4.0	0.27	0.47	0.0089	-0.017

The expansion coefficients for the UD composite β_L and β_T require special discussion presented below. Free expansion of electrode host materials due to intercalation is a well-known phenomenon [25-27]. Initially, it may seem tempting to model this mechanism by following the approach of well-studied models of other volume changing phenomena in fiber reinforced composites, such as moisture absorption. However, the moisture weight in the composite increases during absorption, which makes the moisture weight fraction a suitable variable to use in modeling. In contrast, the amount of Li in the composite material is constant, but the content in the constituents changes

(redistributes) during charging/discharging causing dimensional changes of the constituents and the whole composite. Therefore, the effective composite intercalation expansion cannot be related to the amount of available lithium (which is not changing). A different variable has to be introduced to correlate with the macroscopic dimensional changes, and in this study the normalized average Li content in the fiber, $c_{f,avg}/c_{f,max}$ was used. $c_{f,avg}$ is the average Li concentration in the fiber, and $c_{f,max}$ is the carbon fiber maximum Li storing capacity.

According to linear theory, the intercalation is inducing dimensional changes (strains) to the composite, ε^I , which are proportional to $c_{f,avg}/c_{f,max}$, and different in different directions, Eq. (1) in matrix form

$$\begin{pmatrix} \varepsilon_L^I \\ \varepsilon_T^I \\ \gamma_{LT}^I \end{pmatrix} = \begin{pmatrix} \beta_L \\ \beta_T \\ 0 \end{pmatrix} \frac{c_{f,avg}}{c_{f,max}}. \quad (1)$$

For the UD composite the reference state with zero macroscopic expansion and zero micro-stresses is when the Li content in the fiber is zero (discharged) and the matrix is fully charged. The expansion coefficient in the fiber direction, β_L , can then be described by a simple rule-of-mixture expression [18]

$$\beta_L = \frac{E_z^f V_f \beta_z^f + E_m V_m \beta^m}{E_z^f V_f + E_m V_m} \quad (2)$$

The effect of the thin coating layer is neglected in (2). The expansion coefficient in the composite transverse direction, β_T , is obtained from radial displacements calculated from the coupled electrochemical-mechanical model [17]

$$\beta_T = \beta_r = \frac{\varepsilon_r}{(c_{f,avg}/c_{f,max})} \quad (3)$$

where ε_r is the radial strain calculated from the radial displacement, u_r , at the outer CCA boundary, Figure 2.

It appears that the transverse swelling coefficient of the UD composite calculated using this concept

is actually not a constant value: it depends on Li concentration. However, the stress analysis performed in [9] showed that the worst stress state is in the instant at the end of the charging. Hence, when analyzing the crack growth, we focus on this instant only and β_T in this instant is of interest; the value is given in Table 2.

In order to maintain the accuracy of ERR for radial crack propagation, it is important not to place the homogenized material too close to the crack under investigation. In Figure 3 schematics of the FE-model used in this study is shown, with explicit undamaged fiber/coating/matrix units located adjacent to the “central fiber” with radial matrix crack. The considered laminate is $[(0/90)_n]_s$ with very thin plies (3 fibers).

Analysis was conducted using commercial finite element (FE) software ANSYS APDL[®]. Eight-node “PLANE183” quadrilateral elements were used, with generalized plane strain behavior. Coupling conditions for normal displacement were applied to outer boundary of the unit cell to reflect the repeatability of the microstructure (coupl. DoF in Figure 3).

The geometrical parameters including interfiber distance, l_{ID} , for the reference case are listed in Table 3. Two directions of radial matrix crack growth are considered in this study. The matrix crack perpendicular to the 0°-layer, Figure 3a, is denoted “vertical crack”, and matrix crack growing parallel with the 0°-layer is denoted “horizontal crack”, Figure 3b. In [19] it was shown that having one fiber on each side of the damaged fiber unit in the x-direction is sufficient to represent a matrix crack in an infinite ply in the laminate.

Table 3. Geometrical parameters of the unit cell for the reference case $V_f = 0.338$.

Parameter	Value [μm]
r_f	2.5
r_c	0.1
l_{ID}	2.4

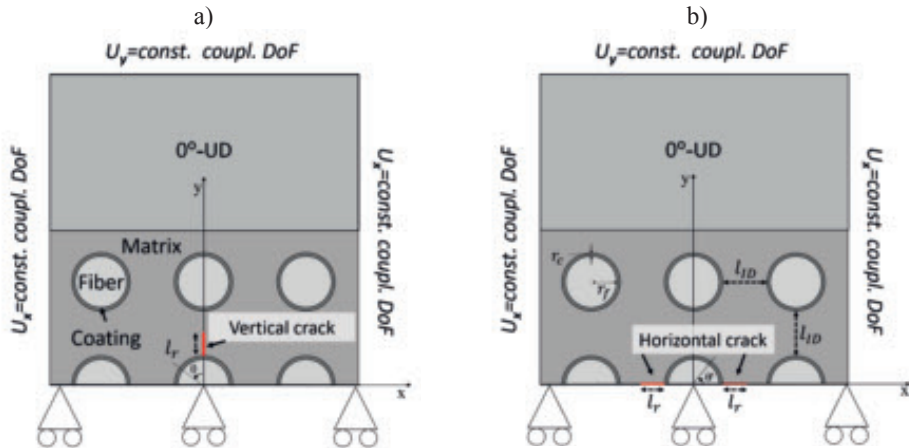


Figure 3. Schematics of the FEM model with boundary conditions for a) vertical crack and b) horizontal crack in the matrix starting from coating/matrix interface and growing towards adjacent fiber.

3. INTERCALATION INDUCED MICROCRACKS

The energy release rate (ERR) of the matrix cracks induced by the intercalation mechanism is calculated by ANSYS built-in virtual crack closure technique (VCCT) [28], providing the fracture mode. Appropriate mesh refinement was used near the crack tip, Figure 4a, where uniform quadrilateral elements were generated ahead of and behind the crack tip, and a mesh convergence study was conducted.

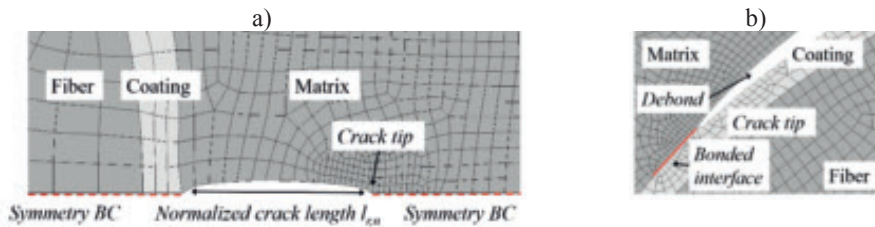


Figure 4. Details of FE model for calculating crack growth related energy release rate, deformed FE mesh for a) the matrix crack tip and b) debond crack tip.

In the FEM model containing coating/matrix interface debonds, the debonded region of the interface is modeled by two coinciding areas; one being matrix and the other being coating, Figure 4b. Contact elements with Lagrange multiplier on contact normal and penalty on tangent were generated on the debonded coating/matrix interface.

3.2 RADIAL MATRIX CRACKS

The difference in the σ_x along the y-axis and σ_y along the x-axis between the central fiber and the adjacent fiber in the undamaged cross-ply material is shown in Figure 5a. It can be seen that added 0° -layer for a cross-ply laminate results in large increase of tensile σ_x in comparison with UD and the stress distribution is rather uniform.

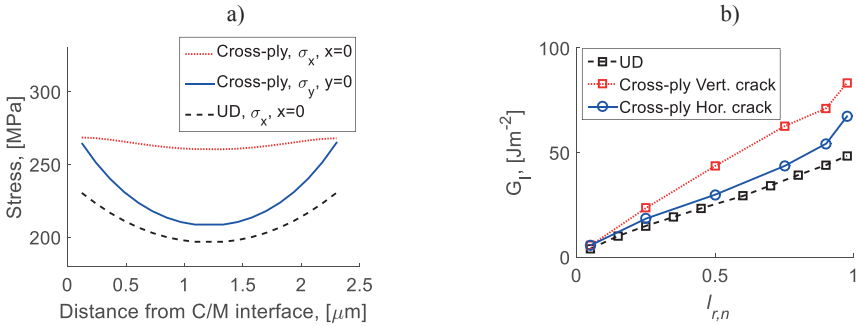


Figure 5. a) σ_y and σ_x distribution between fibers in undamaged composite. b) Variation of ERR as a function of normalized radial crack length $l_{r,n} = l_r/l_{ID}$, for the reference case $V_f=0.338$.

In Figure 5b the Mode I ERR, G_I [J/m^2] at the instant when the fiber is fully intercalated is shown as a function of normalized radial crack length, $l_{r,n} = l_r/l_{ID}$, l_r is the length of the matrix crack, and l_{ID} is the interfiber distance for both crack directions, Figure 3. The Mode I ERR is proportional to the crack length, as typical for cracks in an infinite medium subjected to uniform stress. The ERR for the vertical crack growth is much larger than for the horizontal and both are larger than in the UD composite.

3.3 DEBONDING AT COATING/MATRIX INTERFACE

The presence of a radial crack, imposes changes to the stress distribution at the coating/matrix interface. In Figure 6(a,b) and Figure 7 the radial and shear stress along the coating/matrix interface in a cross-ply laminate is shown, both without matrix crack and for matrix cracks with different normalized crack lengths.

Figure 6a, shows that the radial stress distribution is rather unaffected by the presence of the vertical crack, with the exception of a very local region near the tip of the radial crack where the stresses are tensile and very high for longer radial cracks ($l_{r,n} = 0.5, l_{r,n} = 0.9$). After this region the radial stress is compressive until $\theta < 40^\circ$ is reached where it becomes tensile again.

In Figure 6b it can be seen that the shear stress distribution along the interface is affected to a higher extent by the presence of a radial matrix crack. The shear stress is high not only at the radial crack tip but also in a larger region. The combined action of high tensile radial stresses and shear stresses near the tip of the radial crack could be a likely cause for initiation of debonds.

Figure 6c-Figure 6d show the stresses along the coating/matrix interface in a UD composite [19] not constrained by the 0° -layer. There is a significant difference in terms of radial stress in UD composite in comparison with a cross-ply (Figure 6c). The radial stresses in the UD composite are compressive along the entire interface, with the exception for a very local region close to the crack tip (for longer radial cracks), where the stresses are tensile and very high. As for the shear stress, it can be seen in the comparison between the UD and cross-ply (Figure 6b, d) that both the region with high stress and the magnitude of the stresses are higher for cross-ply layup.

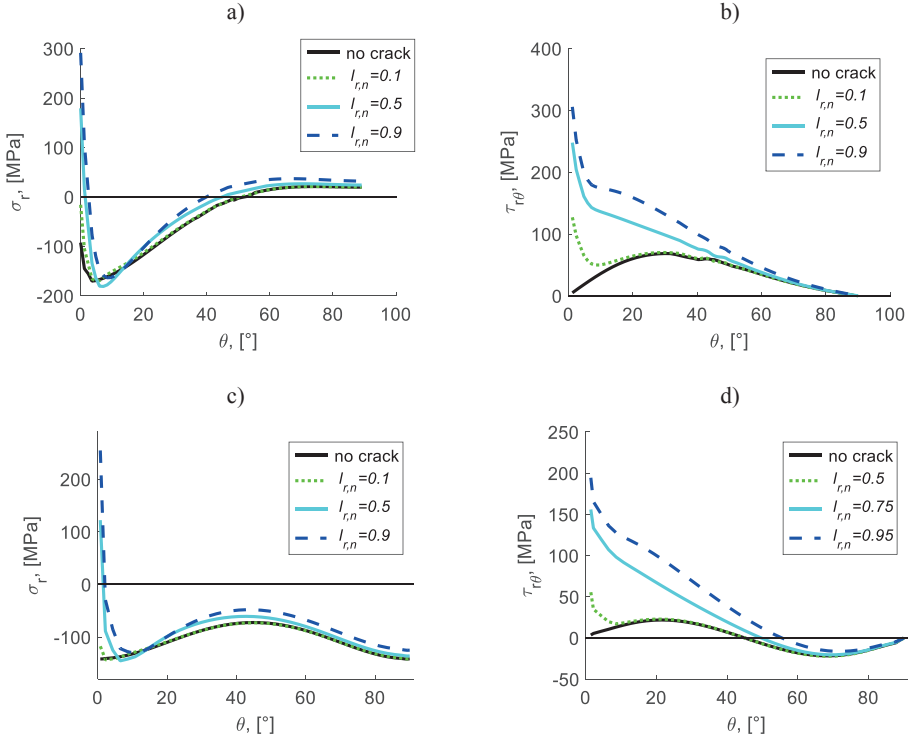


Figure 6. Stress distributions at the coating/matrix interface in 90-layer of a cross ply laminate under pure intercalation loading: a) radial stress distribution and b) shear stress distribution, with and without the impact of a vertical matrix crack. Similar distribution in UD composite, c) radial stress distribution and d) shear stress distribution.

Figure 7a, shows the radial stress distribution along the coating/matrix interface for θ' -coordinate, (Figure 3b), with and without horizontal matrix crack. Like the case with the vertical matrix crack, the radial stress distribution is very similar to that without damage, except the small region close to the matrix crack tip, where the radial stresses are tensile and very high. Since at small angles the radial stress is tensile in absence of the matrix crack, there is possibility to create a debond even without matrix damage. The shear stress distribution, Figure 7b, shows the same trends as in the case of a vertical crack, regarding the influence of matrix cracks.

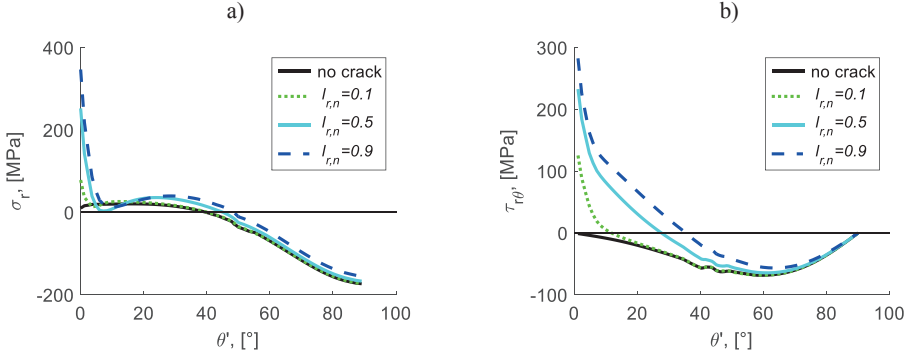


Figure 7. Stress distributions at the coating/matrix interface in 90-layer of a cross ply laminate under pure intercalation loading: a) radial stress distribution and b) shear stress distribution with and without the impact of a horizontal crack.

By comparing the stress distributions shown in Figure 6(a-b) and Figure 7(a-b), we conclude that most probably the debond in both matrix crack cases will initiate at the matrix crack tip, but the growth of debonds occurring in connection to the two different types of radial matrix cracks will be very different. The initiation of a debond before the matrix crack is less likely and if it would happen, then at angle $\theta' = 0^\circ$, where the radial stress is tensile.

In Figure 8a schematics of the debond and the vertical matrix crack are shown. The whole model containing bonded and debonded fibers and matrix cracks is the same as shown in Figure 3a. It has to be noted that due to the used symmetry, this model simulates a case of two radial cracks starting in opposite points of the interface, each with a debond of the same size. The Mode I and Mode II ERR for coating/matrix debond for two different normalized matrix crack length, $l_{r,n} = 0.5$ and $l_{r,n} = 0.9$, are shown in Figure 8(b, c).

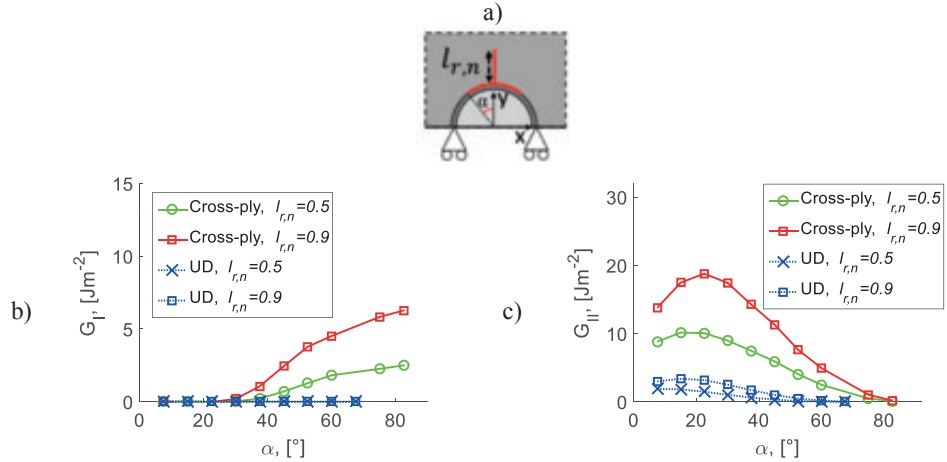


Figure 8. ERR as a function of the debond angular size, for a debond crack along coating/matrix interface originating from vertical matrix crack: a) detail of the model; b) Mode I ERR and c) Mode II ERR

The debond growth at the coating surface is in mixed mode. For small debonds ($\alpha < 30^\circ$) with vertical crack the debond is governed by the Mode II ERR component (G_{II}), Figure 8c, increasing with the debond angle until reaching a peak value at approximately $\alpha = 30^\circ$, then the G_{II} starts to decrease with increasing debond angle α , approaching zero for very large debonds. The Mode I ERR component (G_I), Figure 8b remains insignificant until the same $\alpha = 30^\circ$, where G_I starts to grow with increasing debond angle α . As expected the ERR for debonding is higher for longer matrix crack.

For comparison, debond growth in a UD material is shown in Figure 8 as well, where debond growth is governed by Mode II only, with significantly lower ERR compared to the cross-ply laminate.

In Figure 9a the considered debonds originate from horizontal matrix cracks, other parts of the model and boundary conditions are shown in Figure 3b. In Figure 9b - Figure 9c the mixed mode character of the debond growth with and without horizontal matrix crack is shown. For small

debonds, when the debond crack can be regarded as perpendicular to x-direction, where the tensile stress σ_x in the matrix is the highest, due to constraints from the cross-ply layup. For these small debonds G_I is increasing with increasing debond angle λ . For large debonds ($\lambda \geq 60^\circ$) G_I is greatly reduced, as the debond crack growth direction becomes almost parallel with the x-axis, while generating the maximum value for G_{II} . The impact of the increasing horizontal matrix crack length $l_{r,n}$ on the ERR for debonding is increasing G_I . The effect on G_{II} is more complex: for small debonds it significantly increases but for large debonds it reduces.

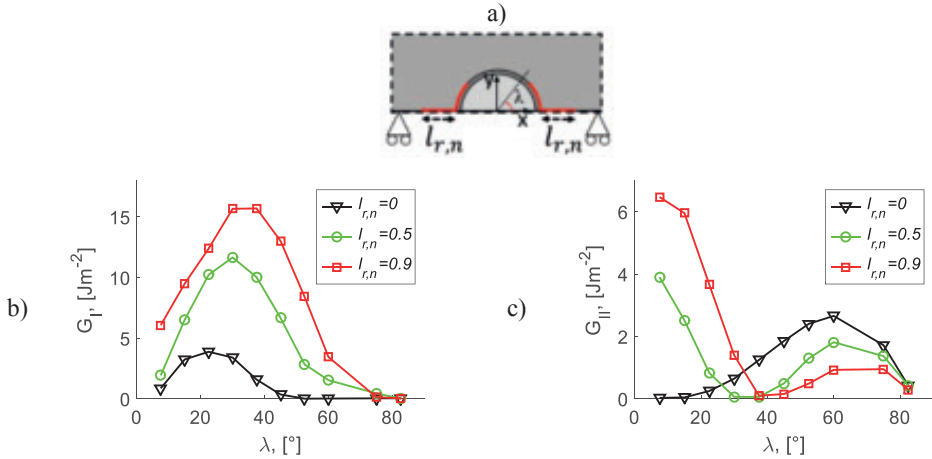


Figure 9. ERR as a function of the debond angular size, for a debond crack along coating/matrix interface originating from horizontal matrix crack : a) detail of the model; b) Mode I ERR and c) Mode II ERR.

4. EFFECT OF COMBINED LOADING ON MICROCRACK GROWTH

In this section the effect of a combined thermo-mechanical load added to the intercalation is analyzed in a cross-ply laminate. In *Section 3* radial crack growth followed by a subsequent debond crack growth in the 90° -layer of a cross-ply laminate was investigated for pure electrochemical loading. In the UD composite the effect of thermal stresses on micro-scale, originating from the cool-down from the curing temperature was shown to be very small in comparison with

intercalation induced stresses [19]. However, in a cross-ply the same cooldown temperature introduces ply-scale stresses that may cause changes in the failure processes discussed above. The impact of thermo-mechanical loading is evaluated as a single event. The temperature load was applied as a temperature difference, $\Delta T = -80^\circ\text{C}$, with calculated coefficient of thermal expansion (CTE) for the UD composite, $\alpha_L = 2.87 \cdot 10^{-7} (1/^\circ\text{C})$ and $\alpha_T = 4.45 \cdot 10^{-6} (1/^\circ\text{C})$. CTE used for the carbon fiber was $\alpha_L = -0.5 \cdot 10^{-6} (1/^\circ\text{C})$ and $\alpha_T = 7.8 \cdot 10^{-6} (1/^\circ\text{C})$ [29,30]. Matrix CTE was assumed $\alpha = 50 \cdot 10^{-6} (1/^\circ\text{C})$.

The mechanical load was applied as a uniform displacement to correspond to the added mechanical strain of $\varepsilon_x = 0.5\%$ to the laminate deformed by electrochemical swelling and temperature change. Figure 10a shows the stress distributions between fibers in x and y -directions for the undamaged cross-ply composite under combined intercalation and thermomechanical loading. The stresses from the added thermo-mechanical load are higher, but with a larger increase for the $\sigma_x(y)$ at $x = 0$ than for $\sigma_y(x)$ at $y = 0$. Consequentially, G_I is larger than in the pure electrochemical case. Figure 10b shows the Mode I ERR variation of the radial matrix crack with thermo-mechanical loads added to the electrochemical load. As in the case for electrochemical load alone, it can be seen that ERR is higher for a crack that grows vertically. The added thermo-mechanical load results in a 10% increase of G_I for the growth in horizontal direction in comparison with pure electrochemical case, and at most about 20% for vertical crack growth.

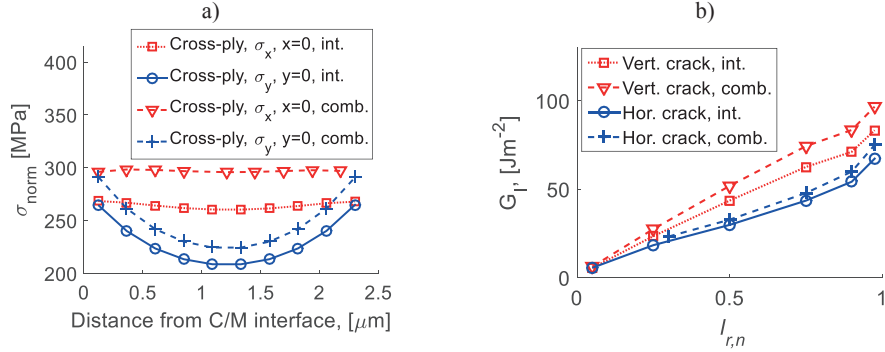


Figure 10. a) Normal stress distribution between fibers in 90°-layer for undamaged composite. b) Variation of Mode I ERR as a function of normalized radial crack length $l_{r,n} = l_r/l_{ID}$, for the reference case $V_f=0.338$ for the two load cases with intercalation only (solid lines) and combined intercalation and thermomechanical load (dashed lines).

In Figure 11a - Figure 11b the effect of combined loading on the Mode I and Mode II ERR for coating/matrix debonding is shown. Just like for intercalation only, the debond growth at the coating surface is in mixed mode. It can be realized that the added thermomechanical load changes the mode ratio (G_I/G_{II}) for the debond. Mainly it is Mode I for debonds $\alpha > 30^\circ$ that has increased considerably, due to the applied thermo-mechanical load, $\epsilon_x = 0.5\%$, acting normal to the crack plane for large debond angles α . The increase in Mode II ERR follow the same trends as for the case of only intercalation load, but with magnified values.

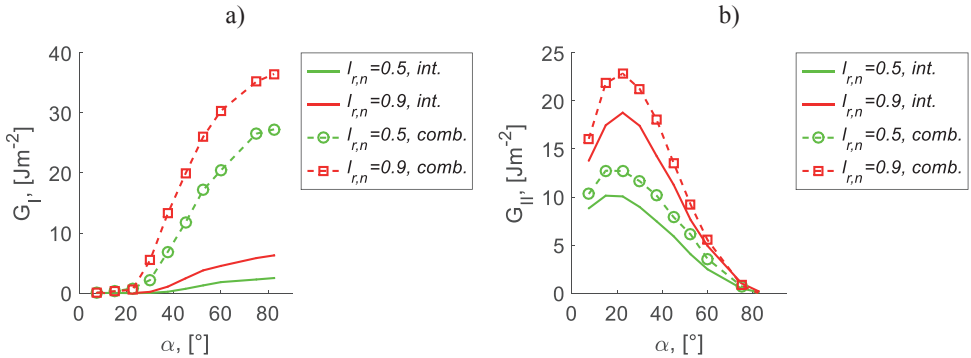


Figure 11. ERR as a function of the debond angular size, for debond crack along coating/matrix interface originating from vertical matrix crack under pure intercalation (solid lines) and combined loading (dashed lines): a) Mode I ERR and b) Mode II ERR.

In Figure 12a - Figure 12b the mixed mode character of the debond with and without horizontal matrix crack is shown for the load case with combined loading. The trends in ERR for debonding remain similar as in the electrochemical case. However, the impact of the added thermo-mechanical loading on Mode I ERR (Figure 12 a) is considerable, especially for debonds $\lambda \leq 40^\circ$, which is when the debond crack can be regarded as near-perpendicular to the direction of the applied load. For large debonds ($\lambda \geq 60^\circ$), the crack growth direction is near parallel with the x-axis, reducing G_I regardless of the added loads in the x - direction.

The added thermomechanical load results in added driving force for debond crack growth in Mode II for debond which is not preceded by a matrix crack, Figure 12 b. For debonds preceded by matrix cracks the thermomechanical load has an impeding effect on small debonds $\lambda \leq 40^\circ$, due to decreased shear stress at the coating/matrix interface. For debonds $\lambda > 40^\circ$ the added load increases G_{II} . The Mode I ERR is significantly larger than the Mode II ERR.

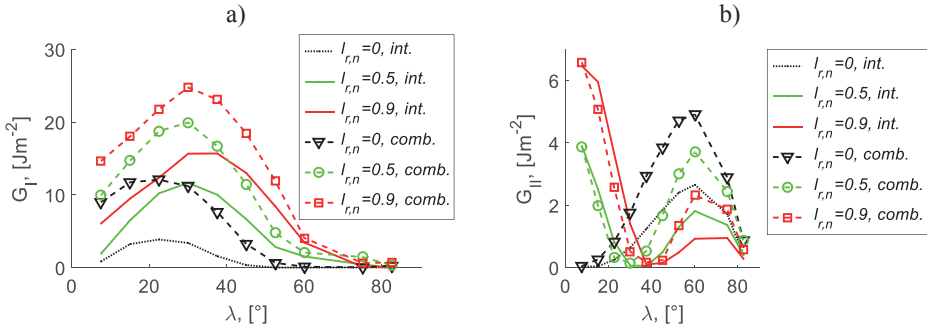


Figure 12. ERR as a function of the debond angular size, for a debond crack along coating/matrix interface originating from horizontal matrix crack under pure intercalation (solid lines) and combined intercalation and thermomechanical load (dashed lines): a) Mode I ERR and b) Mode II ERR.

In the above discussion it has been shown how the length of the radial crack, in both cases of propagation direction, affects the debond crack growth. However, the presence of debonds may have an effect on the radial crack ERR as well. In Figure 13 the debond length impact on Mode I

component of the ERR for matrix crack growth is shown for two crack length, $l_{r,n} = 0.5$ and $l_{r,n} = 0.9$, for the vertical matrix cracks in Figure 13a and the horizontal matrix cracks in Figure 13b. It is clear that the difference between the two matrix crack directions is very large. It is a direct result of the electrochemical loading which causes large swelling strains in the longitudinal direction of the 0°-deg layer, which facilitates the Mode I growth for the vertical matrix crack growing perpendicular to that layer. As the debond angle α increases, the amount of material that counteracts the radial crack growth decreases and the ERR is larger, Figure 13a. It can be expressed also in terms of the opening displacement of the matrix crack, which becomes significantly larger when the debond arc length increases.

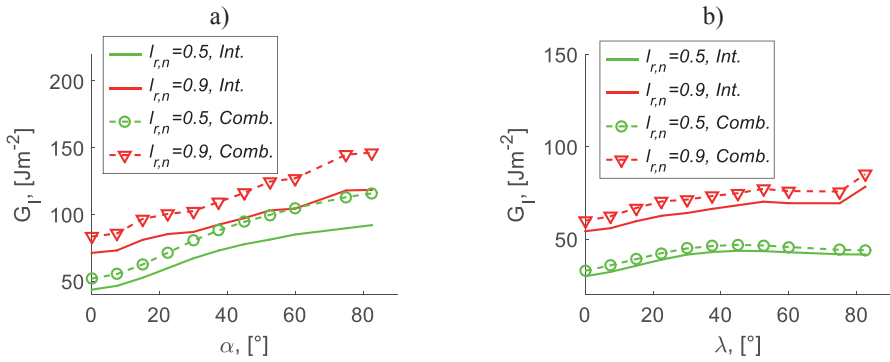


Figure 13. Debond angular size impact on the matrix crack tip for a) vertical cracks and b) horizontal cracks in the matrix.

The horizontal matrix crack growth, see Figure 13b, is less affected by increasing debond angle λ , with larger effect for small debonds ($\lambda \leq 30^\circ$), i.e. when the entire debond is normal to the horizontal matrix crack. The small increase of G_I for increasing λ , favors the radial crack growth slightly. As the debond grows further away from the radial crack, the changes in stress distribution due to the debonds ceases to impact the radial crack tip ERR. Thermo-mechanical loading, added to the electrochemical load, does not change the described trends but the ERR values are higher, see Figure 13.

In all cases the presence of the debond crack would facilitate the growth of the matrix crack. According to results presented in this paper the matrix crack growth is always unstable and, as shown in Figure 13, the presence and size of the debond does not change this feature.

CONCLUDING REMARKS

In this work linear elastic fracture mechanics have been used to analyze radial matrix crack propagation and debonding at coating/matrix interface in a carbon fiber reinforced structural composite aimed for multifunctional application. The material is a cross-plyed structural composite battery consisting of a solid electrolyte coated carbon fiber embedded in an electrochemically active material doped polymer matrix.

We have shown that the initial course of events before the transverse macro-scale matrix crack forming is different for a structural composite battery in comparison to a conventional cross-ply composite. Stress analysis shows that high hoop stress in the matrix at the coating/matrix interface during charging may be a reason for radial matrix cracks initiating at the coating/matrix interface. Propagation of these cracks was studied by calculating energy release rate (ERR) assuming square packing of fibers in the 90°-ply and using homogenized properties for the 0°-ply. For a micro-battery (unit in the structural composite) with fiber content $V_f = 0.338$, results show that the crack growth towards the nearest fiber in both x-direction and y-direction is unstable.

Due to anisotropic ply swelling in the cross-ply lay-up when subjected to electrochemical loading, large tensile radial and shear stresses at the coating/matrix interface make the debonding relevant for consideration. Unlike an UD laminate in electrochemical loading where a debond is not likely to occur without a radial crack, debonds alone can occur at the coating/matrix interface in a cross-ply. Results for ERR show that the debond crack growth is in mixed mode. The ERR values for the interface crack growth are lower than for the radial matrix crack growth. Therefore, the most probable sequence of failure event in the cross-ply laminate are: 1) vertical radial matrix crack

initiation and unstable growth; 2) debond is initiated at certain length of the matrix crack and propagates in a mixed mode manner.

REFERENCES

1. Garrett KW, Bailey JE. Multiple transverse fracture in 90° cross-ply laminates of a glass fibre-reinforced polyester. *J Mater Sci* 1977;12(1):157-168.
2. Varna J, Berglund L. Multiple transverse cracking and stiffness reduction in cross-ply laminates. *J Compos Technol Res* 1991;13(2):97-106.
3. Talreja R. Transverse Cracking and Stiffness Reduction in Composite Laminates. *J Composite Mater* 1985;19(4):355-375.
4. Nairn JA, Hu S, Bark JS. A critical evaluation of theories for predicting microcracking in composite laminates. *J Mater Sci* 1993;28(18):5099-5111.
5. Dvorak GJ, Laws N. Analysis of Progressive Matrix Cracking In Composite Laminates II. First Ply Failure. *J Compos Mater* 1987;21(4):309-329.
6. Varna J, Berglund LA, Ericson ML. Transverse single-fibre test for interfacial debonding in composites: 2. Modelling. *Compos Part A Appl Sci Manuf* 1997;28(4):317-326.
7. Zhang H, Ericson ML, Varna J, Berglund LA. Transverse single-fibre test for interfacial debonding in composites: 1. Experimental observations. *Compos Part A Appl Sci Manuf* 1997;28(4):309-315.
8. París F, Caño JC, Varna J. The fiber-matrix interface crack — A numerical analysis using Boundary Elements. *Int J Fract* 1990;82(1):11-29.
9. Martyniuk K, Sørensen BF, Modregger P, Lauridsen EM. 3D in situ observations of glass fibre/matrix interfacial debonding. *Composites Part A: Applied Science and Manufacturing* 2013;55:63-73.
10. Asp LE, Greenhalgh ES. Structural power composites. *Composites Sci Technol* 2014;101:41-61.
11. Asp L, Bismarck A, Lindbergh G, Leijonmarck S, Carlson T, Kjell M. Structural battery half cell, a structural battery and their manufacture. 2015(2893582).
12. Carlson T. Multifunctional composite materials : Design, manufacture and experimental characterisation. PhD Thesis, Luleå University of Technology, Material Science;, 2013.

13. Leijonmarck S, Carlson T, Lindbergh G, Asp LE, Maples H, Bismarck A. Solid polymer electrolyte-coated carbon fibres for structural and novel micro batteries. *Compos Sci Technol* 2013;89:149-157.
14. Jacques E, Hellqvist Kjell M, Zenkert D, Lindbergh G, Behm M. Expansion of carbon fibres induced by lithium intercalation for structural electrode applications. *Carbon* 2013;59:246-254.
15. Zhang W-. Structure and performance of LiFePO₄ cathode materials: A review. *J Power Sources* 2011;196(6):2962-2970.
16. Pupurs A, Varna J. Modeling mechanical stress and exfoliation damage in carbon fiber electrodes subjected to cyclic intercalation/deintercalation of lithium ions. *Compos B Eng* 2013.
17. Xu J, Lindbergh G, Varna J. Multiphysics modeling of mechanical and electrochemical phenomena in structural composites for energy storage: Single carbon fiber micro-battery. *J Reinf Plast Compos* 2018;37(10):701-715.
18. Xu J, Göran Lindbergh, Varna J. Carbon fiber composites with battery function: Stresses and dimensional changes due to Li-ion diffusion. *J Compos Mater* 2018:0021998317752825.
19. Xu J, Varna J. Matrix and interface microcracking in carbon fiber/polymer structural micro-battery. Submitted to *Journal of Composite Materials* 2018.
20. Hashin Z, Rosen B.W. The elastic moduli of fiber-reinforced materials. 1964;32(2):223-232.
21. Hashin Z. Analysis of Composite Materials- A Survey. *J Appl Mech Trans ASME* 1983;50(3):481-505.
22. Christensen RM, Lo KH. Solutions for effective shear properties in three phase sphere and cylinder models. *J Mech Phys Solids* 1979;27(4):315-330.
23. Marklund E, Varna J, Neagu RC, Gamstedt EK. Stiffness of aligned wood fiber composites: Effect of microstructure and phase properties. *J Compos Mater* 2008;42(22):2377-2405.
24. Carlstedt D, Marklund E, Asp LE. Effects of state of charge on elastic properties of 3D structural battery composites. *Compos Sci Technol* 2019;169:26-33.
25. Siegel JB, Stefanopoulou AG, Hagans P, Ding Y, Gorsich D. Expansion of Lithium Ion Pouch Cell Batteries: Observations from Neutron Imaging. *J Electrochem Soc* 2013;160(8):A1031-A1038.
26. Wang X, Sone Y, Segami G, Naito H, Yamada C, Kibe K. Understanding Volume Change in Lithium-Ion Cells during Charging and Discharging Using In Situ Measurements. *J Electrochem Soc* 2007;154(1):A14-A21.

27. Zhang N, Tang H. Dissecting anode swelling in commercial lithium-ion batteries. *J Power Sources* 2012;218:52-55.
28. Krueger R. Virtual crack closure technique: History, approach, and applications. *Appl Mech Rev* 2004;57(1-6):109-143.
29. Toray Composite Materials America, Inc. T800H Intermediate Modulus Carbon Fiber. 2018.
30. Zhuang L, Talreja R, Varna J. Transverse crack formation in unidirectional composites by linking of fibre/matrix debond cracks. *Compos Part A Appl Sci Manuf* 2018;107:294-303.

Paper V

Methodology for mechanical quality evaluation of carbon fiber coating with energy storage function

Johanna Xu, Janis Varna

Department of Engineering Sciences and Mathematics, Luleå University of Technology SE-97187 Luleå, Sweden

Abstract

A method is described for evaluation of fiber/coating interface quality of novel multifunctional fiber composites. One of the functions of these materials is mechanical performance but the interfacial properties may be significantly reduced. The method can be used when the available amount of fibers is insufficient for macroscale tests. Dry coated fiber bundles of the novel composite are embedded at the mid-plane of a Double Cantilever Beam (DCB) specimen, between layers of commercial unidirectional (UD) prepreg material. The excess resin in prepreg layers impregnates the bundles. The crack in the DCB test propagates through the weakest region (in the coated fiber bundle with weak interface between coating and the fiber). The fiber surface and the fiber imprint in the matrix, containing parts of the coating, are analyzed using scanning electron microscopy (SEM) to correlate the locally varying fracture toughness values with the SEM observations.

The methodology is demonstrated on coated carbon fibers with electrical energy storage and mechanical functions. Mode I tests show the influence of coating thickness variation along the fiber on changing failure mechanisms and on the fracture toughness.

Introduction

In composite materials the efficiency of stress transfer from matrix to reinforcement and, hence several mechanical properties including compressive strength, strain to failure, damage initiation, fracture toughness and fatigue life depend on fiber/matrix interface [1]. In most cases, fibers are coated with sizing to enhance interfacial properties [2]. Other reasons for coating may be introducing additional functionalities to the composite material. One route for

multifunctional performance of carbon fiber reinforced polymers, currently under development, is introducing electrical battery function by stipulating extra requirements for all constituents [3-5]. In the present case, the coating constitutes the active electrode material, where ions can be inserted. Hagberg et al. [6] described the manufacturing of carbon fibers coated with lithium iron phosphate particles, with a particle size of 100-300 nm, by electrophoretic deposition.

The fracture toughness of the coating/fiber interface is still an issue, since one of the functions for these novel composites is mechanical performance. It is expected to be lower than for composites with high mechanical performance but high enough to avoid premature composite failure.

These materials are still under development, and most of used coating techniques are limited by small-scale and batch-wise manufacturing under inert conditions (though continuous electrocoating process at ambient conditions has been investigated [7]). Fiber bundles (not individual fibers) are coated and the variability of the coating thickness between different bundles and inside each individual bundle is rather large even for the same manufacturing parameters. The feature that the particle size is comparable with the coating thickness add additional complexity to possible failure mechanisms. The amount of coated fibers from these setups is not sufficient for macro-specimens to be manufactured and tested.

The commonly used test techniques for interface characterization on single fiber scale are the single fiber fragmentation, the single fiber pull-out and push-out tests [8]. However, fibers coated in bundles risk damaging the coating in the single fiber separation process during test preparation, making certain methods dubious.

The methodology suggested in this paper is based on double cantilever beam (DCB) test, widely used on macroscale [9,10] to determine Mode I fracture toughness. A special symmetric DCB specimen is designed with dry coated fiber bundles of the novel material in

the middle. Fibers in the bundles are aligned along the specimen axis (0° -bundles). The coated fiber bundles are embedded between prepreg layers of commercial unidirectional composite aligned in the same direction. During curing, the excess resin in the prepreg impregnates the coated bundles. The DCB specimen and possible microdamage locations are shown in Figure 1. The Mode I fracture toughness, G_{IC} , measured in the test, reflects possible combination of failures at all interfaces and/or in the matrix and in the coating. Scanning electron microscopy (SEM) and optical fractographic analysis are performed to correlate the measured local variation of G_{IC} along the specimen with the actual failure mechanisms close to the fiber. The performed analysis shows that the mechanism of failure changes with the coating thickness: more energy is absorbed and the crack path is longer if the coating is thin.

Method

DCB test on the designed specimens was carried out to determine the Mode I interlaminar fracture toughness, using multiple loading-unloading steps to achieve stable crack propagation.

1.1 Materials and specimen

The DCB specimens (DCB-1, DCB-2 and DCB-3) were manufactured from carbon fiber/epoxy prepreg (HexPly® M10/38%/UD300/CHS, ABIC Kemi, Sweden) stacking 22-ply in 0° direction and placing the coated bundles in the middle; also in 0° direction. The coated fiber bundle thickness was about 5 fibers. A pre-crack of 40mm was created with a 7 μ m PTFE-film insert, placed at one end of the specimen between coated bundles, Figure 1a. Two piano hinges were attached to the end of the specimen using mechanical joints, Figure 1b.

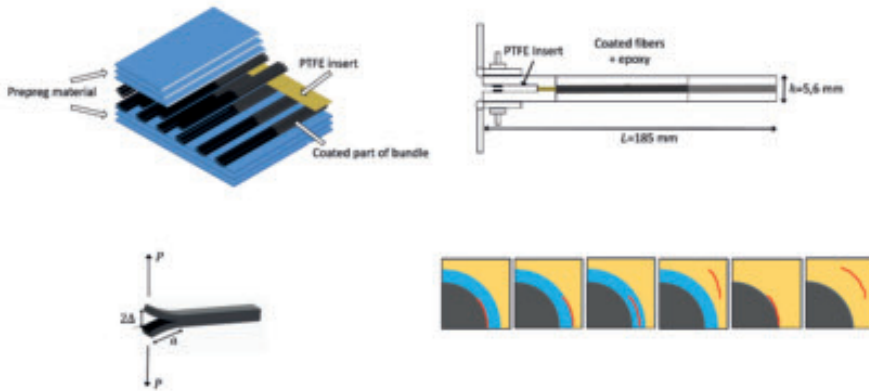


Figure 1. DCB test: schematics of a) material manufacturing, b) specimen geometry and c) test definition. d) possible damage initiation sites along, at i) fiber/coating, ii) coating/matrix interfaces, in the iii) coating and iv) matrix.

1.2 DCB test method

A hydraulic universal testing machine (Instron 3366) with a 10kN load cell was used to perform the tests, under displacement control at room temperature conditions, with a crosshead speed of 2mm/min during loading and 10mm/min during unloading. Compliance calibration (CC) method was used for data reduction. The critical strain energy release rate (fracture toughness), G_{IC} , for each crack length was found using Eq. (1) [11]

$$G_{IC} = \frac{P_{max}^2}{2b} \frac{\partial c}{\partial a} \quad (1)$$

where P_{max} is the recorded load for each crack length a when the crack start to grow, b is the specimen width and c is the specimen compliance for crack length a

$$c = 2\Delta/P \quad (2)$$

where 2Δ is the load point vertical displacement, and P is the recorded load, see Figure 1c.

The compliance as a function of crack length was calibrated using a power function:

$$c = Aa^n \quad (3)$$

where coefficients A and n for the particular specimen are obtained from the compliance (c) versus crack length (a) curve.

1.3 Fracture surfaces

Fractographic analysis was performed on the fully separated half beams of the specimens.

Fracture surfaces of the coated bundle were Au sputter-coated and examined using a JEOL-IT300LV SEM.

Results and Discussion

Since the coated fiber bundle was dry prior to the manufacturing, the quality of its impregnation by the excess matrix of the prepreg is of great importance. It should be avoided that poor impregnation is the reason for premature crack propagation in the test. In Figure 2a, a cross section of the DCB specimen captured in light microscope is shown. The fiber volume fraction, V_f , for the embedded coated bundle is lower than for the supporting prepreg material, and most important; the porosity is negligible. SEM images, Figure 2b-Figure 2c, render complementary information showing that the impregnation on the fiber/matrix scale by epoxy from the prepreg is good.

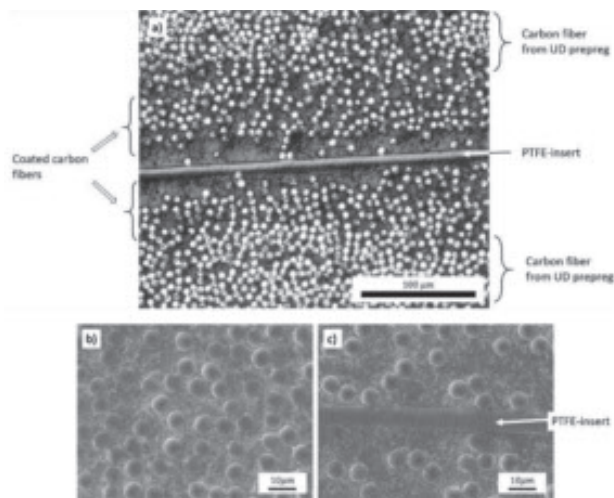


Figure 2. a) Polished cross section of specimen with PTFE-film and coated bundles at the mid-plane. b) SEM image of carbon fiber from the prepreg material, c) SEM image of the coated fibers.

The Mode I fracture toughness is sensitive to a number of interacting factors, including: V_f , resin toughness, local plasticity [12,13], strength/fracture toughness of interfaces, the latter differing between the coated and uncoated part of the bundle. Hence, a direct identification of contribution of each mechanism is not possible.

The recorded load-displacement curves for one specimen are shown in Figure 3a, the corresponding G_{IC} as a function of crack length a is calculated using Eq. (1) - (3) and shown in Figure 3b.

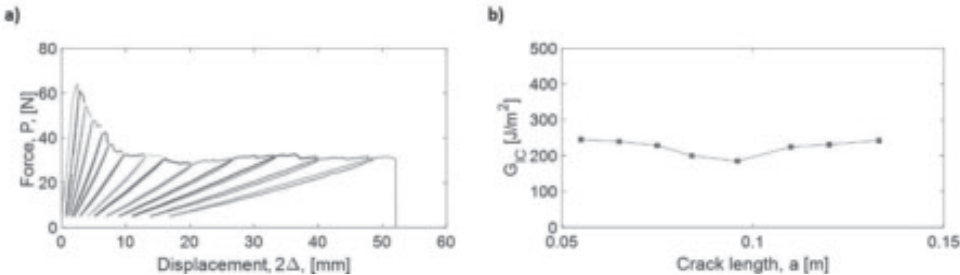


Figure 3. a) Load vs displacement curves for DCB specimen containing coated fibers at the specimen mid-plane. b) G_{IC} vs crack length.

G_{IC} values for all tested specimens are shown in Figure 4. While G_{IC} is stable with increasing crack length for two of the specimens, DCB-1 and DCB-2, but with widely different values, at around 500 J/m^2 and 200 J/m^2 , respectively, a leaping behavior can be found for DCB-3 specimen, with values ranging between these two extreme values.

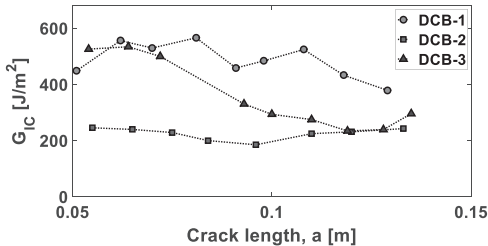


Figure 4. Critical Mode I strain energy release rate G_{IC} for tested specimens, DCB-1, DCB-2 and DCB-3, with coated bundles at the mid-plane of a 22 ply UD carbon fiber/epoxy prepreg.

SEM fractography indicates that the variations in measured G_{IC} can be attributed to varying coating thickness between bundles, and within each bundle. The pulled-out fibers and carbon fiber imprints in the damaged composite in the low G_{IC} specimen (DCB-2) show that the interface between coating and fiber has failed, see Figure 5, where the imprint contains coating particles (Figure 5a) and the fiber surface (Figure 5b) is clean.

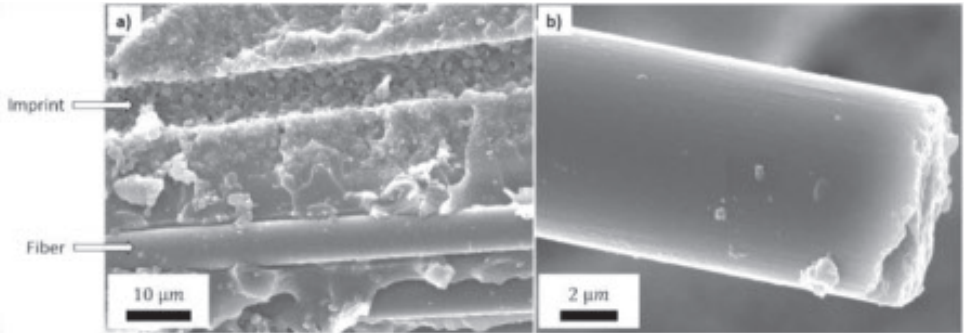


Figure 5. Fracture morphology of the DCB-2 specimen with low strain energy release rate (G_{IC}). a) imprint of a fiber with coating particles and a fiber with clean surface and b) clean fiber surface (magnified).

In specimen DCB-1, Figure 6a, the imprints from the fiber in the fracture surface contain only some coating particles, resulting in more particles and even the matrix adhered to the fiber (Figure 6b-c), The crack surface alternates through the coating from the fiber/coating interface to the coating/matrix interfaces (even inside the matrix) and back to the fiber surface. The real crack path becomes longer than the nominal, and the crack is crossing regions with higher toughness, which correlates to higher G_{IC} in this region.

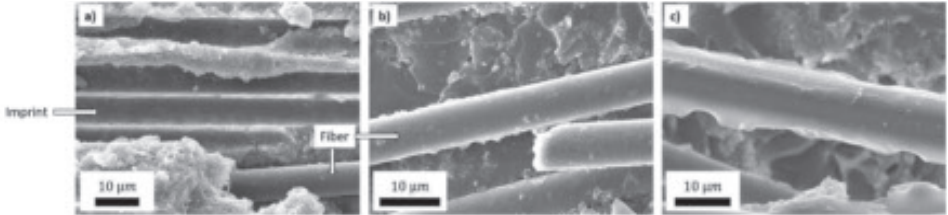


Figure 6. SEM picture of fracture surface of DCB-1 specimen with high strain energy release rate (G_{IC}). a) imprint of a fiber not containing particles and rests of the coating b) fiber surface with rests of resin.c) fiber surface with rests of resin and matrix.

This behavior seems to be more typical for thinner coating when the particle size becomes comparable with the coating thickness: the coating does not behave as a homogenized material, and high heterogeneity facilitates crack deviation. Fractography of specimen DCB-3 with G_{IC} leaping from high to low confirms these observations; in the region where G_{IC} is high, only a few particles are seen on the imprint surface, whereas many particles and rests of the coating material are on the imprint in the low G_{IC} region, Figure 7.

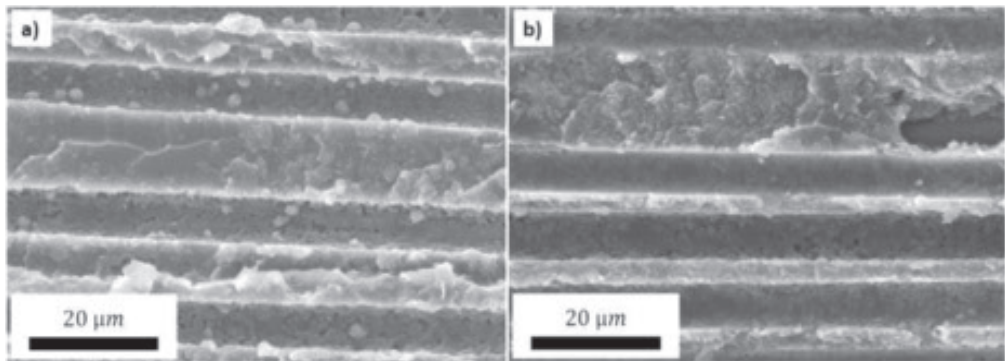


Figure 7. SEM picture of fracture surface of DCB-3 specimen a) imprint of fiber in the beginning of the coated part of the specimen b) imprint of fiber at the end of the coated part of the specimen with low G_{IC} .

Conclusions

Specially designed macro-specimens have been used in DCB test to study fiber/coating interface properties in novel composites, where due to insufficient amount of fibers to produce macro-specimens, the coated fiber bundle is embedded in-between two unidirectional layers of a commercial prepreg and impregnated by the excess of the resin in the prepreg. The analyzed case is novel coated carbon fibers for energy storage applications, where the coating itself is a particulate composite. The post-test SEM fractographic analysis of the fracture surface was used to correlate the highly different G_{IC} values with differences in fiber imprints in the matrix and cleanness of fiber surfaces.

It was found that for the used material, the fiber/coating interface is the weakest among all interfaces. In some cases the coating material was still connected with the fiber and in other cases it was found in the imprint in the matrix. The current non-standardized coating process results in large variation of coating thickness along fiber, between fibers and between bundles. The observed failure mechanisms in the DCB test is as follows

- Thick coating: $G_{IC} = 200 \text{ J/m}^2$ is measured in the DCB test with debonding between fiber and coating with clean fiber surface.
- Thin coating: $G_{IC} = 500 \text{ J/m}^2$ is measured in the DCB test. Heterogeneity of the coating is high (particle size is comparable with the coating thickness), the fiber/coating interface crack deviates in the coating reaching the coating/matrix interface and returning to the fiber/coating interface. The real crack path is longer and crosses regions with higher fracture toughness.

Acknowledgement

The Swedish Energy Agency, project number 37712-1 is acknowledged for funding. Research Engineer Johnny Grahn is acknowledged for assistance with fractography in the SEM.

References

1. Hull D, Clyne TW. An introduction to composite materials. Cambridge: Cambridge Univ. Press, 1996.
2. Bismarck A, Lee AF, Saraç AS, Schulz E, Wilson K. Electrocoating of carbon fibres: A route for interface control in carbon fibre reinforced poly methylmethacrylate? *Compos Sci Technol* 2005;65(10):1564-1573.
3. Asp LE, Greenhalgh ES. Structural power composites. *Composites Sci Technol* 2014;101:41-61.
4. Xu J, Göran Lindbergh, Varna J. Carbon fiber composites with battery function: Stresses and dimensional changes due to Li-ion diffusion. *J Compos Mater* 2018:0021998317752825.

5. Snyder JF, Wong EL, Hubbard CW. Evaluation of Commercially Available Carbon Fibers, Fabrics, and Papers for Potential Use in Multifunctional Energy Storage Applications. *J Electrochem Soc* 2009;156(3):A215-A224.
6. Hagberg J, Maples HA, Alvim KSP, Xu J, Johannisson W, Bismarck A, Zenkert D, Lindbergh G. Lithium iron phosphate coated carbon fiber electrodes for structural lithium ion batteries. *Compos Sci Technol* 2018;162:235-243.
7. Bachinger A, Rössler J, Asp LE. Electrocoating of carbon fibres at ambient conditions. *Composites Part B: Engineering* 2016;91(Supplement C):94-102.
8. Godara A, Gorbatiikh L, Kalinka G, Warriar A, Rochez O, Mezzo L, Luizi F, van Vuure AW, Lomov SV, Verpoest I. Interfacial shear strength of a glass fiber/epoxy bonding in composites modified with carbon nanotubes. *Compos Sci Technol* 2010;70(9):1346-1352.
9. Yasaee M, Bond IP, Trask RS, Greenhalgh ES. Mode I interfacial toughening through discontinuous interleaves for damage suppression and control. *Compos Part A Appl Sci Manuf* 2012;43(1):198-207.
10. Madhukar MS, Drzal LT. Fiber-matrix adhesion and its effect on composite mechanical properties: I. Inplane and interlaminar shear behavior of graphite/epoxy composites. *J Compos Mater* 1991;25(8):932-957.
11. Sela N, Ishai O. Interlaminar fracture toughness and toughening of laminated composite materials: a review. *Composites* 1989;20(5):423-435.
12. Hunston DL. Composite interlaminar fracture: effect of matrix fracture energy. *Compos Technol Rev* 1984;6(4):176-180.
13. Bradley WL, Cohen RN. Matrix Deformation and Fracture in Graphite-reinforced Epoxies. *ASTM Spec Tech Publ* 1985:389-410.

Department of Engineering Sciences and Mathematics
Division of Materials Science

ISSN 1402-1544
ISBN 978-91-7790-312-3 (print)
ISBN 978-91-7790-313-0 (pdf)

Luleå University of Technology 2019